FAST TIME-DOMAIN DIFFUSE OPTICAL TOMOGRAPHY FOR BREAST TISSUE CHARACTERIZATION AND IMAGING

MO WEIRONG

(M. Eng, Zhejiang University, P. R. China)

A THESIS SUBMITTED

FOR THE DEGREE OF DOCTOR OF PHYLOSOPHY

DIVISION OF BIOENGINEERING

NATIONAL UNIVERSITY OF SINGAPORE

2009

Acknowledgements

First and foremost, I would like express my sincere gratitude to my supervisor, Dr. Chen Nanguang for his invaluable inspiration, guidance, advice, constructive criticism and encouragement throughout this PhD research, and his proofreading on this PhD thesis as well.

I would also like thank the following students: T. Chan for her help on *in vivo* experiments; E. Kiat for his help on phantom fabrication; G. X. Tham for his help on system optimization. Without their helps, this research would not progress smoothly.

In addition, I would thank my colleagues: C. H. Wong, Y. Xu, L. Liu, Q. Zhang and L. Chen for their continual help.

I am grateful for the research funding support from Office of Life Science (R397-000-615-712), National University of Singapore and A*STAR/SERC (P-052101 0098) and the research scholarship from National University of Singapore.

Last, I would like to thank my parents and Haihua Zhou for their continual support, encouragements and help throughout my PhD research.

Table of Contents

Summary

Near-infrared (NIR) diffuse optical tomography (DOT) has been proven in last decade as a promising non-invasive optical imaging modality for soft tissue imaging, especially suitable for human breast imaging. This research aims to explore the feasibility of a novel tomographic imager to characterize the optical properties of human breast tissue *in vivo*. The innovation of this approach is to use a high speed pseudorandom bit sequence (PRBS) to acquire the time-resolved signals or the temporal point spread functions (TPSF). The prototype system was constructed. Its performance was assessed in phantom experiments. Furthermore, the prototype system was used to characterize the optical properties and physiological parameters of human breast tissues *in vivo*. Correlations between optical properties, physiological parameters of the breast tissue and the demographic factors (age, menopausal state and body mass index) were established. The preliminary *in vivo* results are promising. The prototype system based on the spread spectrum correlation technique has demonstrated a couple of advantages, including sub-nanosecond (~0.8 ns) temporal resolution, fast data acquisition and the favorable insensitivity of detection to environmental illumination. All of these features demonstrate the novel time-domain DOT developed in this research is highly potential for the clinical applications of breast cancer detection.

List of Tables

List of Figures

List of Symbols

λ	Wavelength, *nm*
c	Velocity of light in a medium, *cm/s*
c_0	Velocity of light in the vacuum, *cm/s*
c_a	Concentration of the absorber, μ *mol*
D	Diffusion coefficient, cm^{-1}
d	Thickness of the medium, *cm*
$\mu_a(\lambda)$	Absorption coefficient at wavelength λ, cm^{-1}
$\mu_s(\lambda)$	Scattering coefficient at wavelength λ, cm^{-1}
g	Isotropic factor
$\mu_s'(\lambda)$	Reduced scattering coefficient at wavelength λ, cm^{-1}
f	Frequency, *Hz*
k	Photon density wave number, cm^{-1}
$k_i(\omega)$	Imaginary part of the photon density wave number, cm^{-1}
$k_r(\omega)$	Real part of the photon density wave number, cm^{-1}
$l_d = \mu_d^{-1}$	Diffusion length, *cm*
$l_{tr} = \mu_t^{-1}$	Photon mean free path, *cm*
n	Relative refractive index of tissue
n_{H_2O}	Refractive index of water
p	Laplace parameter in Laplace domain
$\varepsilon(\lambda)$	Specific extinction coefficient at wavelength λ
τ	Delay time, *ps*
t	Time, *s*
P	Power, *mW*
I	Intensity of light, *mW*
φ	Photon density wave function
Q	Ultrashort pulse light source
SO	Oxygenation saturation
THC	Total hemoglobin concentration, *μMol/L*
Hb	Deoxyhemoglobin
HbO	Oxyhemoglobin

Chapter 1. Introduction

The near-infrared (NIR) optical diffuse imaging (DOI) technique was firstly proposed by Jöbsis in 1977 [1]. With the rapid development of semiconductor technologies, computation technologies and instrumentation industry in the last two decades, the performance of DOI techniques has been significantly improved. Meanwhile, the system cost has greatly reduced. Nowadays, various DOI techniques are under research worldwide. The application has extended from laboratory bench top to preclinical field. DOI has been proven with great potential to complement conventional structural/functional imaging modalities for clinical imaging, especially breast cancer detection.

1.1 Motivation

Breast cancer is the 2nd most common cancer all over the world after lung cancer and the 5th most common cause of cancer death. According to world health organization (WHO) statistics in 2004, breast cancer approximately cause 519 000 deaths worldwide every year (7% of cancer death; almost 1% of all deaths) [2]. In America, it is estimated that 12.5% woman will develop breast cancer in her lifetime [3]. In Europe, approximately 9% women will be diagnosed breast cancer in her lifetime [4]. In Singapore, the breast cancer occurrence rate is lower. The chance is estimated to be 4% to 5% - about 1/3 of American women and half of European women. Even though, breast cancer is still the most common cancer in Singapore women, with almost 1 300 new cases diagnosed each year, of which 270 cases die from it [5].

Early detection and cure can significantly reduce the mortality rate of breast cancer [6]. Breast imaging is a commonly used approach to find breast cancer. Conventional breasts imaging modalities, such as x-ray mammography, magnetic resonance imaging (MRI), and ultrasound, provide structural/functional imaging information. But their performance is limited more and less by their own shortcomings. The diffuse optical imaging modalities are advantageous on non-ionization hazard, non-invasiveness, low cost, portability as well as unique differentiation capability among soft tissues, which has been proven especially suitable for breast cancer detection at early stage.

In the last decade, NIR DOIs for breast cancer detection has got fruitful advances. Nowadays researchers worldwide are racing toward the next generation optical mammography, which can be clinically acceptable for breast cancer patients.

As we known, most all conventional time-domain DOT systems use a pulsed laser as the light source to illuminate the tissue, and use streak cameras or time-correlated single photon counters (TCSPC) to detect the photons emitted from tissue. The systems using streak camera are normally limited by small photon collection area, small dynamic range, and temporal nonlinearity. The TCSPC-based systems are more popular for large dynamic range, high temporal linearity, and high temporal resolution. However, the TCSPC-based DOTs are normally limited by a slow data acquisition speed, which would cause problem if multiple source-detector channels work together. Also it should be noted that the TCSPC system must work in an extremely dark environment to achieve the best performance. This condition is practically

difficult to satisfy. Last, ns/ps/fs-pulse lasers and TCPSC (or streak camera) usually lead to a high system cost and a more complex control structure. This situation will become prohibitive if multiple channels are used. For these reasons, it is necessary to develop a novel DOT imaging approach.

This PhD research leads to the development of advanced fast multi-channel time-resolved optical tomography imaging instrument, as well as the clinical applications for examining early-stage human breast cancer.

1.2 Objectives

The objective of this research is to develop a new fast time-domain diffuse optical tomographic imager. The laboratory prototype system will be implemented. In this new approach, the NIR light is modulated by a train of high speed pseudorandom bit sequence (PRBS). The modulated NIR light goes through phantom or tissue. The emitted optical signals are demodulated by correlating with the reference PRBS. In this way the time-resolved signals, or temporal point spread functions (TPSF) can be acquired very fast. For image reconstruction, the theory of diffuse equation and the semi-infinite boundary conditions will be adopted to resolve the forward and inversed problems. The map of spatial variations of optical properties will be reconstructed. The performance of prototype system will be assessed in phantom experiments. As last, preclinical *in vivo* experiments will be carried out on human breasts and the preliminary spectroscopic data will be acquired and analyzed before moving forward to *in vivo* clinic imaging applications.

Specifically, this research aims

- to propose, design, implement, optimize and evaluate a novel time-resolved DOT technique. Emphasis will be placed on achieving optimal temporal resolution and signal to noise ratio, fast data acquisition speed and stable performance.
- to design an optical hand-held probe and the detection geometry.
- to develop advanced image reconstruction algorithms for high quality optical mammography. The spatial resolution of tomographic images should get into sub-centimeter regime.
- to obtain reference data from subjects and establish correlation between optical properties and physiological parameters.

1.3 Thesis organization

This thesis is constituted by three parts: the first part reviews the fundamental tissue optics, which closely relates to this research. The second part describes the proposal of a fast time-domain diffuse optical tomography prototype system, followed by the detailed descriptions of prototype system implementation and system performance assessment in phantom experiments. The last part describes the *in vivo* experiments, which establishes the preliminary relationship between the optical properties and the physiological parameter versus subjects' demographic information.

In detail, each part is organized as below:

Part I:

Chapter 2 is a preparatory chapter. Topics of tissue optics are selectively reviewed in this chapter. Chapter 2 constitutes the base of the entire research.

Chapter 3 starts with brief reviews of three commonly used image modalities for breast cancer detection, including X-ray mammography, MRI, and ultrasound. After that, optical imaging/spectroscopy theories are reviewed in-deep, including three most popular DOT/DOS techniques: continuous-wave (CW), frequency-domain (FD) and time-domain technique.

Part II:

Chapter 4 systematically describes the working principle of the novel fast TD-DOT system based on the spread spectrum correlation technique.

Chapter 5 describes the phantom experiments, including phantom preparation, experiment setup, system assessment, *etc*. The image reconstruction algorithm and results were described in detail. Chapter 4 and 5 constitute the first contribution from this research [7, 8].

Part III:

Chapter 6 describes in detail the preliminary *in vivo* diffuse optical spectroscopic experiment on human breast tissues. The experimental data processing and results analyses are described. Chapter 6 constitutes the second contribution from this research [9].

Chapter 7 summarizes the entire thesis and proposes the feasible improvements for the upcoming *in vivo* clinical applications.

Chapter 2. Tissue optics on breasts

This chapter selectively reviews some fundaments of tissue optics, which constitutes the base of this research.

2.1 Fundamental tissue optics

The light-tissue interaction can be classified into two types: *destructive* and *nondestructive*. The destructive light-tissue interaction will lead to the alternations of tissue structures or compositions. The major types include *photochemical*, *photothermal*, *photoablative* and *electromechanical* effects. The DOT/DOS techniques belong to the nondestructive light-tissue interaction regime because the optical power used in the tissue illumination is normally range from small to medium power (Class III), so that the above destructive effects will not occur [10].

The light propagation though the tissue can be classified into two types: absorption and scattering, which are quantified by using absorption coefficient μ_a and scattering coefficient μ_s (or reduced scattering coefficient μ_s'), respectively.

2.1.1 Absorption

The wavelength-dependent *absorption coefficient* $\mu_a(\lambda)$ (unit: cm^{-1}) is defined by,

$$dI = -\mu_a(\lambda) \cdot I \cdot dx \tag{2-1}$$

where dI is the differential change of the optical intensity. I is the intensity of the incident light. dx is an infinitesimal path of a homogeneous non-scattering medium where the light passes though.

For a slab of homogenous scattering-free medium in Fig. 2-1, the integrating of Eq. (2-1) over the medium thickness d yields,

$$I_o = I_i \cdot e^{-\mu_a(\lambda)\cdot d} \tag{2-2}$$

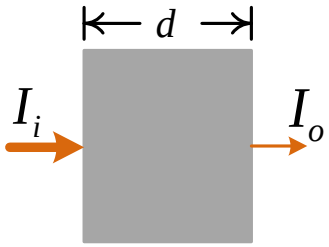

Fig. 2-1 Attenuation of light in a non-scattering homogenous absorptive medium.

The absorption coefficient $\mu_a(\lambda)$ can also be expressed in terms of particle density ρ and absorption cross section σ_a as

$$\mu_a(\lambda) = \rho \cdot \sigma_a \tag{2-3}$$

which yields the *Beer-Lambert* law,

$$I_o = I_i \cdot e^{-\mu_a(\lambda)\cdot d} = I_i \cdot e^{-\rho\cdot\sigma_a\cdot d} \tag{2-4}$$

The reciprocal, $1/\mu_a$ is called the absorption path length and equals to the mean free path that a photon travels between two consecutive absorption events.

Another parameter that is commonly used is the specific extinction coefficient ε. It represents the level of absorption per micro molar of compound per liter of solution per cm (unit $\mu M^{-1}\cdot cm^{-1}$). For most general cases in which multiple

absorbers with individual absorption coefficients $\mu_i(\lambda)$ ($i \in [1,2\ldots N]$) coexist in a non-scattering medium, Eq. (2-2) can be expressed as:

$$I_o = I_i \cdot e^{-\sum_{i=1}^{N} \mu_a(\lambda) \cdot d_i} \tag{2-5}$$

Then the Beer-Lambert law can be expressed as

$$I_0 = I_i \cdot e^{-\sum_{i=1}^{N} \mu_{a(\lambda)} \cdot d_i} = I_i \cdot e^{-\sum_{i=1}^{N} \rho_i \cdot \sigma_i \cdot d_i} \tag{2-6}$$

where d_i is the slab distance for absorber i. For a homogenous absorptive medium with a thickness of d, the absorption coefficient is the contributed by all of the absorptive constituents, i.e.:

$$\mu_a(\lambda) = \sum_{i=1}^{N} \rho_i \cdot \sigma \tag{2-7}$$

The transmission T is defined as the ratio of the transmitted intensity I_0 to the incident intensity I_i,

$$T = \frac{I_o}{I_i} \tag{2-8}$$

The wavelength-dependent optical density (OD) of an attenuating medium at wavelength λ is defined by

$$OD(\lambda) = \lg\left(\frac{1}{T}\right) = -\lg\left(\frac{I_o}{I_i}\right) \tag{2-9}$$

$$OD(\lambda) = -\lg\left(\frac{I_o}{I_i}\right) = -\lg(e)\mu_a(\lambda) \cdot d = \varepsilon(\lambda) \cdot c \cdot d \tag{2-10}$$

where $\varepsilon(\lambda)$ is the specific absorption coefficient of medium at wavelength λ. c is the concentration of absorber in unit of μM.

2.1.2 Refractive index

The light speed c in a specific medium with a *refractive index* n_r is defined by

$$c = \frac{c_0}{n_r}. \tag{2-11}$$

where c_0 is the light speed in vacuum.

When a light beam arrives the interface between two different media in an angle of θ_i, it will be refracted into the medium in an propagation angle of θ_r (Fig. 2-2), where θ_i, θ_r and n follow the *Snell's law*,

$$n_i \sin \theta_i = n_r \sin \theta_r \tag{2-12}$$

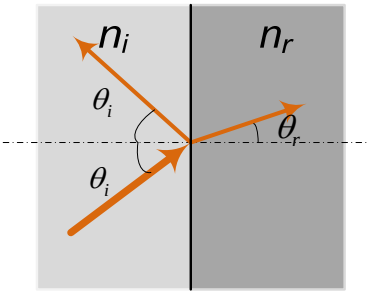

Fig. 2-2 Refractive effect of light when travels across two media with different refractive indices ($n_r > n_i$).

In breast, different tissues have different refractive indices. The refractive index varies from 1.33 (water) to approximately 1.55 (fat and concentrated protein solution). In most researches, a refractive index of 1.40 was widely accepted for the overall breast tissue [11, 12].

2.1.3 Scattering

Scattering is the phenomenon that causes the light propagation direction to be changed within a medium. It can be quantified using the scattering coefficient

$\mu_s(\lambda)$. For a collimated beam with intensity of I_0 , its intensity I_i after going through a non-absorptive homogenous scattering medium with a thickness of d (Fig. 2-3), is given by,

$$I_o = I_i \cdot e^{-\mu_s(\lambda)\cdot d} \tag{2-13}$$

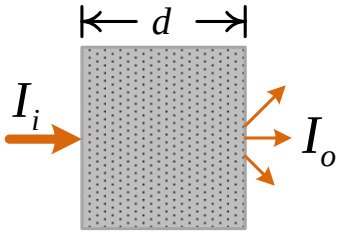

Fig. 2-3 Light scattering after going through a non-absorptive homogeneous scattering medium.

where the scattering coefficient $\mu_s(\lambda)$ is wavelength dependent. It can also be defined in terms of particle density ρ and scattering cross section σ_s:

$$\mu_s(\lambda) = \rho \cdot \sigma_s \tag{2-14}$$

The scattering coefficient quantifies the probability of a photon being scattered per unit length. Its reciprocal $1/\mu_s(\lambda)$ is called the mean scattering path, which quantifies an average distance that a photon travels between two consecutive scattering events.

When a photon travels through the medium, it will be probably scattered into any angles in three dimensions. The phase function $f(\vec{\mathbf{p}}, \vec{\mathbf{q}})$ is used quantify the probability of a photon to be scattered from direction $\vec{\mathbf{p}}$ into direction $\vec{\mathbf{q}}$ (Fig. 2-4)

$$f(\vec{\mathbf{p}}, \vec{\mathbf{q}}) = f(\cos\theta) \tag{2-15}$$

The phase function in a random media is independent on the orientation of the scatter. Except some cases such as muscle and white matter, this assumption is

valid for most biological tissue. Thus Eq. (2-15) can be expressed as a function of the scalar product of the unit vectors in the initial and final directions $(\vec{\mathbf{p}},\vec{\mathbf{q}})$ which is equal to the cosine of the scattering angle $\cos(\theta)$. The *anisotropy factor,* g is then defined as the mean cosine of the scattering angle:

$$g = \int_{4\pi} d(\cos\theta)\cos\theta \cdot d\theta \tag{2-16}$$

If $g = 1$, the scattering is completely forward; if $g = -1$, the scattering is backscattered; if $g = 0$, then the scattering is isotropic.

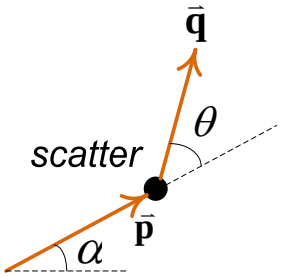

Fig. 2-4 Phase function $f(\vec{\mathbf{p}},\vec{\mathbf{q}})$.

The anisotropy factor g depends on the scatter size, shape and the mismatch of the refractive index between two scatters. Biological tissues are strongly forward scattering medium in NIR regime (650 - 1150 nm) because the anisotropy factor is typically $0.69 \le g \le 0.99$ [11]. For normal breast tissues, the typical values of an isotropic factor is $0.9 \le g \le 0.99$, which means that the light photon almost keep its original direction within a few millimeters propagation. Therefore it is appropriate to reduce the scattering coefficient μ_s by the factor $(1-g)$, which gives the definition of *reduced scattering coefficient* or *transport scattering coefficient*, μ_s' :

$$\mu_s'(\lambda)=(1-g)\cdot\mu_s(\lambda) \tag{2-17}$$

The quantity μ_s' represents the isotropic scattering property. Its reciprocal $\frac{1}{\mu_s'}$ represents the distance that a photon has a probability of $1/e$ to get an isotropic scattering action. The reciprocal can also be interpreted as the free mean path between two consecutive scattering events along photon propagation.

2.1.4 Mean free path

Regarding the absorptive and scattering effects together, one can define a *total attenuation coefficient* as

$$\mu_t=\mu_a+\mu_s \tag{2-18}$$

where $1/\mu_t$ is commonly referred as *mean free path* between any two consecutive light-tissue interaction events. Similarly, one can define the *transport attenuation coefficient*, μ_{tr} as

$$\mu_{tr}=\mu_a+\mu_s(1-g)=\mu_a+\mu_s' \tag{2-19}$$

2.2 Chromophores in breast tissues

Most soft tissues contain a couple of substances that exhibit absorption in NIR regime (650 – 1150 nm). They are known as *chromophores*. In breast tissue, the significant chromphores to NIR light are water, lipids, hemoglobin and melanin.

2.2.1 Water

The absorption spectrum of water in NIR regime is shown as solid line in Fig. 2-5 [13]. At 785 nm and 808 nm, the absorption coefficients are 0.0252 cm^{-1} and 0.0218 cm^{-1}, respectively. In normal breasts, the water concentration varies from 10% - 30%, depending on menstruation and the menopausal status [14-17].

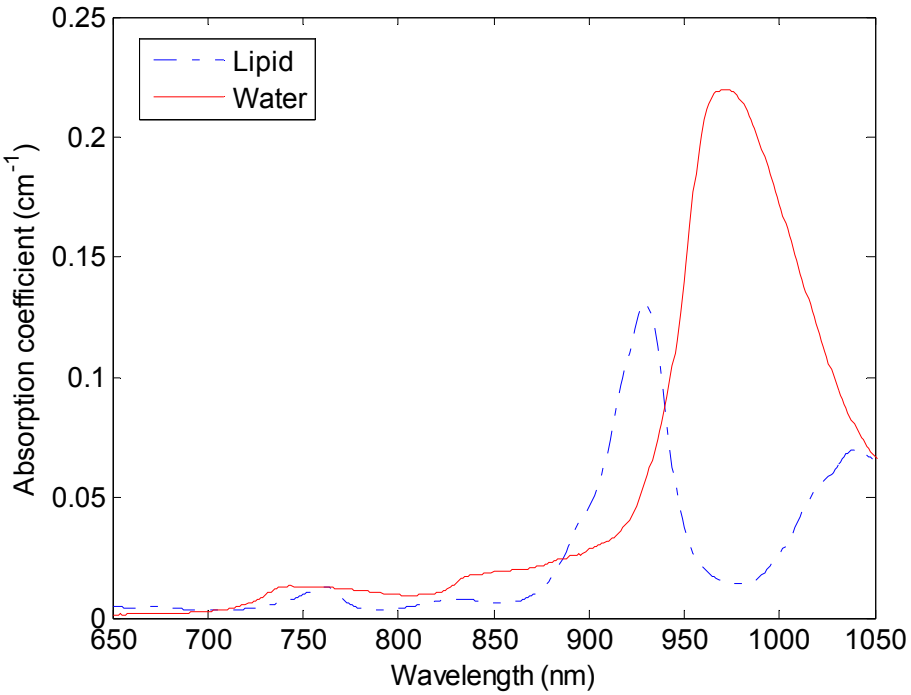

Fig. 2-5 Absorption coefficient of water and lipid in the near-infrared region.

2.2.2 Lipid

Adipose tissue (or fatty tissue) is another dominant constituent in normal breast tissue. Its absorption spectrum is shown in dashed line in Fig. 2-5 [18]. At 785nm and 808 nm, the absorption coefficients of lipid are 0.00357 cm^{-1} and 0.00497 cm^{-1}, respectively. In normal breasts, the lipid concentration is in range 50% - 58%. Such a high concentration leads to an accumulative

absorption which makes lipids one of the dominant absorbers in breast tissues. Meanwhile, its effect will increase with women ageing because older women tend to have less fibrous tissue and more adipose tissue.

2.2.3 Hemoglobin

Oxyhemoglogin (HbO) and deoxyhemoglobin (Hb) are the most significant chromophores in breast tissues because they are highly dependent on the oxygenation level of the blood. Fig. 2.6 shows the molar absorption coefficients of HbO and Hb in the NIR regime (650 nm - 1050 nm) [13]. The differences in the absorption spectra give us a possibility to differentiate these two compounds by using two wavelengths. These two molar absorption coefficients of two compounds cross over at 800 nm. This property means two wavelengths on both sides can be eligible to resolve the concentrations of HbO and Hb.

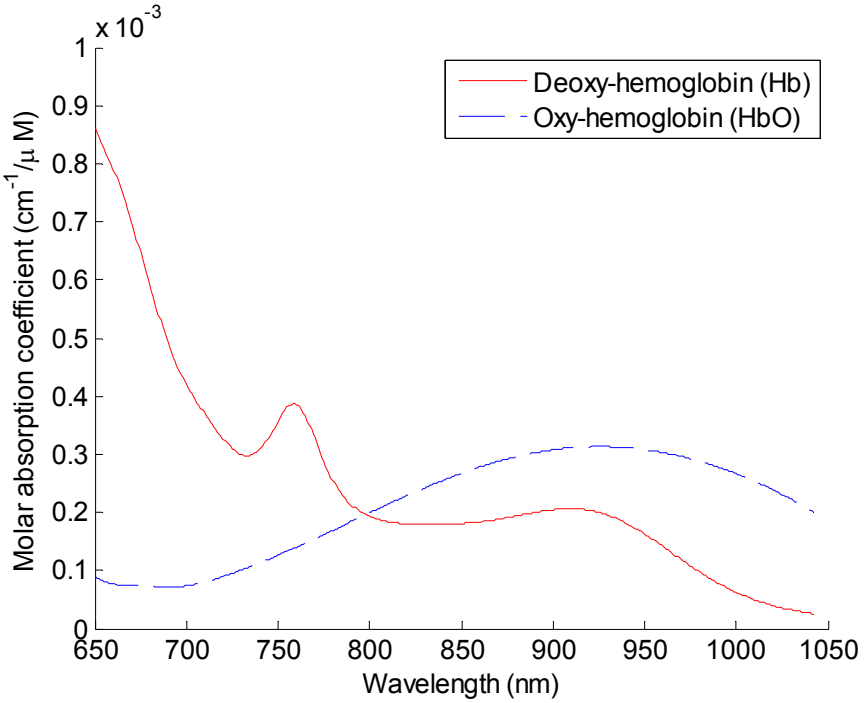

Fig. 2-6 Specific molar absorption coefficient of oxy-hemoglobin (HbO) and deoxy-hemoglobin (Hb).

2.2.4 Other chromophores

In addition to these four major chromphores (water, lipid, HbO and Hb), there are some other minor chromophores coexisting in breasts, such as melanin and cytochrome.

2.2.4.1 Melanin

Melanin is found in cells 'melanosomes' in the epidermis layer of the skin. The concentration of melanin is normally low [19-21]. In NIR window (650 nm - 1050 nm), melanin is a relatively high absorber. However, due to its ultra low concentration and the property of oxygenation independence, its effect upon the overall absorption property can be ignored in breast tissue hemodynamic assessment, with considering to the above four major chromophores.

2.2.4.2 Cytochrome

Like melanin, cytochrome also has a very low but constant concentration in breast. Although it has a relatively high absorption in NIR regime (650 – 1050 nm), its contribution to the overall breast tissue still can be ignored when the hemodynamic matter is analyzed.

For these reasons, we only concern water, lipid, Hb and HbO when analyzing the absorption properties of overall breast tissue. Contributions from melanin and cytochrome will be ignored.

2.3 Optical properties of breast tissues

The human breast tissues are majorly constituted by glandular tissue and fatty tissue. The concentrations of water and lipids normally change only with menstrual status and ageing. However, the concentrations of HbO and Hb are

not stable as water or lipid. They will not only change with age, menstruation state, but also is highly dependent on the local hemodynamic changes. When local vascularization or angiogenesis occur, the corresponding concentrations change of Hb and HbO will become significant.

Therefore, we assumed in this study the wavelength-dependent absorption coefficients of the breast tissue are solely contributed by: water, lipid, HbO and Hb. From Eq. (2-7) we have,

$$\begin{pmatrix} \mu_a^{785} \\ \mu_a^{808} \end{pmatrix} = 2.303 \cdot \left[\begin{pmatrix} \varepsilon_{Hb}^{785} & \varepsilon_{HbO}^{785} \\ \varepsilon_{Hb}^{808} & \varepsilon_{HbO}^{808} \end{pmatrix} \cdot \begin{pmatrix} C_{Hb} \\ C_{HbO} \end{pmatrix} + \begin{pmatrix} \varepsilon_{H_2O}^{785} \\ \varepsilon_{H_2O}^{808} \end{pmatrix} \cdot C_{H_2O} + \begin{pmatrix} \varepsilon_{Lipid}^{785} \\ \varepsilon_{Lipid}^{808} \end{pmatrix} \cdot C_{Lipid} \right] \tag{2-20}$$

where μ_a^{785} and μ_a^{808} are the absorption coefficients of bulky breast tissue at wavelength 785 nm and 808 nm, respectively. ε_{Hb}^{785} ε_{Hb}^{808}, ε_{HbO}^{785} and ε_{HbO}^{808} are molar extinction coefficients of Hb and HbO at 785 nm and 808 nm. $\varepsilon_{H_2O}^{785}$ and $\varepsilon_{H_2O}^{808}$ are molar extinction coefficients of water at 785 nm and 808 nm. $\varepsilon_{Lipid}^{785}$ and $\varepsilon_{Lipid}^{808}$ are molar extinction coefficients of lipid at 785 nm and 808 nm. These extinction values can be obtained in literature [22]. C_{Hb} and C_{HbO} represent the unknown concentrations of Hb and HbO, respectively. C_{H_2O} and C_{Lipid} represent the concentrations of water and lipid, respectively. As the concentrations of water and lipid are normally constant, thus we assumed in this study the relative concentration of lipid was 56%, the water concentration of premenopausal and postmenopausal women were 11% and 26%, respectively [23]. With regarding to these assumptions, we can resolve the

spatial distribution of the absorption coefficient μ_a^{785} and μ_a^{808} from the time-resolved TPSF measurements at 785 nm and 808 nm, respectively.

2.4 Physiological parameter of breast tissues

From Eq. (2-20), we can calculate the physiological parameters C_{Hb} and C_{HbO} simultaneously and get two more physiological parameters. One is *total hemoglobin concentration* (*THC*), which is defined as [11, 21]

$$THC = C_{HbO} + C_{Hb} \tag{2-21}$$

and *blood oxygenation saturation* (*SO*), which is defined as [11, 21]

$$SO = \frac{C_{HbO}}{THC} \times 100\% = \frac{C_{HbO}}{C_{HbO} + C_{Hb}} \times 100\% \tag{2-22}$$

Parameter THC is in unit of micro-molar per liter (μMol/L). It quantifies the blood volume in the breast, which can also be interpreted as the total blood supply in the breast. Parameter SO can be interpreted as the oxygen consumption level of breast tissue. Normally, the local cancerous tissues require much more blood supply and oxygen consumption. This inherent property will significantly alter the positional optical properties as well as the individual physiological parameters alternation of breast tissue. Therefore, the positional differences (inhomogeneities) of μ_a, μ_s', THC and SO can be used to as indicators of breast abnormities.

The average μ_a and μ_s' of normal breast tissue in most recent researches are tabulated in [24, 25]. Although they were resolved by using different methodologies and apparatus, the data shown in Table 2.1 exhibits a uniformity of absorption properties among different studies. The global

average absorption properties of normal breast tissue are found to be 0.04 cm^{-1} at 700 – 800 nm and 0.05 cm^{-1} at 800 – 900 nm. The averaged reduced scattering properties are found to be 8.0 cm^{-1} for both 700 – 800 nm and 800 – 900 nm regimes. These data will be used as reference throughout this research.

Table 2-1 Summary of optical/physiological parameters of normal breast tissue from recent literatures. N refers to the number of subjects involved in different studies. μ_a and μ_s' are rounded properly for consistency

Reference	N	μ_a (cm^{-1})		μ_s' (cm^{-1})		SO (%)	THC (μMol/L)
		700-800 nm	800-900 nm	700-800 nm	800-900 nm		
Durduran [26]	52	0.04 ± 0.03	0.05 ± 0.03	9 ± 0	8 ± 2	68 ± 8	34 ± 9
Grosenick [27]	28	0.04 ± 0.01	0.05 ± 0.02	10 ± 1	8 ± 2	74 ± 3	17 ± 8
Tomas [28]	36	0.04 ± 0.02	0.04 ± 0.02	8 ± 2	8 ± 2	77 ± 8	17 ± 10
Spinelli [29]	50	0.04 ± 0.01	0.10 ± 0.07	11 ± 2	12 ± 0	66 ± 9	16 ± 5
Taroni [30]	101	0.05 ± 0.01	0.05 ± 0.01	11 ± 1	10 ± 1	71 ± 8	20 ± 7
Pogue [31]	46	0.05 ± 0.04	0.05 ± 0.02	10 ± 2	10 ± 2	61 ± 1	22 ± 7
Poplack [32]	23	0.05 ± 0.02	0.05 ± 0.02	12 ± 2	12 ± 2	69 ± 9	24 ± 12
Srinivasan [33]	28	-	-	-	-	58 ± 9	22 ± 8
Suzuki [34]	30	0.05 ± 0.01	0.05 ± 0.01	9 ± 1	10 ± 0	-	-
Global average	-	0.04	0.05	8	8	68 ± 5	21 ± 6

2.5 Early breast cancer

Breast cancer is the abnormalities which most probably occur at ducts (i.e. ductal carcinoma *in-situ*, DCIS) and lobules (i.e. lobular carcinoma *in-situ*, LCIS). Almost 90% breast cancer starts from duct and 10% breast cancer start from lobule. Like other cancers, breast cancer also starts from a single cell. The transformation from a normal cell into a tumor cell is typically a progression from a pre-cancerous lesion to malignant tumors. These changes may be the result of interactions between a genetic factor and the following three external carcinogens:

- Physical carcinogens, such as ultraviolet and ionizing radiation;
- Chemical carcinogens, such as components of tobacco smoke and arsenic;
- Biological carcinogens, such as infections of viruses, bacteria or parasites.

Aging is another very important factor for cancer development because the overall cancer risk is combined with the tendency for cellular repair mechanisms to be less effective as a person grows older.

The breast cancer is diagnostically classified by cancer stages primary on the basis of tumor size, invasiveness or non-invasiveness, whether lymph nodes are involved, and whether the cancer has spread beyond the breast. The commonly used staging system is the 4-stage system.

Stage 0 - the breast cancers is non-invasive. Like DCIS and LCIS, there is no evidence of cancer cells or non-cancerous abnormal cells breaking out of the part of the breast where they started, or

invading neighboring normal tissue. The tumor size is less than 1 cm.

Stage I - the breast cancer normally becomes invasive. The cancer cells breaks though and invades neighboring normal tissue. The tumor size is less than 2 centimeters, and no lymph nodes are involved.

Stage II - the breast cancer at stage II when the tumor size is more than 2 cm, but less than 5 cm across and/or the lymph nodes in the axillary are affected.

Stage III - the breast cancer at stage III when the tumor size is more than 5 cm across and the lymph nodes in the axillary are affected without further spreading.

Stage IV - Breast cancer has spread to other organs of the body - usually the lungs, liver, bone, or brain. The tumor size is larger than 5 cm and can be any size.

Clinically, breast cancer at stage 0, I, II, and some stage III are regarded as "*early*" stage, while other stage III and stage IV are regarded as "later" or "advanced" stage.

Survival rate of breast cancer depends on many factors: cancer type, treatments, lifestyle, and genetics. Table 2-2 shows the statistics of 5-year survival rate survival rates by breast cancer stage. It also shows the survival rate of breast cancer can be improved significantly if cancer at 'early' stage (stage 0, I, II, III) can be cured than the 'later' stage (stage III, IV). Therefore, women at 40s and above are strongly invited to attend routine breast cancer screening [35, 36] after tissue constituents start altering.

Table 2-2 Average 5-year surviving rate of breast cancer at each stage

	Stage	US *	Singapore #
Early	0	100%	90%
	I	100%	75%
	II	81%~92%	60%
Later	III	54%~67%	50%
	IV	20%	50%

* American College of Surgeons National Cancer Data Base from 1995-1998. http://www.breastcancerandtreatment.com/Breast_Cancer_Survival_Rate.html

Data source: http://www.singaporecancersociety.org.sg/lac-fcb-classifications.shtml

Chapter 3. Breast Tissue Imaging

This chapter reviews the pros and cons of *non-optical* structural imaging modalities for breast examination and diagnosis, including X-ray mammography, MRI and ultrasound. The emphasis is placed on the novel non-invasive *optical* imaging modalities, especially the diffuse optical tomography (DOT) and the time-resolved diffuse optical spectroscopy (DOS) techniques.

3.1 Biomedical imaging modalities

The most commonly used biomedical imaging modalities for breast imaging and diagnoses include X-ray mammography, MRI and ultrasound.

3.1.1 X-ray mammography

The X-ray radiation can penetrate most biological tissues (e.g. the breast tissue) with little attenuation. When X-ray is used for breast screening, it is called X-ray mammography. The imaging of the absorption properties (namely mammograms) are used to find potential signs of breast cancer such as tumors, small clusters of calcium (microcalcifications) and abnormal changes in the skin.

The imaging contrast of the mammogram is not only depended on the distribution of absorptive substance in the tissues, but also the thickness of breast that the X-ray will go through. Healthy breast tissues are normally constituted by fat and the glandular tissues, such as ducts and lobules, which lead to a medium dose exposure. At cancerous conditions, the absorption of

breast tissue to the X-ray radiation is limited by the microcalcification. In order to obtain an optimal imaging contrast and minimize the ionization hazard, the breasts are normally compressed in between two transparent plates during screening. The thickness between two parallel plates is normally 2-8 cm, which enables high contrast whilst keeping the ionization dose within an acceptable level. Such breast suppression might cause discomfort to patients, which requests the screening finish as quick as possible. Most current mammography imaging can be finished in 15 (film mammography) - 30 minutes (digital mammography).

Until now, the X-ray mammography is still called '*gold standard*'. It can find cancers at early stage, when they are small and most responsive to treatment. Meanwhile, X-ray mammography has a good imaging contrast of benign tumors like cyst, fibroadenomas, macrocalcification to malignant tumors such as the invasive microcacification.

For young women with dense breast tissues, the attenuation of the glandular tissue to the X-ray radiation is higher, which induces difficulties for X-ray mammograms to distinguish benign and malignant tumors. As women ageing, the glandular tissue is gradually supplanted by fat so that the breast density gradually decreases. This physiological change reduces the absorption of the breast to the X-ray radiation, which would increase the imaging contrast. For most of the past two decades, the American Cancer Society has been recommending women age 40 and older should have an annual screening mammogram and should continue to do so for as long as they are in good health.

Due to the high false-positive rate, many women have to undergo follow-up biopsy, leading to unnecessary physical and psychological morbidity. Additionally, X-Ray mammography causes extra ionization radiation and has limited benefit for younger women with dense breast. Table 3-1 summarizes the pros and cons of X-ray mammography for breast cancer imaging.

Table 3-1 Advantage and disadvantages of X-ray mammography for breast cancer imaging

Advantages	Disadvantages
• High differentiation capability among benign and malignant cancers; • High sensitivity and high resolution; • High detection rate for early stage breast cancer (~95%). • Large penetration depth; • Relative low cost;	• Low contrast on high dense breast tissue; • Potential ionizing radiation hazard; • Discomfort to patients because of the breast compression; • Long projection time; • Relatively high false-positive rates; • Accuracy is affected by the silicone implantations;

3.1.2 MRI

The phenomenon of nuclear magnetic resonance (NMR), when used in imaging, is called magnetic resonance imaging (MRI).

3.1.2.1 Nuclear magnetic resonance (NMR)

Nuclei have an intrinsic quantum property called spin. For those atoms with odd number of protons, such as the hydrogen atom, the nucleus spinning forms small magnetic moments (Fig. 3-1). In a thermal equilibrium, all protons move in a random direction and the magnetic moment of each proton are randomly oriented. The overall magnetic moment or net magnetic moment is zero.

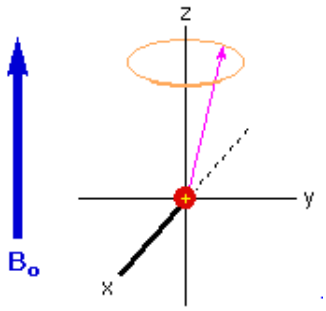

Fig. 3-1 Spin of nuclei in an external magnetic field B_0.

In human body, water proportion is approximately 60%. The abundance of the hydrogen atoms with only one proton is used for imaging by MRI. Placing the human body into a magnetic field with magnetic field intensity of B_0, the randomly moving hydrogen atoms in thermal equilibrium will be lined up along the applied magnetic field. Half of the hydrogen atoms will be lined up with orientation along the magnetic field at a lower energy state. Another half of hydrogen atoms are lined up against the magnetic field at a higher energy state. The atoms number at lower energy state is slightly more than the atoms at high energy state. These excess number of protons result in a net magnetic moments, whose Larmour frequency is proportional to the magnetic field B_0 (e.g. $42.57 B_0$ MHz for hydrogen nucleus). When another radio frequency (RF) pulse with same Larmour frequency is radiated to the human body in a direction perpendicular to the magnetic field, the protons absorb the energy and spins are knocked out of alignment with B_0 (see Fig. 3-2). When the excited RF energy ceases, excited spins return to their initial state soon, emitting a radio frequency signal. The amplitude of the emitting signal depends on the number of protons in resonance. These signals are picked up

by coils placing around the body, from which the proton density (known as spin density, SD) varying among tissues can be visualized. It is this resonant radiation that constitutes the signal in NMR.

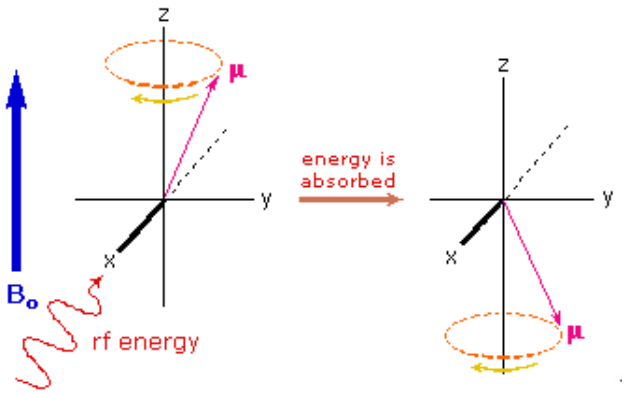

Fig. 3-2 Spin of nuclei flips after it absorbs a photon at its Larmor frequency.

3.1.2.2 Magnetic resonance imaging (MRI)

MRI differs from NMR in that an image is obtained. Normally in NMR, a single uniform magnetic field B_0 is applied to the whole sample. There is no way to determine where a given proton with its signatures of relaxation times is located. By imposing a spatially varying magnetic field, i.e. a magnetic field gradient upon the constant magnetic field B_0, one can obtain a range of proton resonant frequencies. Each is dependent on the position of the particular proton within the body.

Slice selection is accomplished by using a frequency-selective pulse applied simultaneously with on the magnetic field gradient. The slice selection direction, x, y and z determines the orientation of coronal, sagittal, and axial of the image.

3.1.2.3 Breast MRI

Most MRI techniques for breast imaging use a contrast material called Gadolinium DTPA (Gd-DTPA), which is injected intravenously into arms before or during the examination to improve the image quality. Gd-DTPA's paramagnetic property would reduce the T1 relaxation time (and to some extent the T2 and T2* relaxation times) in NMR. It is this property that helps MRI to get a stronger and clearer image to "highlight" any abnormalities.

The increased vascularity of tumors normally produces a preferential uptake of agent (Gd-DTPA). This effect can be used to improve the contrast of tumors from the surrounding normal tissue. If MRI scans are repeatedly acquired along with the contrast injection, the dynamic nature of between the normal and cancerous tissue can be differentiated. This is called dynamic contrast-enhancement MRI.

As an example, Fig. 3-3 illustrated a 1.5-Tesla breast MRI developed by Siemens company which provides a bilateral imaging capability for both breasts imaging The total imaging time can be reduced to about 30 minutes compared from 60 minutes required by conventional MRI which utilizes lateral imaging technique [37, 38].

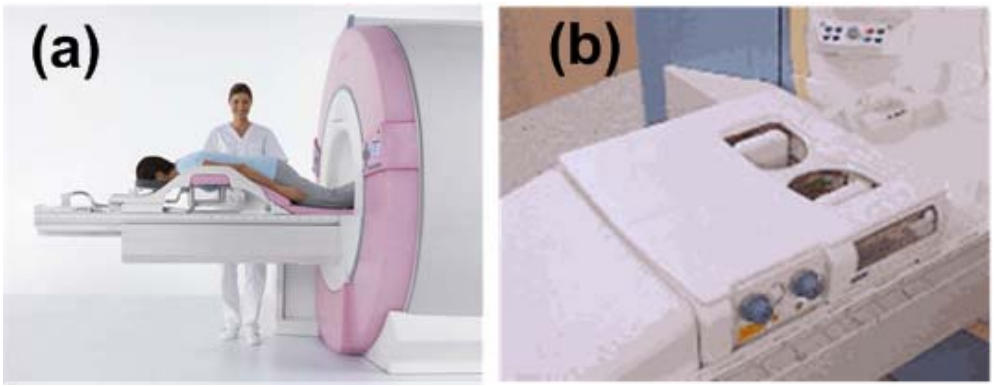

Fig. 3-3 Magnetom Espree-Pink, a 1.5-Tesla MRI dedicated for breast imaging. (a) Instrument overview. (b) Breast array coil for bilateral breast imaging.

3.1.2.4 Pros and Cons of breast MRI

MRI is a very useful diagnostic tool for breast cancer detection when works in conjunction with X-ray mammography. It has been proven to be remarkably effective to image the augmented breast. MRI can also be used effectively to gain information about breast abnormalities detected with mammography, physical examination, or other breast imaging modalities. Because of the high sensitivity, the American Cancer Society also recommended that young women at very high risk of the disease receive annual MRI exams in addition to annual mammograms. MRI may also useful for women who have been diagnosed with breast cancer to detect cancer in the opposite breast, to evaluate treatment options, and to follow-up after treatment has been completed. Table 3-2 summarizes the pros and cons of MRI breast cancer diagnosis.

Table 3-2 Advantages and disadvantages of MRI for breast cancer imaging

Advantages	Disadvantages
• Non-ionization hazard; • Effective for dense breast; • Can image breast implants/ruptures; • Can detect residual cancer and recurrence of cancer after lumpectomy; • Useful for high-risk women; • Can provide high resolution (typ. 0.5 mm) imaging details on axial plane, coronal plane, and sagittal plane; • Functional imaging to study the blood flow (angiography). • Can image deep internal organs and tissues that are inaccessible to mammography.	• Expensive; • Requires agent injections (Gadolinium) for imaging contrast; • Can not detect microcalcification at early cancer stage; • Unsuitable for patient with claustrophobia; • Relatively long scanning times compared with X-ray mammography; • Relative high false positive ratios, resulting in unnecessary biopsies; • Long imaging time (30-60 min) than X-ray mammography (15-30 min).

3.1.3 Ultrasound

In medical applications, the ultrasound with frequency from 1 MHz to 30 MHz is widely used. Since the normal breast tissue is constituted by fat and glandule, the sound wave in breast tissue can get a speed of 1550 m/s, with a variation about ±6%. Thus for ultrasound frequency from 1 MHz to 30 MHz, the wavelength is from 1.5 mm to 0.05 mm and the spatial resolution is typically in the order of millimeters [39].

For breast imaging, a hand-held transducer is used as the ultrasound wave source, in which a piezoelectric crystal is driven to generate the ultrasound wave with frequency from 1 to 15 MHz. These ultrasound waves are generated intermittently. The pulse width is shorter (normally <1 us) than the repetition time (normally > 1ms). Because the acoustic impedances of air (0.0004 MRayl) and breast tissue (1.38 MRayl) are very different, almost 100% of the sound wave will reflect back. To increase the percentage of the transmission, an impedance matching medium (usually a gel) is smeared on the breast before scanning. The ultrasound wave transmitting inside the breast tissue will be reflected back once it encounters an acoustic impedance mismatch. Taking the fluid filled cyst as an example, its acoustic impedance is larger (1.48 MRayl) than the surrounding fat (1.38 MRayl). Thus at the cyst-fat boundary, 23% of the ultrasound wave will be reflected back and detected by the transducer. This effect greatly improves the imaging contrast between the cystic tissues and the surrounding tissues, which makes ultrasound particularly useful for detection of these kinds of lesions. Meanwhile, for young women who have dense breast, ultrasound offers an effective approach to detect these lesions, where the mammography is often unsuitable. This capability makes breast ultrasound a useful complementary examination to the X-ray mammography.

In addition, the Doppler Effect describes the frequency difference generated from still and moving targets. This effect is utilized in medical ultrasound to monitor the hemodynamic of blood flowing. Regarding to breast cancer detection, the Doppler ultrasound can monitor the blood flow and so can be an indicator of vasularization of a malignant tumor in the breast.

Table 3-3 summarizes the advantages and disadvantages of the medical ultrasound technique for breast imaging.

Table 3-3 Advantages and disadvantages of medical ultrasound for breast imaging

Advantages	Disadvantages
• Relatively cheap; • Imaging in real-time; • Portable; • Non-ionization hazard; • Can yield vascularization information by applying Doppler Effect; • Suitable for dense breast; • Suitable for cystic lesions detection; • Excellent contrast resolution; • Supplementary to the mammography; • Can be used to accurate guide for biopsy; • Complement to the mammography	• Not suitable for LCIS; • Not suitable for calcification; • Highly depended on operator's skill; • High false positive/negative rate from time-to-time; • Prominent image artifacts; • Not suitable for obese patient; • Limited resolution (in millimeters range); • Can not provide volume information;

3.1.4 From non-optical imaging modality to optical imaging modality

In addition to X-ray mammography, MRI and ultrasound, there are recently some other useful imaging modalities [40, 41] like contrast-enhanced breast MRI [42-44], clinical breast magnetic resonance spectroscopy (MRS) [45], radionuclide imaging like single photon emission computed tomography (SPECT) [46] and positron emission tomography (PET) [46], near-infrared optical imaging [47], diffuse optical imaging (DOT) [48, 49], diffuse optical spectroscopy (DOS) [14, 15, 17, 50-54], near-infrared imaging fluorescence [55] . There are also various kinds

of hybrid imaging modalities available, like PET-CT [46], MRI-PET [56], X-ray-DOT [57], Ultrasound-DOT [58, 59] and so on. Although these new imaging modalities have demonstrated promising results on breast cancer imaging, they are still unable to match the performance of X-ray mammography for routine screening [60]. In more cases, these imaging modalities play a supporting role to supplement X-ray mammography by providing more detailed information from other perspectives. For example, the main limitation of X-ray mammography is that it has a poor specificity for tumor type so that it is not suitable for dense breast tissue. This shortcoming can be compensated by MRI, ultrasound and other imaging modalities which provide additional information for tumor diagnose and thus reduce unnecessary biopsies.

Among these supplementary imaging modalities, optical imaging modalities have a unique imaging capability for non-invasive breast cancer detection. In the following part, emphases are placed on this new imaging modality.

3.2 Non-invasive optical imaging modalities

3.2.1 Introduction

Biomedical optics for breast tissue imaging (also named optical mammography) make use of the near-infrared (NIR) illumination. This principle has got fast development both on academia as well as in the industrial R&D laboratories in the last decades. Comparing with those non-optical imaging modalities, the optical modality offers a couple of advantages, which make it extraordinarily suitable for non-invasive breast tissue examination and diagnoses.

- First of all, the optical imaging is a very safe and very comfort imaging modality for breast imaging. Using low dose of NIR light for illumination, ionization hazard will not happen at all. Patients could repeat imaging examination frequently without worrying about any radiative harm.
- Second, optical imaging modality is non-invasive. No extra contrast agent is used. This advantage greatly releases patients' morbidity.
- Third, optical imaging provides excellent contrast in terms of optical properties (commonly by absorption coefficients and scattering coefficients) among various tissues types. This feature makes optical imaging a very useful tool to compensate X-ray mammography for dense breast tissues.
- Forth, optical imaging using multiple wavelengths and can be utilized for NIR spectroscopic application, through which the optical properties of each specific chromophores (especially the oxygenated hemoglobin, HbO and the deoxygenated hemoglobin, Hb) can be quickly quantified. The quantification of these two significant chromophores offers an approach to assess tissues' angiogenesis and vascularization.

Nowadays, the optical imaging modalities for breast cancer imaging and diagnosis mainly focus on two application fields. One application field is near-infrared optical spectroscopy [15, 17, 51-54, 61-66]. The other application field is near-infrared optical imaging [14, 15, 23, 26, 27, 29, 65, 67-72]. In addition to breasts, optical imaging is also widely used to research the brain functional imaging [16, 73-78], arms imaging [69, 79-81], brain trauma monitoring and surgical interventions [82-87].

In the optical imaging applications, the optical properties commonly in interest are absorption coefficient μ_a and reduced scattering coefficients μ_s'. Choromophores in breast tissue at different concentration has corresponding characteristic absorption spectra and scattering spectra. Concentration of these chromophores in normal and cancerous tissues will be different. Quantifying these differences among chromophores could help we well understand the health of the breast tissue.

3.2.2 Photon transportation in tissue

In most optical imaging and spectroscopy application in biomedical system the light -tissue interactions should be taken into account. When a collimated NIR beam shines on the tissue's surface, some optical energy will reflected back into air and the remaining energy will go into the tissue. In breast tissue, the water, lipid, and hemoglobin may either cause photons to be absorbed, keeping propagating in its original direction, or change it propagating direction by elastic scattering.

Although the interaction between photon and the biological cell membrane unpredictably change the photon propagation direction, the behavior of vast photons passing though a scattering tissue will follow an underlying statistics. The photon propagation track inside the tissue can be classified into 3 types: ballistic, snake and diffused [87] (Fig. 3-4).

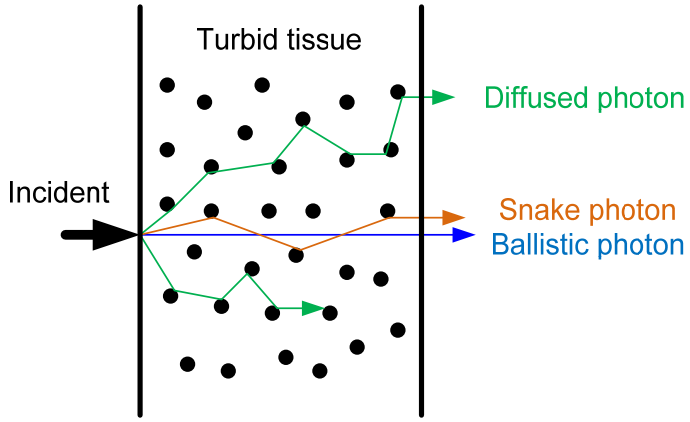

Fig. 3-4 Tissue-optic interactions of NIR light photons.

- *Ballistic* photons

As shown in Fig. 3-4, unscattered photons and photons undergoing forward scattering constitute the group of *ballistic* photons (photons travelling straight along the direction of the incident laser beam).

- "*Snake*" photons

The group of "*snake*" photons is composed by the photons that undergo a few elastic scattering events during transmission. The snake photons constitute the first measureable part on the time-resolved signals.

- *Diffused* photons:

The group of *diffused* photons is very intensive. It contains the majority of the incident photons after they have participated in many scattering events. The diffused photons carry information of the scattering properties of the medium.

3.2.3 Photon detection

With considering on target's shape, for example, the cone shape of breast, different detection geometries should be taken into account to detect the optical signal. Two illumination-detection layouts are commonly used, as

shown in Fig. 3-5 and Fig. 3-6 respectively. The detection layouts in Fig. 3-5 records the transmitted photons (i.e. in a transmission mode) while the detection layout in Fig. 3-6 takes advantages of their backscattering (reflective mode). In the transmission mode, the source fibers and the detectors (normally fiber and photodiode, etc) are placed on the opposite sides of the tissue slab. In the reflective mode, the source and the detector are placed on the same sides. For the transmission mode, the breasts normally need to be slightly suppressed to decrease the thickness. But for the reflective mode, the breast suppression is not required.

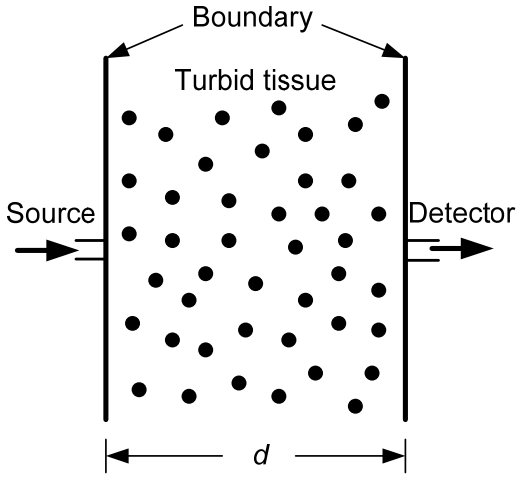

Fig. 3-5 Transmission mode: light source fibers and detectors are placed on opposite sides of tissue slab.

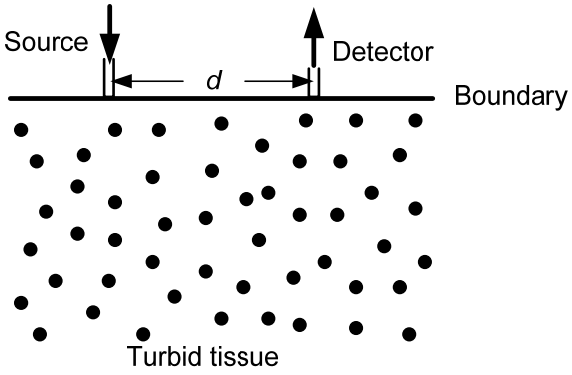

Fig. 3-6 Reflective mode: light source fibers and the detectors are placed on the same side of tissue.

3.2.4 Model of the photon transportation in biological tissue

This subsection describes the biophysical models of light propagation in tissues. The focus was placed on the *forward* and *inverse* problems for a semi-infinite boundary condition because the prototype system reported in this thesis is working on the reflective mode. The in-depth mathematical and physical derivations of these subjects can be found in publications [12, 88].

3.2.4.1 Diffusion equation

The optical propagation in the turbid medium can be described using the *diffusion equation,*

$$D\nabla^2\phi(\mathbf{r},t)-\mu_a\phi(\mathbf{r},t)=-\frac{1}{c}\frac{\partial\phi(\mathbf{r},t)}{\partial t}-S(\mathbf{r},t) \tag{3-1}$$

$$D=\frac{1}{3(1-g)\mu_s}=\frac{1}{3\mu_{st}}=\frac{l_{tr}}{3} \tag{3-2}$$

where D is the photon diffusion coefficient, g is the isotropic factor, $\mu_{st}=(1-g)\mu_s=\mu_s'$ is the linear transport coefficient, and $l_{tr}=\frac{1}{\mu_{st}}$ is the transport mean free path. μ_s is the scattering coefficient. c is the light speed in the tissue. $\phi(\mathbf{r},t)$ is the measurable fluence rate. t is time and $\mathbf{r}$ is the spatial position of the detector. $S(\mathbf{r},t)$ is the light source in the medium [89, 90].

The diffusion equation is essentially an energy conservation equation, where absorption + flow + diffusion = sources.

The diffusion equation is valid to describe the photon propagation in the medium with two prior assumptions [12]:

- The scattering effect is dominant over the absorption effect.

- The distance from source-to-detector should be sufficient large.

For most biological tissue, the scattering properties are usually much stronger (more than 100 times greater) than the absorption properties ($\mu_s >> \mu_a$), that means the photons will be almost isotropically scattered. For human breast tissue, the scattering coefficient (normally μ_s = 8.0 cm^{-1}) is 160 times greater than the absorption coefficients (normally μ_a = 0.05 cm^{-1}) [11], which validates the 1st assumption [91-93].

The 2nd assumption actually depends on the tissue probing setup. In this research, we designed a hand-held probe, which mounts the source fibers and detection fibers with separation more than 1 cm. These separations allow the photons experience multiple scatterings before reaching the detection fibers.

Overall, the research work in this thesis is based on the diffusion equation. The solutions to the diffusion equation can be classified into analytical methods and numerical methods [94-96]. The numerical solutions commonly make use of the Monte-Carlo (MC) method [93 97, 98 99 100] and the finite element method (FEM) [101 102]. The analytical approaches mostly focus on the Green's functions. In this study, the analytical solutions are adopted. Details of the numerical and analytical solutions to solve the diffusion equation can be found in a couple of literatures [12, 93, 96, 103, 104].

3.2.4.2 Analytical solutions

The analytical solution to the time-dependent diffusion equation can be classified into three different types with regarding to the medium geometries: infinite medium, semi-infinite medium and finite slab medium [105]. For different medium, different boundary conditions are applied. Therefore the

solutions to the diffusion equation have different forms [12, 104]. All of them are discussed below.

3.2.4.2.1 Infinite boundary condition

For a layout of source-detector pair (optode) in an infinite medium shown in Fig. 3-7, we assume that only the fluence rate $\phi(\mathbf{r},t)$ become small at very long distances away from the source. Then the Green's function to the diffusion equation due to a pulsed laser at an unit energy emitted from the origin at time $t-t'$ is [12]

$$\phi(r,t-t') = \frac{1}{[4\pi Dc(t-t')]^{\frac{3}{2}}} \exp\left[-\frac{r^2}{4Dc(t-t')} - \mu_a c(t-t')\right]. \qquad (3\text{-}3)$$

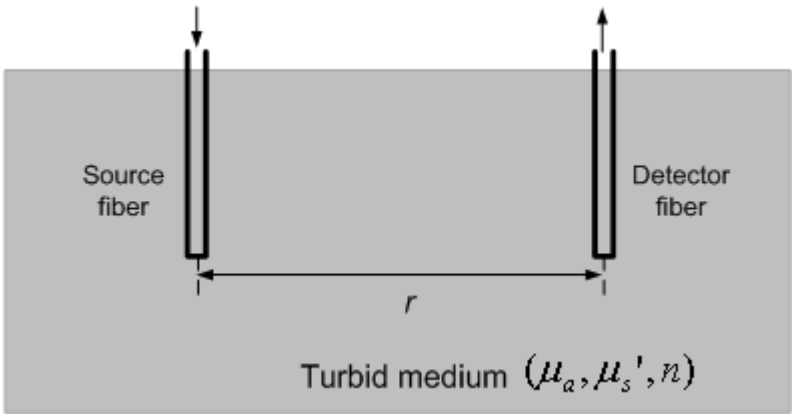

Fig. 3-7 Light source and detector in infinite boundary medium.

3.2.4.2.2 Semi-infinite boundary condition

The semi-infinite boundary condition showing in Fig. 3-8 assumes the boundary extend to infinite in direction of $z<0$. An effective isotropic point light source (called '*real*' light source), which can be thought of as simulating a narrow collimated laser beam incident at $z_0 = 0$, is placed at depth $z_r = \frac{1}{\mu_s'}$

interpolated into the medium. A so-called '*image*' counterpart of the real source is formed by the reflection of the real source about the plane of the "extrapolated boundary". In combination with the boundary condition $\phi(z = z_b, t = 0) = 0$, one can get the analytical solution for detectors located on the surface of the semi-infinite medium, as [12, 87, 106]

$$\phi(r, t - t') = \frac{1}{[4\pi DC(t - t')]^{\frac{3}{2}}} \times \exp[-\mu_a c(t - t')] \cdot \left[\exp\left(\frac{-r_1^2}{4Dc(t - t')} \right) - \exp\left(\frac{-r_2^2}{4Dc(t - t')} \right) \right]. \tag{3-4}$$

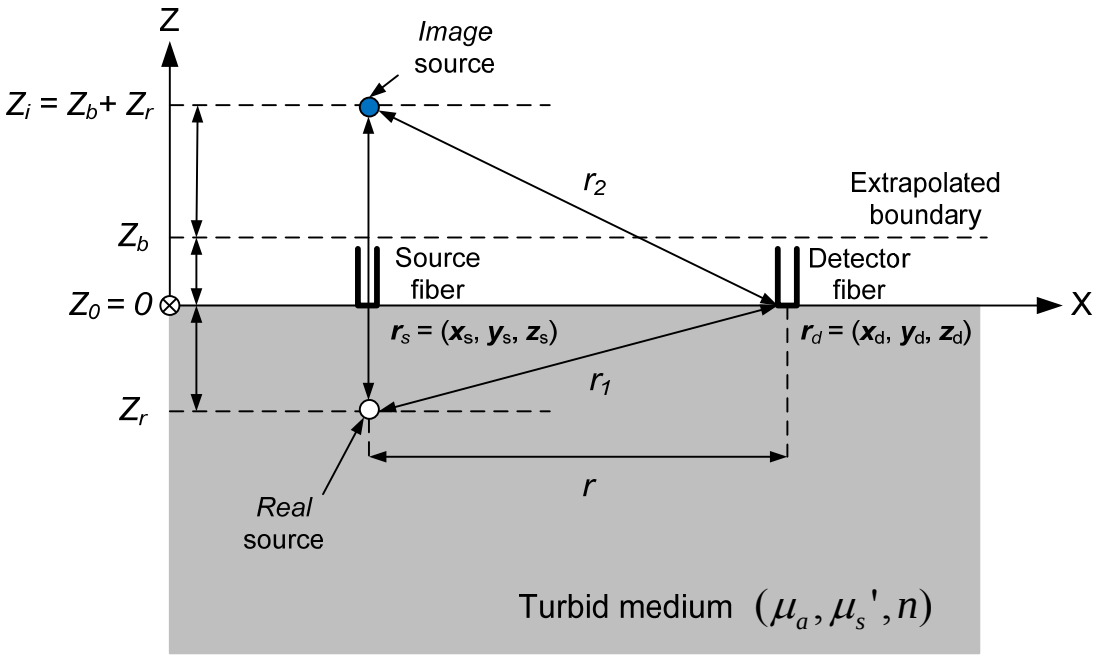

Fig. 3-8 Light source and detector in a semi-infinite boundary medium.

where $r = \left[(x_d - x_s)^2 + (y_s - y_d)^2 \right]^{1/2}$ is the radial distance from the input source fiber to the detection fiber in the *x*-*y* plane. $r_1 = \left(r^2 + z_r^2 \right)^{1/2}$ is the distance from the real light source to the detector fiber. $r_2 = \left[r^2 + (2z_b + z_r)^2 \right]^{\frac{1}{2}}$ is the distance from the image light source to the detector fiber. Here $z_b = \frac{(1 + R_{eff})}{(1 - R_{eff})} \times \frac{2}{3\mu_s'}$ is the distance of the extrapolated boundary to the real

boundary and R_{eff} is the effective reflection coefficient on the interface [107, 108, 109, 110].

$$R_{eff} = -\frac{1.44}{n_r^2} + \frac{0.71}{n_r} + 0.608 + 0.0063 n_r \tag{3-5}$$

where $n_r = \frac{n_{in}}{n_{out}}$, the ratio of the refraction index of the "inside" medium to the "outside" medium. The values of R_{eff} for different interfaces can be found in literature [104].

3.2.4.2.3 Slab medium solutions

The solution to a finite slab boundary, as showing in Fig. 3-9 can be described using approximate boundary conditions $\phi(z=0, t=0)=0$. Then fluence reflectance is give by [12, 106].

$$\phi(r,d,t-t') = \frac{1}{[4\pi DC(t-t')]^{\frac{3}{2}}} \times \exp\left[-\frac{r^2}{4Dc(t-t')} - \mu_a c(t-t')\right] \cdot$$

$$\left\{ z_0 \exp\left(-\frac{z_0^2}{4Dc(t-t')}\right) - (2d - z_0)\exp\left[-\frac{(2d-z_0)^2}{4Dc(t-t')}\right] \right.$$

$$\left. + (2d + z_0)\exp\left[-\frac{(2d+z_0)^2}{4Dc(t-t')}\right] + \ldots \right\}. \tag{3-6}$$

Similarly, the fluence transmission is given by

$$\phi(r,d,t-t') = \frac{1}{[4\pi DC(t-t')]^{\frac{3}{2}}} \times \exp\left[-\frac{r^2}{4Dc(t-t')} - \mu_a c(t-t')\right] \cdot$$

$$\left\{ (d - z_0)\exp\left(-\frac{(d-z_0)^2}{4Dc(t-t')}\right) - (d + z_0)\exp\left[-\frac{(d+z_0)^2}{4Dc(t-t')}\right] \right.$$

$$+(3d-z_0)\exp\left[-\frac{(3d-z_0)^2}{4Dc(t-t')}\right]-(3d+z_0)\exp\left[-\frac{(3d+z_0)^2}{4Dc(t-t')}\right]+\ldots\Bigg\}. \quad (3\text{-}7)$$

where d is the thickness of the finite slab. In Eq. (3-4), extrapolated boundary condition is used to describe single boundary. However, the slab medium showing Fig. 3-9 has an additional boundary. The boundary condition $\phi(z=0,t=0)=0$ can be met by adding two sources near $z=2d$ as shown in Fig. 3-9. However, the boundary condition at $z=0$ is violated for $t=2d/c$. Both boundary conditions above can be met at all times only by adding an infinite number of dipole sources. Thus the measurable reflectance and transmission fluencies emitted from slab medium can be described by Eq. (3-6) and Eq. (3-7), respectively [12, 106].

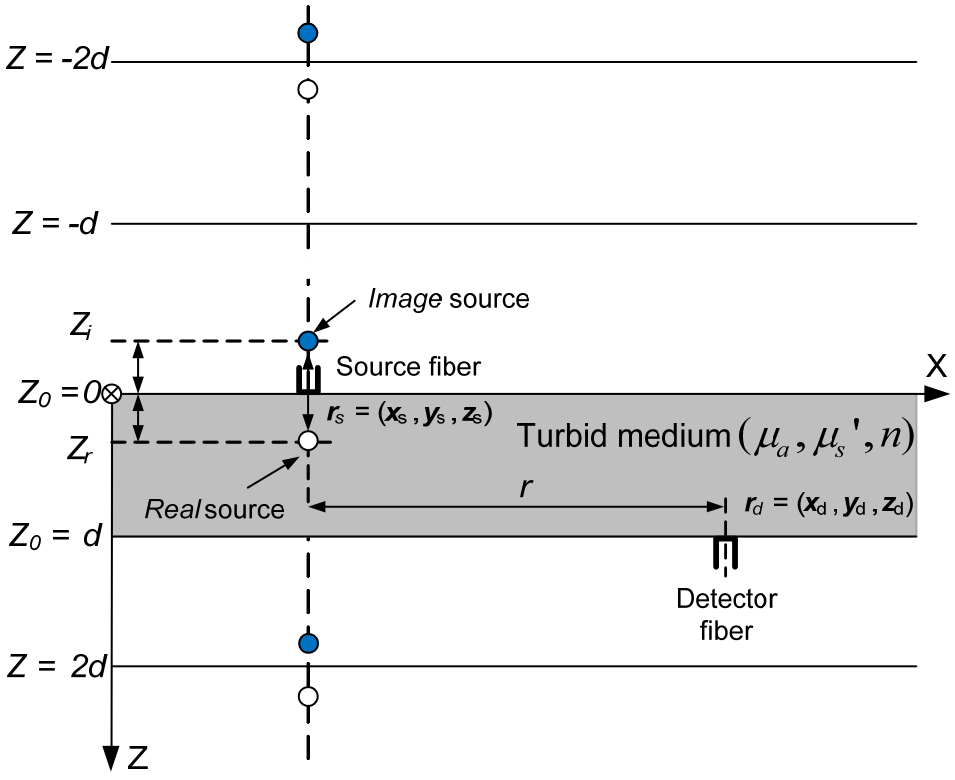

Fig. 3-9 Light sources and detectors in a finite slab medium.

The derivation of analytical solution under the three main boundary conditions involves the superimposing of the Green's functions. Taking the semi-infinite boundary as an example (Fig. 3-8), the temporal point spread functions (TPSF) for the optical properties μ_a = 0.05 cm^{-1} and μ_s' =10 cm^{-1} is normalized and shown in Fig. 3-10. Analytical solutions for other complex geometries, such as spheres and cylinders are explored by literatures [12, 104, 111]. Although there are no general solutions for inhomogeneous media, analytical expressions have been derived, which are capable of incorporating a single point-like absorbing perturbation into an otherwise homogeneous medium.

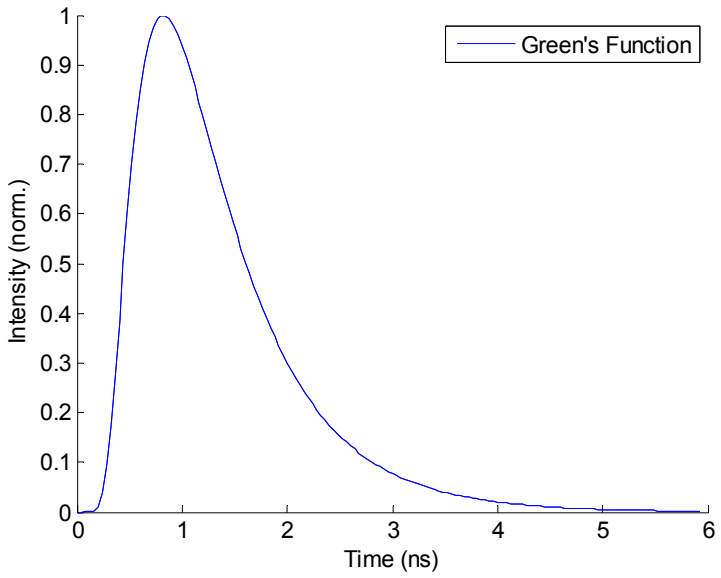

Fig. 3-10 A typical temporal point spread function (TPSF) calculated using Green's function from a semi-infinite boundary.

3.2.5 Image reconstruction

DOT imaging modalities aim to quantify and map the difference of optical properties between normal and abnormal tissues by determining the optical properties of the theoretical values acquired from the same setup used for

experiment. This can be realized by solving the *forward* model and the *inverse* problem.

3.2.5.1 Forward model

The forward model of DOT imaging can be described in equation:

$$Y = J \cdot X \tag{3-8}$$

where Y is the signal which can be got from experiments, X is the known optical property of object, and J is *Jacobian* matrix (or weight matrix). Given the prior information of spatial arrangements of light sources and detectors (optodes) and the optical properties of objects under illumination, the value of Y can be calculated.

3.2.5.2 Inverse problem

To get the unknown optical properties of the target under investigation, we should resolved X by inverting Eq. (3-8) as,

$$X = J^{-1} \cdot Y \tag{3-9}$$

where Y represent the measurements data (e.g. TPSF data) acquired from the DOT experiments, X represents the optical properties to be uncovered and J^{-1} represents the inversion of Jacobian matrix.

3.2.5.3 Image reconstruction

3.2.5.3.1 Perturbation theory

According to the perturbation theory, a small change in the object (e.g. the presence of heterogeneous optical properties in the homogeneous background) will consequently lead to a corresponding change in the data acquired. This change can be expanded in a series from the known function describing the

original state of the object. The measurements Y acquired from light source n and detector m for the objects with optical properties X can be described in Taylor series,

$$\Delta Y_{(n,m)} = \frac{\partial Y_{(n,m)}}{\partial x}\Delta x + \frac{1}{2!}\frac{\partial^2 Y_{(n,m)}}{\partial x^2}(\Delta x)^2 + \cdots \tag{3-10}$$

where $x = \begin{bmatrix} \mu_a \\ \mu_s' \end{bmatrix}$ is the distribution of optical properties throughout the object.

If we neglect the terms above the first derivative and rearrange Eq. (3-10), we have

$$\frac{\Delta Y_{(n,m)}}{\Delta x} = \frac{\partial Y_{(n,m)}}{\partial x} = J_{(n,m)} \tag{3-11}$$

where the values of $J_{(n,m)}$ over the volume of the object is known as the photon density measurement function (PDMF) [112], which maps the magnitude of the change in the measurements Y that results from a unit change in optical prosperities x at position r for a source-to-detector pair (n, m). The Jacobian matrix J is composed by all the derivatives of $J_{(n,m)}$ for all source-to-detector pairs at all volume voxels.

3.2.5.3.2 Linear image reconstruction

The linear reconstruction is the simplest way to reconstruct 2-D/3-D images. For the measurement differences induced by the heterogeneity presence in a homogeneous background, Eq. (3-11) can be rewritten as

$$\Delta Y_{(n,m)} = J_{(n,m)}\Delta x \tag{3-12}$$

If the optical properties perturbation is small, one can solve the above equation by inverting the Jacobian matrix J after calculating the homogeneous

background (forward model). To invert Jacobian matrix, there are several features which may complicate the process:

1) The matrix is ill-posed, which means the independent measurement is less than the unknown voxel numbers;
2) The matrix is ill-conditioned, which means the condition number is typically very large, resulting in the magnification both of measurement errors and numerical errors on inversion.

In order to solve these errors, DOT imaging reconstructions make use of methods like singular value decomposition or *Tikhonov* regularization. The latter one can improve the matrix's condition by adding an identity matrix I with a weight factor λ . i.e

$$\Delta x = \left[J^T \cdot J + \lambda I \right]^{-1} \cdot J^T \cdot \Delta y \tag{3-13}$$

The advantage of linear reconstruction is that it does not require a good forward model to be derived for achieving reasonable results. The main disadvantage is that it is can only reconstruct small changes in the optical properties. In this thesis research, linear image reconstruction, especially the *Tikhonov* method is adopted for image reconstructions.

3.2.5.3.3 Non-linear image reconstruction

Non-linear reconstruction involves generating a forward model, comparing its predictions with the experimental data and updating the sensitivity matrix to minimize the difference. This process is repeated iteratively until the model data is within an acceptable degree of the experimentally measured data.

3.2.6 Optical instrument types

This section reviews three diffuse optical imaging techniques and their instrumentations: continuous-wave, frequency-domain and time-domain.

3.2.6.1 Continuous-wave method

3.2.6.1.1 Principle

Continuous illumination of breast or 'diaphonography' is used to produce shadow images. It was firstly introduced by Culter in 1929 [113]. In 1977, Jöbsis [1] firstly proved that the intensity change of continuous intensity light after going though the tissue can be recorded for tissue optical properties characterization. The typical working principle of continues-wave (CW) mode diffuse optical imaging is shown in Fig. 3-11. A collimated beam of NIR light with intensity of I_i is incident on the tissue slab. The intensity of the emission is $I_o (I_o \leq I_i)$. The attenuation of the input intensity with respect to the output intensity of the NIR light is primarily caused by the presence of absorber and scatterer inside the tissue. Arridge has proven that the information of intensity change alone is not sufficient to distinguish between the changes between absorption and scatter [114]. To be able to resolve absorption properties, one has to assume that the scattering properties of the tissue are homogeneous throughout the tissue and estimate their average value. With this assumption, the intensity change can be dependent on the absorption only. Thus the absorption properties can be resolved accordingly.

For multiple pairs of light sources and detectors, the absorption coefficient of the tissue can be simultaneously derived from the measurement using the

spectroscopy-like detection setup. However, for multiple wavelengths, the assumptions that the scattering is constant will induce error to the absorption coefficients. Therefore the difficulty of the continuous wave optical approach should increase to non-linear mode if one wants to resolve the chrompohore concentrations.

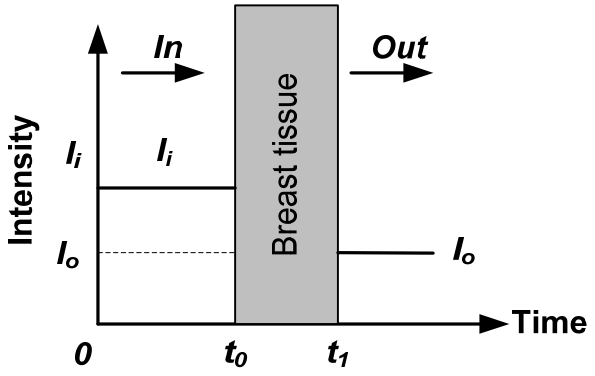

Fig. 3-11 Continuous-wave technique.

3.2.6.1.2 Instrumentations

The geometry of the light source and detector employed in the continuous wave optical approach determines the corresponding instruments, which can be spectroscopic systems (for single pair of light source and detector fiber) or CCD camera system (for multiple light source and detector fibers).

The advantages using fiber-coupled CCD camera are depended on the speed performance. Normally a CCD spectrometer can operate at frequency up to 100 Hz, which enables a possibility to realize high speed tomography imaging performance. The limitations of CW measurements are that the path length for photon travelling must be estimated and the scattering properties must be assumed. This estimation will cause errors in absorption resolution. Meanwhile, CW methods are also suitable for application including thick tissue since the attenuation measurements are subject to the signal-to-noise

ratio (SNR). Comparing to the frequency-domain method and the time-domain method, CW is not suitable for tomographic imaging applications as the measurements severely limit the resolving accuracy of tissue's optical properties [115].

3.2.6.1.3 CW systems at present

Currently, almost all CW imaging/fluorescence applications make use of NIR CCD cameras as detector to get a fast detection speed (multi channels in parallel) and a large detection area. Ulas [116, 117] employs the CCD camera to detect the intensity of the fluorescence around the tumor region to study the drug delivery effect. Barbour developed an 18 channels a CW system named IRIS-OPTI scanner [118]. Schmitz [119] proposed a CW method to record the breast cancer using high speed CCD camera. Researchers in Hitachi (Tokyo, Japan) developed a commercial product for topographic mapping of cortical activity [120].

3.2.6.2 Frequency-domain method

3.2.6.2.1 Principle

Fig. 3-12 illustrates the schematic of a typical frequency-domain (FD) optical imaging technique. In FD, intensity-modulation technique is used to modulate light source and the heterodyne technique is used to resolve the optical properties from the transmitted or reflected acquisitions. In practice a NIR laser diode (LD) is intensity-modulated (by modulating the working current)at one or few radio frequencies (RF). The RF frequencies are normally in few hundred MHz. The modulated light is guided to illuminate the tissue. The transmitted and/or the reflected signals, often known as the photon density

waves (PDW) are fiber-coupled into the photomultipliertubes (PMT), where the optoelectronic (O/E) conversions are down-converted into audio frequency signals by correlating with the reference signal. As a result, the modulation frequency-dependent light power (intensity) $M(f)$, phase shift $\phi(f)$ and the modulation depth of the detection signals relative to the input reference signals can be extracted.

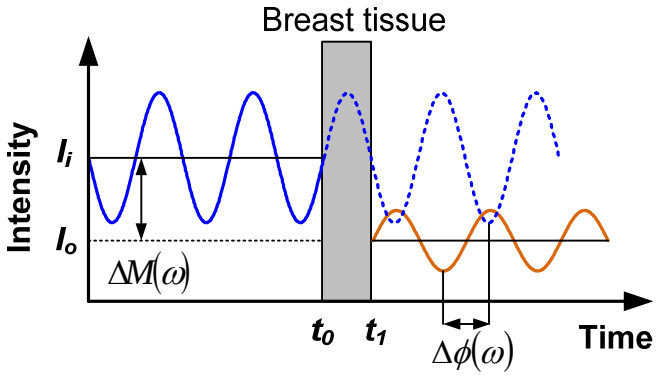

Fig. 3-12 Frequency-domain (frequency-modulate) techniques.

For example, the analytical expressions for the intensity modulation intensity $M(f)$ and the phase $\Delta\phi(f)$ derived by the Fourier transformation of Eq. (3-3) at modulation frequency f in an infinite boundary condition (Fig. 3-7), are defined by [88]

$$M(r,f)=\frac{\left(1+\psi_0^2+\psi i\right)^{1/2}}{\left(1+\psi_\infty\right)}\cdot\exp\left(\psi_\infty-\psi_i\right), \tag{3-14}$$

$$\phi(r,f)=\psi_r-\tan^{-1}\left(\frac{\psi_r}{1+\psi_r}\right), \tag{3-15}$$

where

$$\psi_0 = \sqrt{\frac{3[\mu_a + (1-g)\mu_S] \cdot (r^2 + Z_0^2) \cdot \sqrt{(\mu_a c)^2 + (2\pi f)^2}}{c}}, \tag{3-16}$$

$$\psi_r = -\psi_0 \sin\left(\frac{\theta}{2}\right), \tag{3-17}$$

$$\psi_i = \psi_0 \cos\left(\frac{\theta}{2}\right), \tag{3-18}$$

$$\theta_i = \tan^{-1}\left(\frac{2\pi f}{\mu_a c}\right), \tag{3-19}$$

$$\psi_\infty = \psi_\infty(f=0) = \psi_i(f=0) = \sqrt{\frac{3\mu_a[\mu_a + (1-g)\mu_S] \cdot (r^2 + Z_0^2)}{c}}, \tag{3-20}$$

For the fixed values of r and f, the absorption coefficient and scattering coefficients can be obtained by a multidimensional Newton-Raphson algorithm designed to solve Eqs. (3-13) and (3-14).

It has been proven that the scattering and the absorption of tissues have independent affects on both the intensity and phase shift measurements of the transmitted and/or the reflected signals [88, 121]. Therefore, the change of these signals can be used to separate the absorption and scattering information without *prior* knowledge of the path length, which makes FD approach different to the continuous wave approach. The standard technique of frequency-domain spectroscopy configurations and the imaging has been reviewed in literatures [88, 94, 121-123].

3.2.6.2.2 Instrumentations

Gao *et al.* have proven that the sensitivity to absorption and scattering (for spectroscopy), and the spatial resolution of the FD imaging systems are

dependent on the frequency chosen [124]. Theoretically, the more spread frequency spectra were utilized in the FD system, the higher accuracy the TPSF can be achieved. But in practice, the laser diode (LD) cannot be modulated by arbitrarily high frequencies due to the limitations of the LD construction (primarily due to the bandwidth limitation associated with the conjunction capacitance). Thus in most cases, the RF frequencies used range from tens to few hundred MHz (typically from 50 MHz up to 250 MHz). This RF range equivalently corresponds to a few nanoseconds in the time-domain technique. For actual instrumentations, two modulation schemes are widely used. The system either uses a single LD which is modulated by multi frequencies, or uses multiple LDs, which are modulated in a single frequency. Comparing with the later one, the former scheme offers system advantages like low cost and compactness. However, the system architecture is normally complex. For a few specific RF frequencies, the data acquisition time by using single LD will significantly increase, which consequently reduces the superiority of the FD technique.

3.2.6.2.3 FD systems at present

The first frequency-domain measurement of photon migration in tissues was reported by Lakowicz and Berndt in 1990 [125]. After that, the effectiveness of frequency domain systems for tissue imaging have been demonstrated by different research groups [71, 121, 125-129], including the first *in-vivo* images [121, 130, 131]. Apart from academia, some industrial companies have involved in this promising field. Several breast imaging prototype systems based on FD measurements have been built by Carl Zeiss ,[132] Siemens [133] and Philips [134]

companies, respectively. The preliminary clinical trials have already been conducted using prototypes at each company.

3.2.6.3 Time-domain (TD) method

3.2.6.3.1 Principle

Fig. 3-13 illustrates a typical time-domain diffuse optical imaging technique, which can be used for time-resolve spectroscopy of imaging applications. An ultrashort pulse laser (typically from few femtoseconds up to a few nanoseconds in pulse width) is used to illuminate the tissue. The photon will become spatially and temporally dispersed with time after transmitting through or reflecting back from the tissue. A histogram of the time-of-flight of individual photons, or so-called the temporal point spread function (TPSF), can then be accumulated. As the ultrashort pulse light is essentially constituted by ultra broad band frequency spectrum information, so the retrieved TPSF contain very broad spectra information. This feature theoretically makes TD superior over the CW technique, in which only DC signal is investigated and the FD technique, in which a limited few RF signals are investigated. In addition, extra information can be extracted from the TPSF measurements. For example, the integrated intensity of the TPSF is the same as a continuous wave measurement. The amplitude and the temporal shifting of the TSPF can be used to retrieve the optical properties of the tissue. The full theory of the time-domain optical measurement has been investigated in a couple of literatures [12, 68, 104, 106, 135].

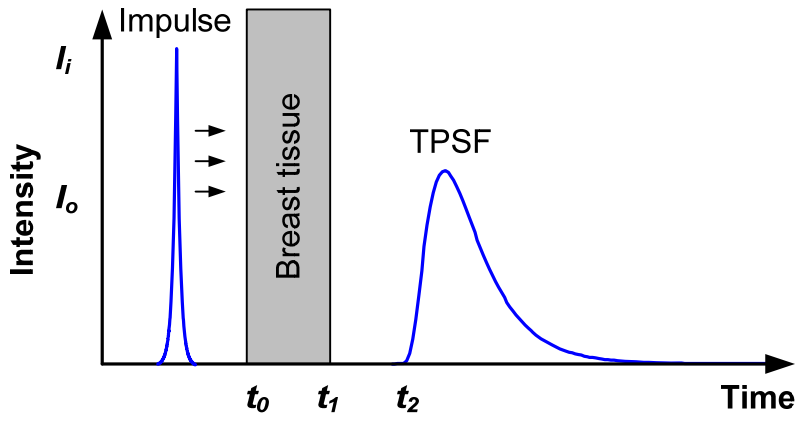

Fig. 3-13 Time-domain diffuse optical technique.

3.2.6.3.2 Instruments

The time-resolved spectroscopy and tomography imaging are intensively explored for breast examination. The ultrashort pulse laser (from CO_2, He-Ne Lasers and so on) is multiplexed into multiple fibers channels using optical switch/router. These fibers are attached on the tissue in a specific spatial layout in order to get maximal independent optical information. Meanwhile, to measure the TPSFs from the transmission and the reflectance, time-correlated single photon counting (TCSPC) [23, 67, 69, 71, 74, 136-140] and streak camera [133, 141-143], are the widely used for optical signal detection.

3.2.6.3.2.1 Streak camera

Streak camera can record full TPSFs. Fig. 3-14 shows the working principle of streak camera. The diffused photons escaping from the breast tissue enter the streak camera through a slit, after that the photons are converted into electrons, which is proportionally to the sensitivity of the photocathode. The photonelectrons are accelerated by the following high electric field and go through a deflection tube. An external temporal sweeping voltage deflects the direction of these electrons in vertical direction. The deflected electron hit the

phosphor screen. Then the time-resolved intensity can be acquired using a high speed CCD camera.

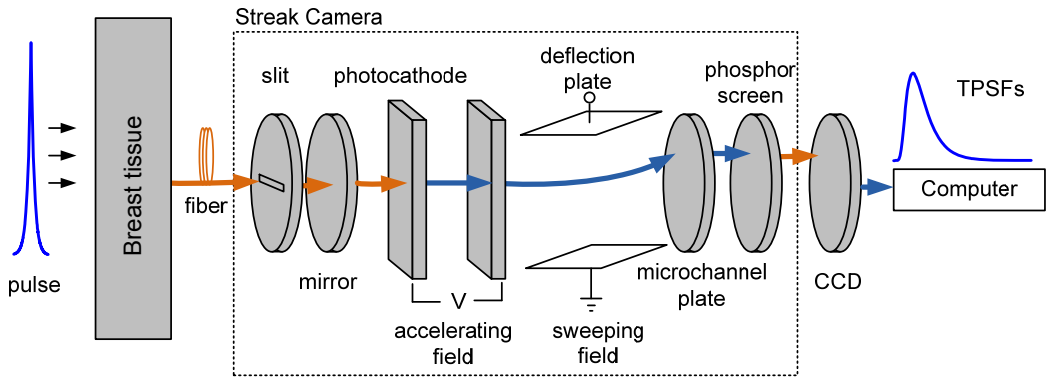

Fig. 3-14 TPSF acquisition using streak camera.

Since the arriving time of each photon to the slit is depended on the absorption and scattering properties of the tissue, then the accumulation of the streak intensity on the phosphor screen over time results in the TPSF measurement accordingly. Illuminating the photocathode directly by the ultrashort pulsed laser can create a reference pulse on the phosphor screen, from which the absolute time of flight can be calibrated.

The TPSF acquisition using streak camera setup gives the time-resolved systems advantages including excellent temporal resolution (normally down to a few picoseconds) and fast data acquisition. However, the disadvantage is about the high system cost. The detection area is subject to the aperture size of camera, which is normally in a small size (normally < 1 mm^2). In addition, the dynamic range of streak camera is normally limited (approximately 10^4). Finally, the temporal nonlinearity is inherently subject to the ramp voltage. For these reasons the streak camera method has limited applications for diffuse optical imaging.

3.2.6.3.2.2 Time-correlated single photon counting

Time-correlated single photon counting (TCSPC) is based on the detection of single photons of a periodical light signal. Fig. 3-15 shows the detection time of each individual photon and the waveform accumulation from individual time measurements. This method makes use of a straightforward fact: the light intensity signals of high repetitions rate is usually so low that the probability of detecting one photon in one signal periods is much less than one. Therefore, the detection possibility of several photons can be neglected.

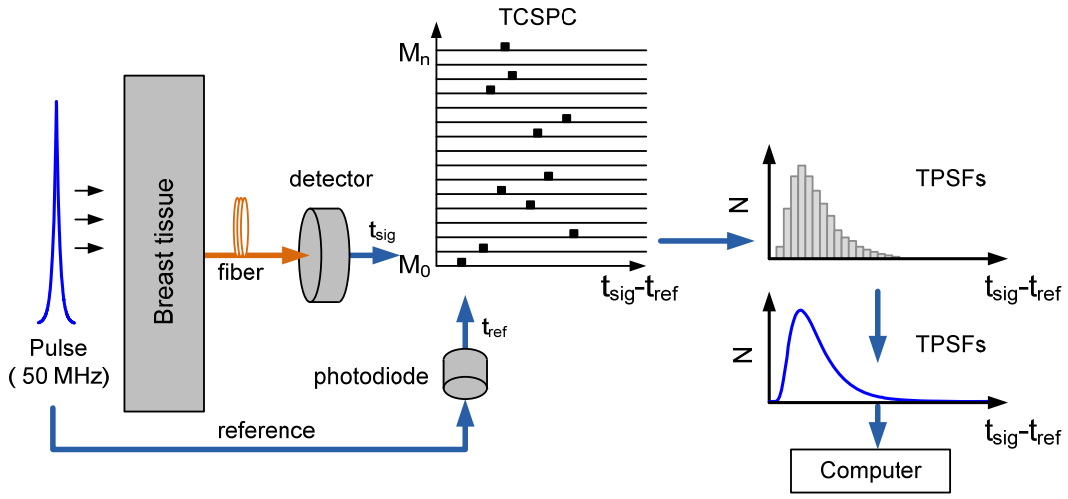

Fig. 3-15 TPSF measuring using TCSPC techniques.

In the time-domain TPSF measurement, a periodical short pulse laser with high repetition rate is used to illuminate the tissue. Each pulse will disperse with time after transmitting though or reflecting from the tissue. Each of this dispersed pulse will be coupled into the fast detector such as a time-to-amplitude (TAC) converter. Although each pulse consists of a large amount of photons, only one photon can be detected by the TCSPC at each measurement ($M_i, i = 0 \ldots n$). The timing of each detected photon is specified by the reference photon. It is should be noted the possibility to detect more than one

photon at each detection time is very rare and the possibility of detecting nothing does exist. After many photons and a period detection time, the randomly detected photons and the corresponding timing pulse stored in the system memory can be accumulated into the TPSF.

The TCSPC-based signal acquisition techniques have been widely applied in ultra fast recording of optical waveforms, fluorescence lifetime measurements, fluorescence lifetime imaging and optical tomography. The advantages of TCSPC-based system are of high dynamic range and excellent temporal linearity. If combining with the micro-channel plate (MCP) PMT, the system additionally offers a desired goodness on large detection areas. The low cost replacement to MCP-PMT is to use high speed avalanche photodiode (APD) [144]. However, such a replacement is limited by a smaller dynamic range.

The disadvantage of TCSPC system is lower temporal resolution (typically in a range of tens to hundreds of picoseconds). TCSPC devices' high optical sensitivity requires an extreme dark environment for TPSF acquisition. This will cause discomfort to patients in clinical application. To detect the TPSF with sufficient signal-to-noise ratio, the data acquisition time usually extends to tens of minutes or longer due to the slow photon accounting rate (usually from 10^4 up to 10^6 per second). The data acquisition will be significantly extended if multiple light sources and detectors are employed. This system limitation also limits its applicability for those clinical applications, in which fast data acquisition performance is crucial.

3.2.6.3.3 TD systems at present

With the development of ultrafast laser technique and NIR semiconductor detection devices, the time-domain optical imaging system got profound advances.

In Japan, Oda *et al* reported an advanced 64-channel TCSPC system using the TAC for time-resolved function [145]. Also in Japan, Prof. Yamada's group reported a 16-channel time-resolved DOT system using TCSPC devices for anatomic imaging [69, 124, 146-148].

In US, Prof. Chance's group reported an 8-channel time-resolved TCSPC NIR spectroscopy instrument for motor cortex activity monitoring and the tomographic breast phantom studies [26, 121, 149-152]. In UC Irvine, Prof. Tromberg's group constructed a time-resolved NIR spectroscopy for benign and malignant breast tissue characterization [23, 153-156].

In UK, UCL has built a 32 channels time-resolved DOT, named MONSTIR using TCSPC-based devices [70, 74, 157, 158] and streak camera devices [136]. The research focuses on human breast tissue and neonatal brain hemodynamic study.

3.2.7 Comparison between optical techniques

As a summarization, Table 3-4 compares pros and cons of the above three main diffuse optical imaging techniques.

Table 3-4 Pros and Cons of CW, FD and TD techniques for DOT/DOS

	Advantage	Disadvantages
CW	• Low cost; • High speed; • Simple architecture;	• Low detection depth; • Less information; • Susceptibility to SNR;
FD	• Relatively low cost; • Fast system response; • High speed; • Relative simple architecture;	• Lower temporal resolution (< 1 GHz or equally a few nanoseconds);
TD	• High temporal resolution; • Large detection area; • High dynamic range;	• High system cost; • Susceptible to environmental noise;

Chapter 4. Design and implementation of novel fast time-domain diffuse optical tomography

This chapter systematically describes the design and implementation of a novel fast time-domain diffuse optical system, which is advantageous on fast spectroscopic and tomographic imaging performance for breast tissue characterization *in vivo*.

The first part describes the working principle. Emphasis is placed on spread spectrum correlation technique using high-speed pseudorandom bit sequence and its potential to acquire time-resolved data in a fast speed. The second part technically describes the details of the implementation. All of key modules and functionalities which affect system performance are discussed separately. The last part shows the system performance assessment.

4.1 Principle

4.1.1 Correlation of spread spectrum signals

It is well known that a spread spectrum system possesses many desirable properties, such as selective addressing capability, low error rate, and interference rejection which make it extremely useful in communication industry. Taking the pseudorandom bit sequence (PRBS) as an example, the PRBS code has only a weak cross-correlation with other codes, while the autocorrelation function shows a delta-function-like function. Therefore, a receiving system can pick up the correct code sequence, differentiate it from environmental noise and interference, and is able to distinguish the same

sequence that arrives at different times from multiple paths. These properties are utilized in our time-resolved optical system, in which photons detected at different time delays can be resolved. Higher signal-to-noise ratio, shorter data acquisition time, and low system cost are the expected advantages of our new diffuse optical tomography system by using the PRBS modulation technique [159].

We denote $I(t)$ as the time-dependent response of a sample to the excitation of an ultrashort pulse. A light source continuously modulated with a pseudorandom bit sequence is used to illuminate the sample. So the ac component in the detected signal is proportional to a convolution of the impulse response and the excitation:

$$R(t) = A \cdot I(t) \cdot P(t) \tag{4-1}$$

where A is the modulation depth, $P(t)$ is a maximal length sequence, which has a circular autocorrelation function similar to a delta function:

$$g(\tau) = \langle p(t)p(t-\tau)\rangle = \begin{cases} 1 & \tau/T_0 = 0; \\ -\dfrac{1}{N} & \tau/T_0 = \pm 1, \pm 2, \ldots \pm \dfrac{N}{2}. \end{cases} \tag{4-2}$$

where τ is the time delay, T_0 is the period of one-bit. $g(\tau)$ is a delta-shape function when τ is in region $[-T_0, T_0]$. In regions out of $[-T_0, T_0]$, the autocorrelation approximate to zero when N is big enough. Correlating $R(t)$ with $P(t)$ yields

$$f(\tau) = \langle R(t)P(t-\tau)\rangle = I(\tau) \otimes g(\tau) \tag{4-3}$$

Eq. (4.3) is valid when the time span of TPSF is less than NT_0. If T_0 is small enough, $f(\tau)$ at a specific delay time τ is well approximated by $I(\tau)$. When

T_0 becomes comparable to the time scale of $I(\tau)$, $g(\tau)$ acts as an equivalent temporal gating window. So the impulse response or its integral over a time window can be retrieved by the correlation method.

4.1.2 Simulation

Fig. 4-1 shows a typical non-return-to-zero (NRZ) PRBS signal at a bit rate of 2.488-Gb/s (OC-48) and pattern length of 2^9-1 = 511 bits. Each pattern has period of 205.38 ns.

Fig. 4-2 shows the simulation results (with normalization) of the autocorrelation of the PRBS with a data bit rate of 2.488 Gbps and pattern length of 511 bits. The repetition rate of autocorrelation is exactly equal to the pattern length, i.e. 205.38 ns.

A zoom-in view of each autocorrelation (rectangle area in Fig. 4-2) is shown in Fig. 4-3. The delta-shape function has theoretical full width at half maximum (FWHM) of 401.929 ps, which equals to two folders of the reciprocal of the data bit rate of the PRBS signal.

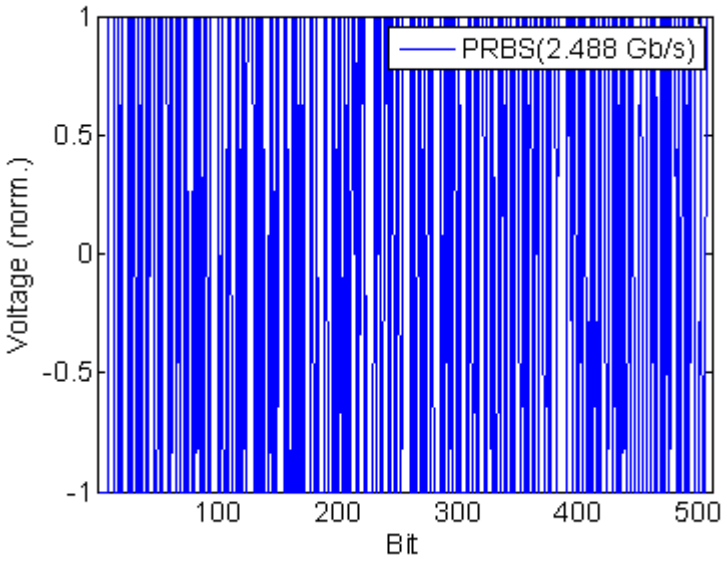

Fig. 4-1 Pattern of a NRZ 511-bit, 2.488-Gbps PRBS.

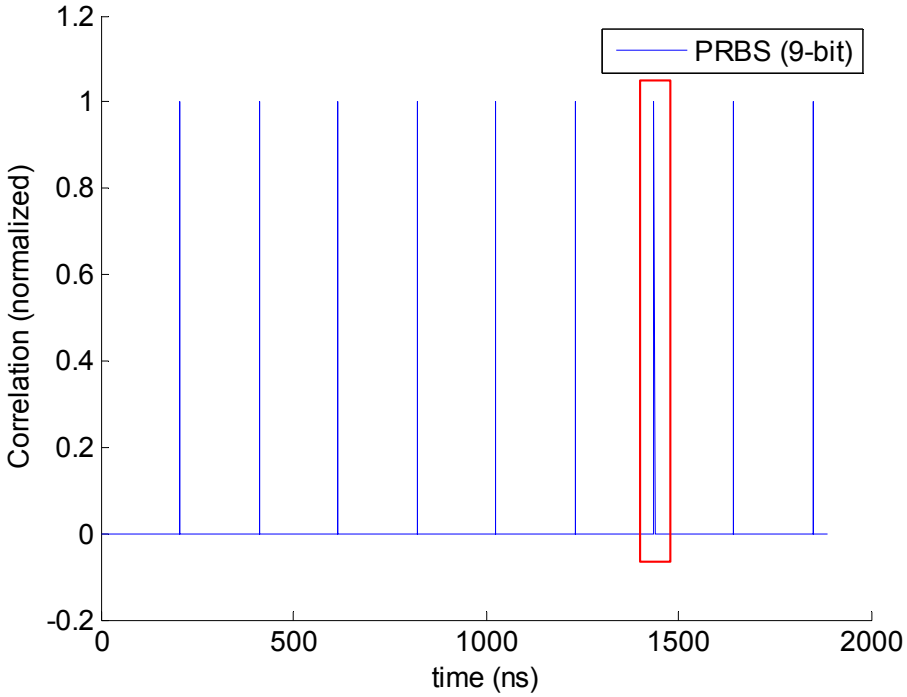

Fig. 4-2 Autocorrelation of 511-bit, 2.488-Gbps PRBS signals (NRZ).

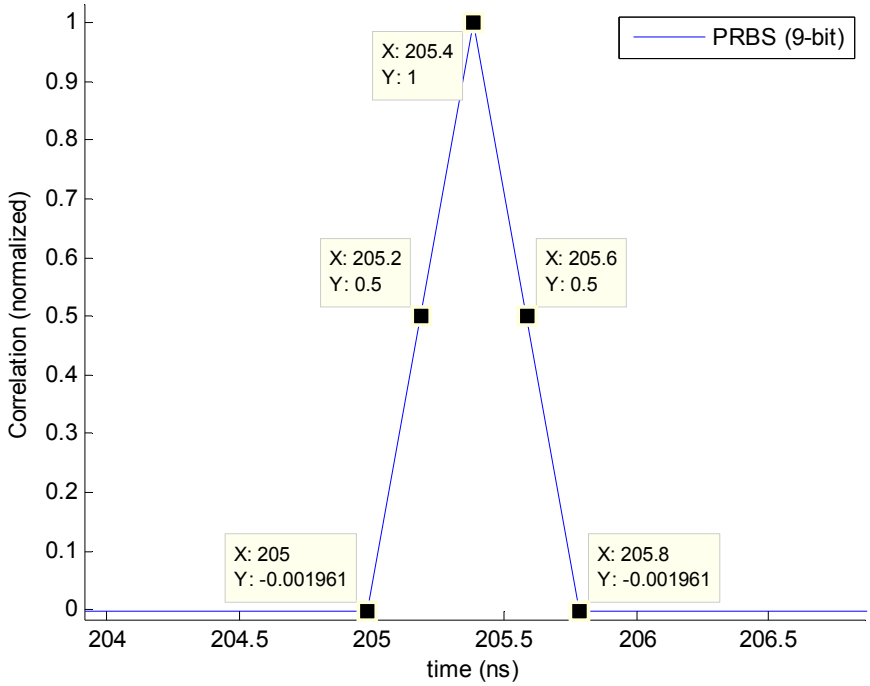

Fig. 4-3 Autocorrelation of 2.488-Gbps PRBS (zoom-in view of Fig. 4-2).

4.2 System Design and Implementation

4.2.1 General objectives

This research firstly aims to develop and construct a high quality time-domain DOT/DOS system by utilizing the above spread spectra correlation technique. The following objectives highlight the most important features of the system, which will guide the whole research.

- The whole system is a fully simplex. The prototype system contains 9 light source fibers and 4 detection channels (totally 36 source-detector pairs) for TPSF acquisition. The system should be fully automatically controlled by computer via software (LabVIEW^{TM} and Matlab^{TM}) and hardware interfaces (data acquisition card) in a friendly user control GUI (graphic user interface).
- In order to improve the data accuracy against to the environment changes, the temperature whole system should be kept stable within a sufficiently long duration (> 1 hour).
- The temporal resolution is a very important system specification. Theoretically it can reach 401.929 ps. However, due to the limited bandwidths of the optical devices (such as laser diodes and photodetectors) and RF components, the real time-resolution is usually worse than the theoretical value. But we choose components carefully to achieve the highest possible time-resolution. .
- The crosstalk between source and detection channels should be negligible comparing with the TPSF intensities acquired. The effect of environmental illuminations should be negligible, too. The maximum dynamic ranges of TPSF signal acquisition should be around 10^4.

- At least two NIR wavelengths should be employed to quantify the concentration changes of Hb and HbO. Super stable laser diodes (LD) will provide stable light sources.
- A hand-held probe in reflectance mode is designed to mount all fiber and bundles. Balance between number of sources and detectors and the data acquisition speed should be optimized. High data acquisition speed is desired. Nearly real-time imaging performance is expected.
- The computation time for imaging reconstruction should be much faster than data acquisition.
- There is a research budget $120k for prototype system development, supporting equipment purchasing and *in vivo* experiments. The total cost of prototype system should be less than $ 70k. The prototype system should be compact, robust and lightweight.

4.2.2 System overview

Fig. 4-4 shows the schematic diagram of fast TD-DOT prototype system developed in this research [160]. A PRBS function generator continuously generates a train of 2.488-Gbps signals. The pattern length is 511-bit. This PRBS signal is spitted into two even arms by a power splitter. One arm is used to modulate the NIR light. The other arm is used as reference to decode the optical signals emitted from tissue. Laser beams from two low-cost LD ($\lambda_1 = 785$ nm and $\lambda_2 = 808$ nm) have optical powers of 5 mW. Two NIR light beams are coupled into a single mode fiber then go through an external Mach-Zehnder intensity modulator. In modulator, their intensities are respectively modulated by the PRBS modulating signals. After modulator, the encoded

light beams are fiber-coupled to a Y-shape tap coupler. A minor portion (~2%) of the optical power is tapped out for intensity stability monitoring. The major portion (~98%) of the optical power is guided to a 1 × 9 fiber optical switch. The switch sequentially multiplexes the laser beam into 9 output fibers. A hand-held probe mounts 9 fiber and together with another 4 fiber bundles. The probe is placed on the top surface of tissue-like phantom or breast tissue. The reflectance optical signals from the phantom/tissue are collected by fiber bundles and guided to 4 avalanche photodiodes (APD). After O/E conversion, the signals are pre-amplified by lower noise amplifiers before being fed into 4 mixers through the radio frequency (RF) port. Meanwhile the reference PRBS signals feeding into the local oscillation port (LO) after appropriate sequential time delay are used as reference for demodulation. The down-conversion signals, i.e. the TPSFs are amplified by operational amplifiers (OP-AMP). Computer gets these TPSF signals from data acquisition card (DAQ). The tomographic images or the spectroscopic information are reconstructed and analyzed, and the optical properties, including absorption coefficient, reduced scattering coefficient, and the physiological information, including the oxygenation saturation and the total haemoglobin concentration are extracted and mapped.

Fig. 4-5 shows the picture of fast time-domain DOT/DOS prototype system. Details of each module are described in the following parts.

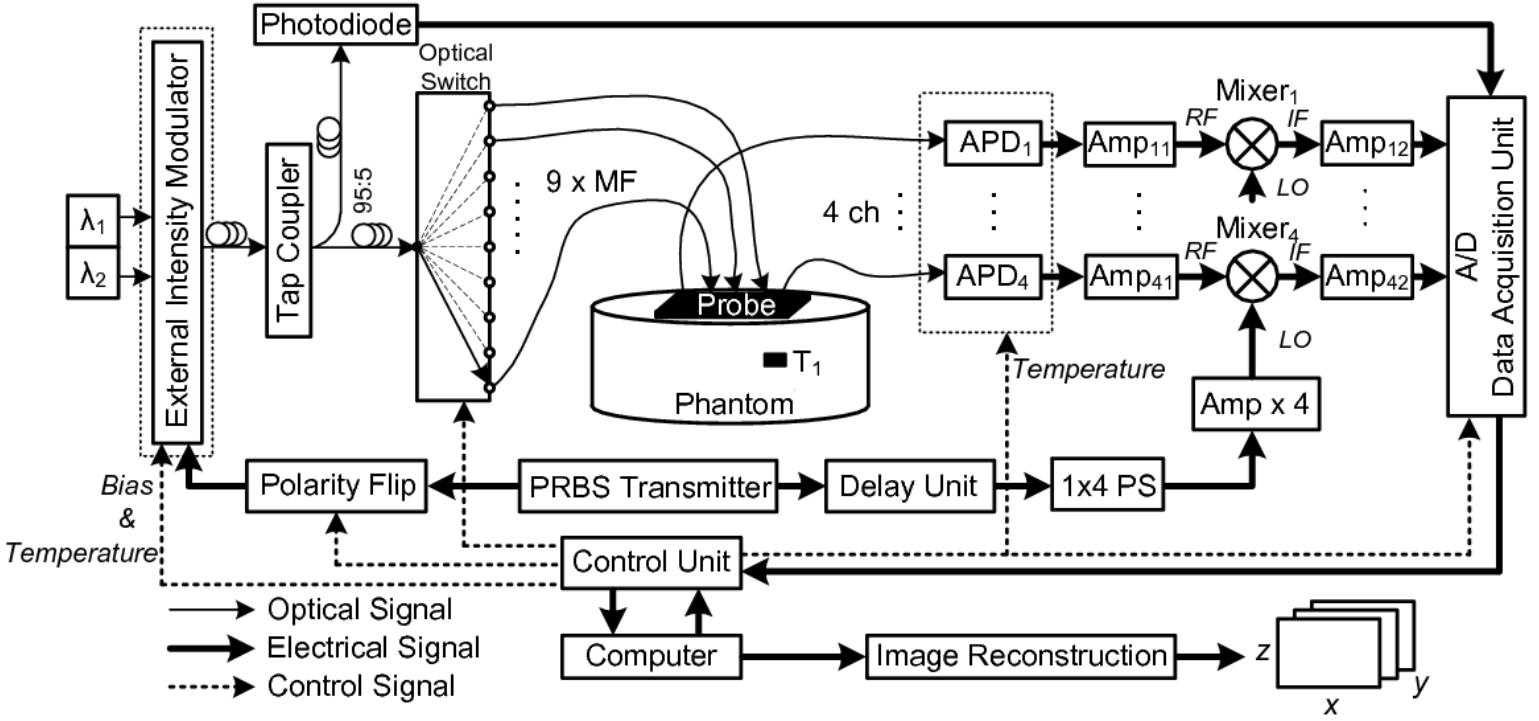

Fig. 4-4 Schematic of novel TD-DOT prototype system.

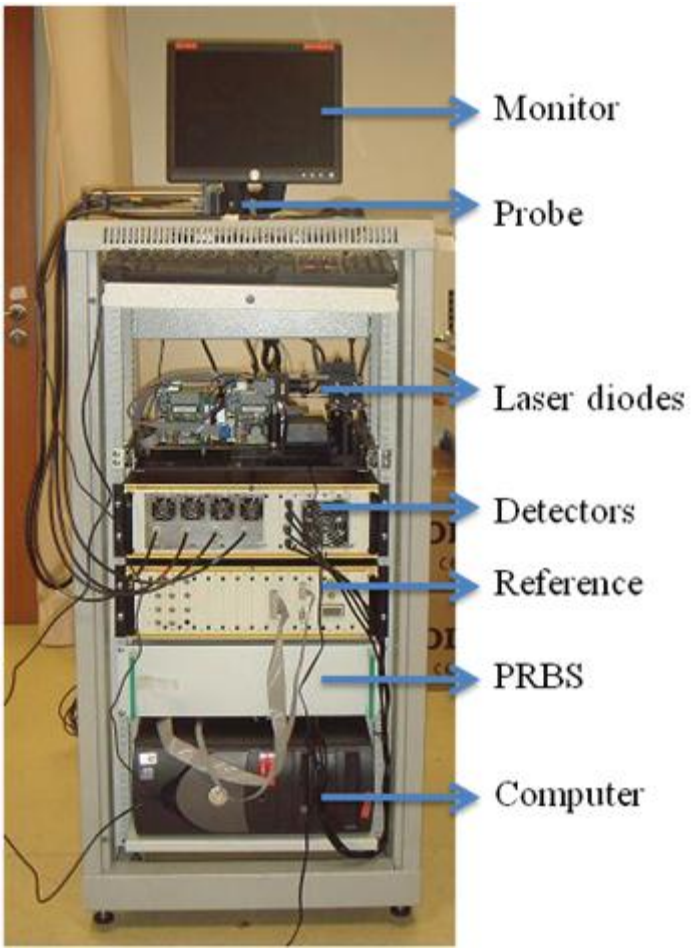

Fig. 4-5 DOT/DOS prototype system on a 19-inch rack (front view).

4.2.3 Optical modules

The optical modules play key roles in the whole system. Research was focused on the stabilization of modulation depth, optical power modulation, and temporal delay between optical modules.***Laser sources***

Two laser source schemes are available and tested, respectively. Scheme one will use a wavelength-tunable stable laser diode (DL 100, TOPTICA, US). Scheme two will use two NIR laser diodes (780 nm and 808 nm). Scheme one is reserved for spectroscopy application in future. The laser diode is constructed in the prototype system for image/spectroscopy study at present.

4.2.3.1.1 Wavelength -tunable stable grating laser diode

The tunable wavelength LD is purchased from TOPTICA [161]. During system calibration, one single wavelength (at 785 nm) is picked up by default. The laser diode driver provides excellent temperature stability as well as a fast warming up speed. The output optical power can be accurately and easily changed using current controller and monitor on the instrument panel. The limitation of this wavelength tunable laser diode system is its slow wavelength tuning speed, which would increase the data acquisition time in the spectroscopy applications. Table 4-1 summarizes main specifications of the wavelength-tunable LD scheme.

Table 4-1 Specs of the wavelength-tunable laser diode

Model	DL series
Mode	SM
Tunable Wavelength (nm)	632-1700
Modulation (mode-hop free range) (GHz)	> 20
Wavelength (nm)	785 ± 3
Power Settings (mW)	~20 mW
Power Max (mW)	50 mW
Driver	DCC110; DTC110; DC110; SC110;
Manufacturer	TOPTICA PHOTONICS

4.2.3.1.2 NIR laser diodes

The dual NIR wavelengths can be got from two dedicated laser diodes (LD). These two LDs are employed in the spectroscopy system to resolve the concentrations of HbO and Hb. During system calibration and tomographic image reconstruction, lasers at 785 nm or 808 nm were selected sequentially. The optical power from two LDs is monitored using power meter (NEWPORT). Table 4-2 summarizes the specifications and the configurations

of two wavelength-fixed LDs. Fig. 4-6 shows the setup picture of dual wavelength LDs in the system. In the following part, the description is focused on the applications using two independent NIR LDs.

Table 4-2 Two wavelength-fixed NIR LDs in the DOT/DOS system

	λ_1	λ_2
Model	DL-7140-201S	DL-8141-035
Mode	SM	SM
Driver	ITC102	ITC102
Wavelength (*nm*)	785 ± 3	808 ± 10
Average power (*mW*)	~ 20	~20
Max power (*mW*)	70	150
Beam Divergence Perpendicular (^{o})	17 ± 3	16 ± 4
Beam Divergence Parallel (^{o})	8 ± 2	8 ± 2
Off Axis Angle Perpendicular (^{o})	0 ± 3	0 ± 3
Off Axis Angle Parallel (^{o})	0 ± 2	0 ± 3
Manufacturer	SANYO	SANYO

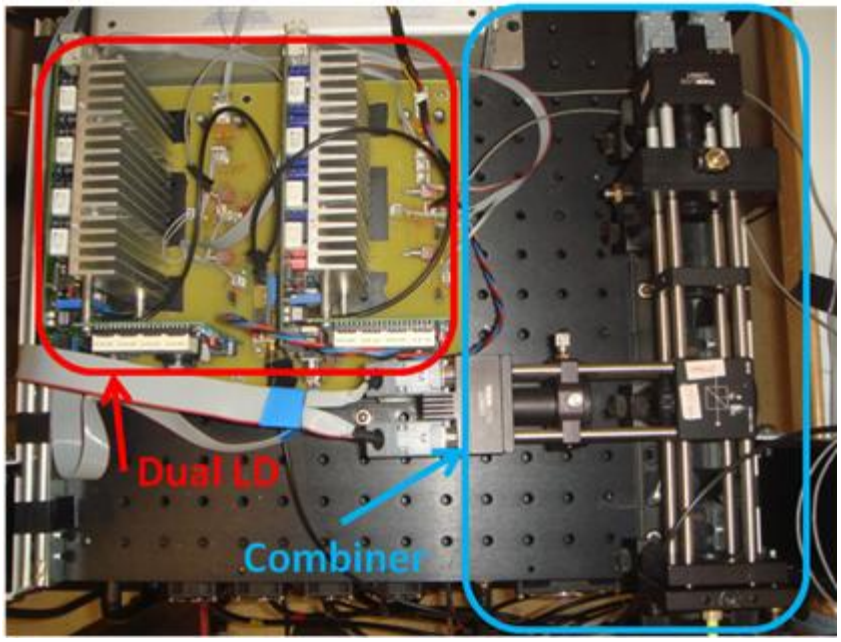

Fig. 4-6 Photograph of the dual-wavelength light sources and the combiner on a 19'' optical rack.

4.2.3.2 Fibers

There are three types of fibers are utilized in the system: the SM/PM FC fibers, the multimode (MM) fibers and the quartz fiber optical light guide (fiber bundles). The SM/PM FC fiber conducts the constant optical power NIR laser from the LD into the intensity modulator. Nine MM fibers were used as light source fibers to conduct the PRBS-modulated optical signal from optical fiber switch to the hand-held probe (see Fig. 4-4). In order to mount 9 fibers in the hand-held probe, the fiber cladding were taken away. The optical light guides who were mounted on the hand-held probe together with the MM fiber serve as the detection channels. They are used to collect the reflective optical signal emitting from phantom/tissue and transmit the optical signals to the APD array (see Fig. 4-4).

Table 4-3 Specification of optical fibers used in the prototype system

Model	F-PM630-C-2FC	SF13048M-001	NT38-955
Description	Fiber	Bare fiber	Light guide
Wavelength (*nm*)	630	780	780
Mode	SM	MM	MM
PM	Yes	No	No
Core size (*mm*)	0.01	0.05	3.175
Cladding size (*mm*)	0.400	0.125	-
N.A	0.11	0.11	0.17
Distributors	Newport	Photoniks	EO Edmund

4.2.3.3 Modulator

In our system, the constant intensity laser beams need to be intensity modulated by the 2.488 Gb/s PRBS signal. This can be realized by using an external intensity modulator. There are two types of modulators available for high speed analog modulation: Electroabsorption modulator (EAM) and

interferometric modulator (generally the Mach-Zehnder intensity modulator, MZM). Comparing with EAMs, the MZMs generally offer the maximum power handling capability, the minimum optical loss, the maximum modulation depth and the cost-effectiveness. Because of these highly desirable features, our system would adopt MZM to realize the PRBS modulation for the NIR beams. The drawback of the MZM also deserves careful handling. The inherent modulation instability will induce an undesired bias drifting effect. So it is necessary to introduce an external bias controller to dynamically stabilize the modulation depth of the MZM (see section 4.2.4.8 for modulation stabilization).

The MZM deployed in our system is 2-port, *Z*-cut titanium-indiffused lithium neobate (Ti:$LiNbO_3$) interferometric MZM (Fig. 4-7), which is commercially available from EOSPACE, US [162]. This kind of MZM product provides a stable analog modulation speed at 10 Gb/s and a sufficient bandwidth (>10 GHz), which fully satisfy the requirements at 2.488 Gb/s analog modulation. The RF port is connected to the 2.488-Gbps PRBS signal for modulation. The DC port is connected to bias voltage to keep the working point biased at the desired positive quadrature point. Table 4-4 summarizes the main specifications and configurations of the MZM in our system.

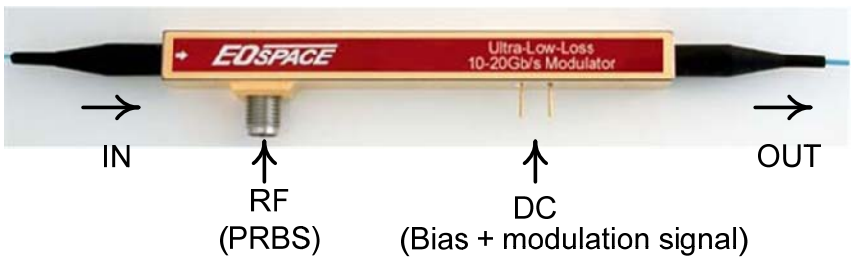

Fig. 4-7 Interferometric Mach-Zehnder intensity modulator.

Table 4-4 Specifications of the MZM

Wavelength (*nm*)	780
Modulation speed	10 Gb/s
Bandwidth	>10 GHz
Input fiber mode	PM
Output fiber	SM and PM
Bandwidth (*GHz*)	> 10
Optical insertion loss (*dB*)	3.7
RF port: V_π @ 1GHz (*V*)	1.7
Bias V_π	1.7
Extinction ratio (*dB*)	21
Crystal cut/materials	*Z*-cut LiNbO3
Model	AZ-0K1-10-PFU-SFU-780-S
Manufacturer	EOSPACE, US

4.2.3.4 Fiber optic switch

The fiber optical switch sequentially deliveries the PRBS-modulated laser beam from the MZM into 9 independent source fibers. It is a fast and compact component from PHOTONIK Company [163]. The optical multiplexing is TTL programmable by computer through a 9-pin D-shape connector. Two laser beams 785 nm and 808 nm are alternately coupled into a 1 × 9 fiber optics switch. Table 4-5 summarizes of the primary specifications of the fiber optics switch.

Table 4-5 Specifications of the fiber optics switch

Wavelength (nm)	850
Insertion loss (dB)	< 1.0
Return loss (dB)	SM: > 55; MM: > 25
Cross talk (dB)	< -60
Switching time (ms)	< 10
Vendor	PHOTONIK Singapore

4.2.4 Electrical modules

This part describes the main electrical modules; including the PRBS signal generation, transmission, correlation and performance control. All of the electrical modules are encased in the three drawers as shown in Fig. 4-5.

4.2.4.1 PRBS generators

Currently we adopt two available approaches to obtain the 2.488-Gbps NRZ PRBS signal in our system. One approach is to use the field programmable gate array (FPGA). The other approach is to use transceiver.

4.2.4.1.1 FPGA approach

FPGA developing board is purchased from commercially available products (model VIRTEX-II PRO from Xilinx Company) [164]. The chips are programmable instructed using a logic circuit diagram in combination with a source code of hardware description language (HDL). The chips can be configured to realize any logical function as same as what an application-specific integrated circuit (ASIC) can perform.

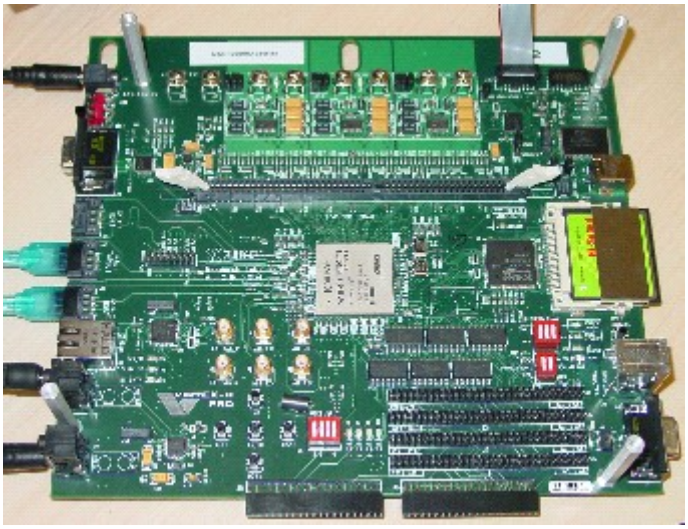

Fig. 4-8 PRBS generation using FPGA developing board.

The 2.488-Gbps PRBS generation using FPGA can be realized using the M-sequence algorithm. Fig. 4-8 shows the FPGA developing board.

4.2.4.1.2 Transceiver approach

The PRBS generation using FPGA developing board offers system versatility for pattern configuration. However, normally middle/high-end FPGA developing board is usually high cost (approximately 3,000 US dollars). The board size (25 cm × 25 cm) is large which is not desired for low cost and portable applications. Therefore it is necessary to substitute it with an economical alternative.

We designed and realized a low cost PRBS solution by using gigabit transceivers. The affiliated on-board PRBS serializer verification function is utilized for PRBS generation. Fig. 4-9 shows the photograph of a home-made transceiver-based PRBS generator. The board size is only 6 cm × 4 cm. The cost is significantly reduced from few thousand US dollars to about one hundred dollars. Appendix A.3 shows the circuit design, PCB fabrication and the program of this PRBS generator.

In this solution, the core chip is TLK2511 (Texas Instruments, US). The clocking module is picked up from programmable 1-PLL voltage control crystal oscillator synthesizer (CDCE913, Texas Instrument, US) [165]. The on-board bus clock is configured in LabVIEW™ program “CLOCK PRO” via USB port.

Fig. 4-9 PRBS generator using transceiver.

4.2.4.2 Avalanche photodiode (APD)

4 avalanche photodiodes (APD) are used to convert the optical reflectance emitted from the tissue into the electrical signal. Each of 4 APD detection channels is cascaded with a 50 Ω high-frequency resistors. The APD components (model: S2383-20) are available from company HAMMATSU, Japan [166]. They are in small size (TO-18 package, Fig. 4-10) and high quantum efficiency. Table 4-6 summarizes the configuration and settings of the APD used in the system.

Table 4-6 Specifications of the APD for O/E conversion

Bias voltage (*V*)	127 - 131
Detection area (mm^2)	0.78
Bandwidth (*MHz*)	600
Sensitivity range (*A/W*)	0.5
Spectral response (*nm*)	400-1000
Peak wavelength (*nm*)	800
Terminal capacitance (*pF*)	6
Gain (at 800 nm)	100
Temperature coefficient of Vbias (*V/deg.C*)	0.65
Model	S2383
Manufacturer	HAMAMATSU

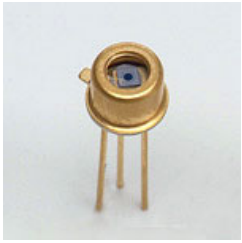

Fig. 4-10 High speed APD for O/E conversion.

4.2.4.3 Mixer for demodulation

The O/E conversion signals are amplified by two stages of *RF* amplifiers (model: ERA-3, Mini-Circuits Company, US). The amplified signals are fed into the RF port of mixer as shown in Fig. 4-11. The implementation of one detection channel is shown in Fig. 4-12. The LO port of the mixer is connected to the PRBS reference. Two PRBS signals are cross-correlated (by multiplying) in the mixer and the intermodulation results from IF port are down-converted by using a low pass filter (LPF). The low frequency signal is capacitively coupled to the DAQ. The PRBS-demodulation results, i.e. the TPSF of the tissue can be recorded using a specified sampling rate. Appendix A.2 shows the circuit design, PCB layout of the APD, amplifiers and the multiply mixers.

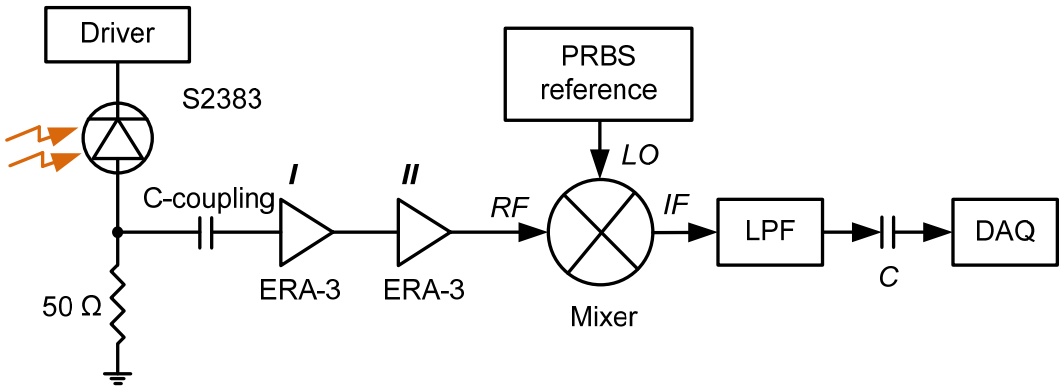

Fig. 4-11 Schematic of PRBS optical demodulator (one channel).

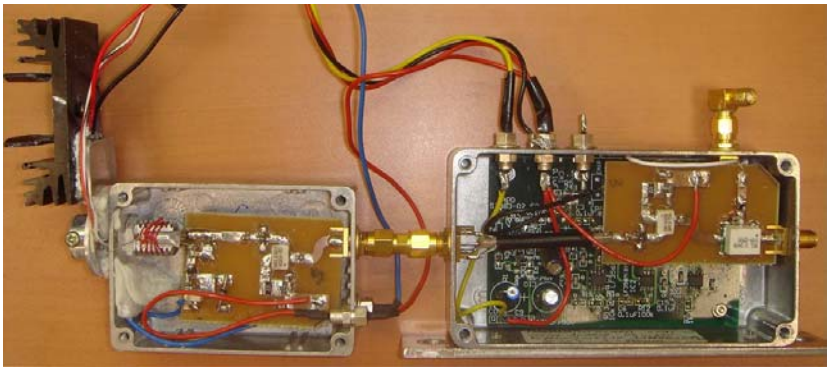

Fig. 4-12 Photograph of the PRBS demodulator.

4.2.4.4 Temporal delay

In order to get a temporal sampling as fine as 40 ps in TPSF acquisitions, the reference PRBS is sequentially delayed in steps of 40 ps. This task is realized by using a programmable optical delay line.

The PDDL5, GigaBaudics, US [167] used in the prototype system has an accurate digital control through a 25-pin TTL port. The minimum temporal delay step is 20 ps per LSB. The total temporal delay can be configured from 0 picoseconds up to 10230 ps. Table 4-7 summarizes the main specifications and configurations of the programmable optical delay line.

Table 4-7 Specifications of the programmable optical delay line

Signal rate (*Gbps*)	0 - 5
Minimum step size (*ps*)	20
Accuracy	± 1 LSB
Input mode	ECL
Output mode	ECL
Jitter (*ps*)	< 10
Model	PDDL5
Manufacturer	GigaBaudics, US

4.2.4.5 RF modules

In the spread-spectra correlation, a 2.488-Gbps PRBS is used for NIR light modulation. For such a high frequency signal, it is very important to maintain the signal integrity during transmission between any two consecutive lumped RF components. There are couples of RF components that are interconnected in order to maintain the signal integrity and relay the RF power, including RF synthesizer, RF amplifiers, bias tee, RF choke, RF attenuator and ECL-TTL converter. These components are distributed and connected into two PRBS transmission braches (see Fig. 4-11 and Fig. 4-12). Table 4-8 summarizes the specifications and settings of all RF components locating in the PRBS modulation branch and the PRBS demodulation branch.

Table 4-8 RF components utilized in the system.

Branch	Models	Quan.	Function	Manufacturer
PRBS Modulation	ADCH-80+	x 4	RF choke	Mini-Circuits
	ZKL-2R5	× 1	RF amplifier	
	ERA-3	× 2	RF amplifier	
	ZFL-11AD+	× 2	RF amplifier	
PRBS Reference	ZFBT-6GW-FT	× 1	Bias tee	Mini-Circuits
	ZJL-6G+	× 1	RF amplifier	
	BW-S3W2	× 2	RF attenuator	
	BW-S10W2	× 1	RF attenuator	
PRBS Demodulation	SYM-2500	× 4	Frequency mixer	Mini-Circuits
	ZFSC-2-11+	× 2	Power splitter	
	ZFSC-2-2500+	× 2	Power splitter	

4.2.4.6 Peltier cooler for APD

The APD is highly sensitive to environmental temperature, which requires a stable temperature environment for O/E conversion. The prototype system uses an external *Peltier* cooler for this purpose. The temperature around the APD is stabilized at 22 ± 0.05 ^{o}C at steady state. The thermal sensor is model MP-2731 from TETECH [168] and the controller is PID-1500 from WAVELENGTH ELECTRONICS [169]. The thermal sensor MP2731 is a negative thermoresistor with temperature sensitivity of ±0.15 ^{o}C. With on-board PID parameter configurations, the temperature around the APDs can be stabilized in 15-20 min. The temperature controller PID-1500 offers ultra low drifting performance – about ±0.005 C in 24 hours.

Once the temperature around the APD stabilizes, the O/E convention fluctuations induced by the temperature fluctuation are less than 1%, which offers sufficient reliability for TPSF acquisition.

4.2.4.7 Peltier heater for MZM

On the other hand, it is necessary to enhance the ambient temperature for intensity modulator from room temperature (25 ^{o}C) to a higher level (e.g. 40 ^{o}C). This heating aims to enhance the mobility of the photon electrons and minimize the detrimental photorefractive effect.

In our system, a Peltier heater (PID-1500, WAVELENGTH ELECTRONICS company) is utilized to stabilize the ambient temperature around the MZM at 42 ± 0.5 ^{o}C. The thermalresistor is TH10K from THORLABS company [170] and the thermal controller is TC-24-10 from TETECK [171]. The thermalresistor TH10K is negative thermoresistor and the resolution is ±1 Celsius degrees. This temperature stabilization can be realized in 20 minutes.

4.2.4.8 Bias controller for MZM

4.2.4.8.1 Bias-drift effect

The modulated output power of $LiNbO_3$ MZM versus the applied voltages (bias) can be expressed as a *modulation transfer function* [172-175].

$$P_o(V_b,t,T)=\frac{A\cdot P_i}{2}\left\{1+\cos[\frac{\pi\cdot V_b}{V_\pi}+\theta+\varphi(t,T)]\right\}. \quad (4\text{-}4)$$

where t is time, T is ambient temperature, A denotes the insertion loss, P_i stands for the input optical power, V_b is the modulating bias voltage, V_π is the intrinsic parameter of the $LiNbO_3$ substrate which indicates a half-wave voltage to turn P_o from the maximum level (P_o^{max}) to the minimum level (P_o^{min}), θ is a known constant phase and $\varphi(t,T)$ is a time- and temperature-dependent variable which is subject to the intrinsic $LiNbO_3$ substrate photorefractive effect and the temperature changes. It is this factor that causes the detrimental bias-drift effect.

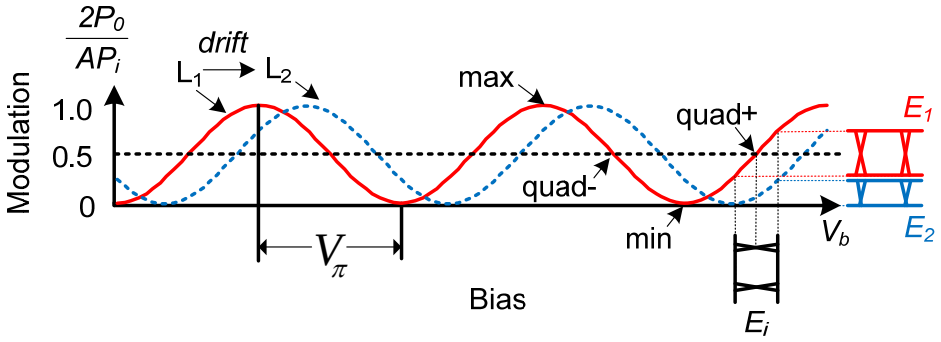

Fig. 4-13 Modulation transfer function (L_1) and bias-drift effect (L_2) of the interferometric $LiNbO_3$ intensity modulator.

Fig. 4-13 illustrates the bias-drift effect (from curve L1 to L2) in terms of eye diagram. In most analog modulation applications, MZM is biased at 50% transmission of the modulation output P_o^{max}, or the 'quadrature' point

(positive ‘quad+’ or negative ‘quad-‘) to maximize the modulation linearity. In our TD-DOT application, where a 2.488 Gb/s PRBS is used by setting the bias of MZM at ‘quad+’, the opened eye (at diagram E1) will gradually change its shape and may completely close (at diagram E2). That means the modulation depth of MZM will lose its stability. As a result, the correlation detection begins fluctuating. Obviously it is necessary to introduce an bias controller to correct the bias drifting effect by tracking and locking the working point at the ‘quad+’ point.

4.2.4.8.2 Bias controller

The bias controller for ‘quad+’ point tracking is working in a dither-then-difference mode. Fig. 4-14 and Fig. 4-15 show the schematic. A 2.5 kHz square wave that falls well outside of effective spectra of the 2.488-Gbps PRBS modulation signal is generated by DAQ and serves as a dither signal S_d. It has a data length which equals to 8 periods. The peak-to-peak amplitude is fixed to V_π. In addition, a DC voltage V_b from microcontroller is superimposed on S_d and the biased dither signal ($S_d + V_b$) is fed into the MZM through the DC port (see Fig. 4-14). The corresponding modulation results A_{mod} are sampled $2N$ (N = 8) times by the MCU: N samples are acquired for MZM biasing at high dither bias V_b^H; the other N samples are acquired for MZM biasing at low dither bias V_b^L, where $V_b^H = V_b^L + V_\pi$. The summation of N -sample differential amplitudes, defined by Eq. (4-5), indicates the modulation depth for MZM biasing at voltage $V_b = V_b^L$.

$$\Delta_{V_b} = \sum_{i=1}^{N=8} [A_{mod}^H(i) - A_{mod}^L(i)] \tag{4-5}$$

$$\Delta_{V_b} = \begin{cases} 0, & V_b = \left[V_b^{quad+}, V_b^{quad-}\right]; \\ \Delta_{V_b}^{max}, & V_b = V_b^{min}; \\ \Delta_{V_b}^{min}, & V_b = V_b^{max}; \end{cases} \tag{4-6}$$

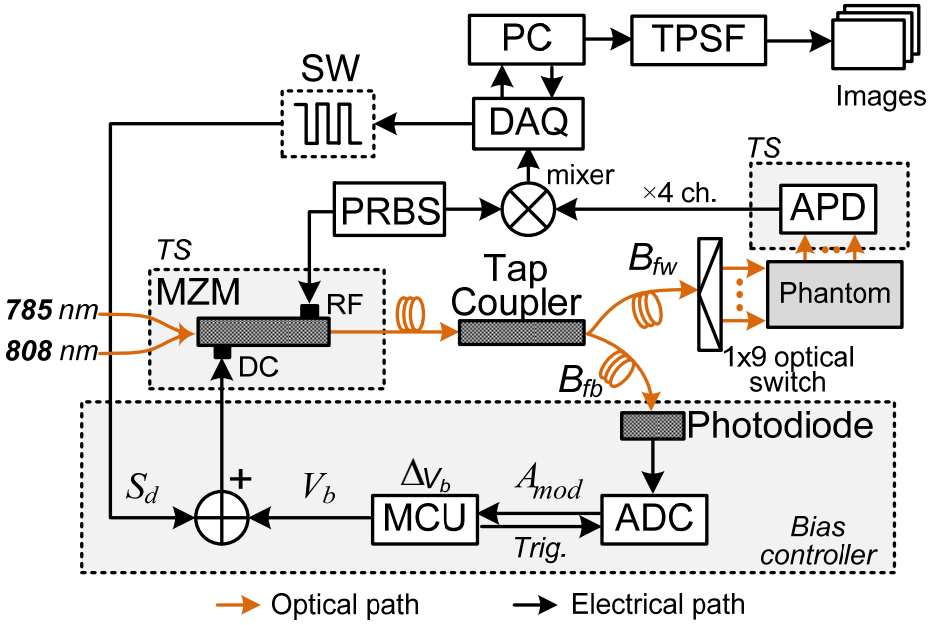

Fig. 4-14 Schematic of fast TD-DOT system and the dither-and-difference bias controller.

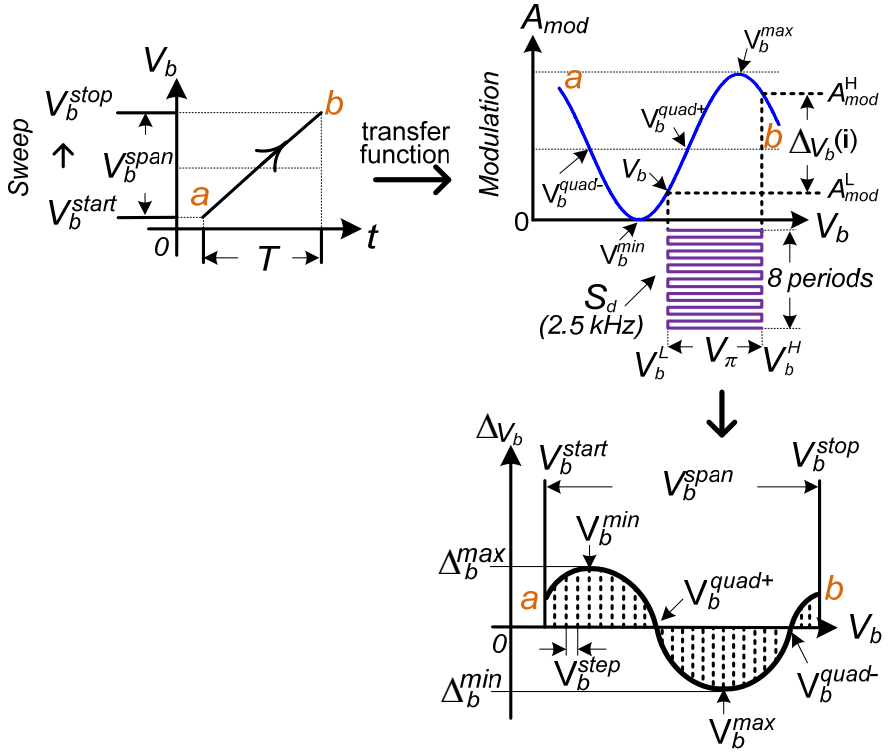

Fig. 4-15 Schematic of bias controller for 'quad+' point tracking.

To find out the 'quad+' point, the microcontroller starts bias sweeping in a step of $0.05V_\pi$ from an arbitrary bias V_b^{start} and simultaneously checks the polarity of quantity Δ_{V_b} until it changes from positive to negative for the first time. After that, the sweeping step decreases to a smaller size $0.01V_\pi$. At each bias step, the corresponding Δ_{V_b} compares with Δ_{V_b} at previous bias step and the smaller one is retained by MCU as the new reference for the succeeding comparisons. The bias sweeping and the iterative comparison stop until Δ_{V_b} equals to or very close to zero. Then the desired 'quad+' point V_b^{quad+} can be inferred. The arbitrarily assigned bias V_b^{start} can be substituted by the V_b^{quad+} so that the succeeding bias tracking procedure can be speeded up. For the worst case that a span of $2V_\pi$ have to be swept before finding out the 'quad+', a number of 200 $\Delta_{V_b}(j)$ ($j \in [1,2...200]$) acquisitions have to be performed. It will take about 12.8 seconds. In this a period, the distortion of the $\Delta_{V_b}(j)$ caused by the photorefractive effect and temperature changes can be ignored because the bias-drift is usually a slow, gradual process. However, to tolerate this worst case at stating stage and prevent MZM from over-biasing damage, the bias sweeping span is set as $V_b^{stop} = V_b^{start} + V_b^{span} = V_b^{start} + 4V_\pi$. The bias hops $4V_\pi$ backward to resume the bias tracking as long as it sweeps beyond V_b^{stop}.

Fig. 4-16 shows the bias controller for 'quad+' point tracking by using the MSP430F-4270 from Texas Instrument Company as the core chip. Appendix A.1 describes the circuit design, PCB layout and C-code burning in the ROM of the microcontroller chip in detail.

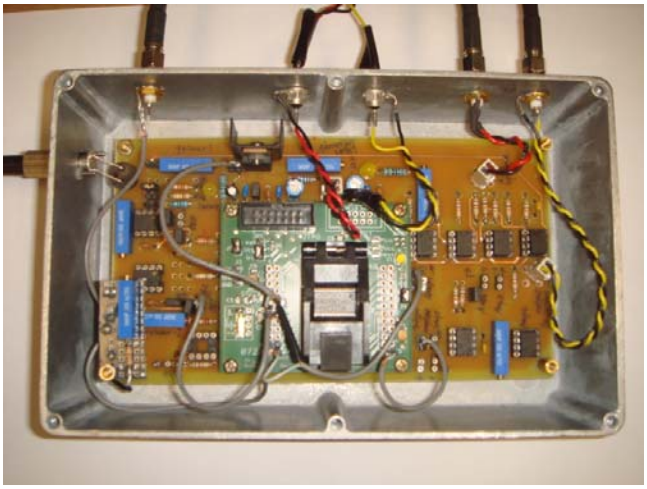

Fig. 4-16 MZM bias controller for ‘quad+’ point tracking.

4.2.5 Mechanical modules

4.2.5.1 Hand-held probe

The hand-held probe is designed to work in reflectance mode. All 9 light source fibers and 4 detection fiber bundles (quartz light guides) are mounted on the hand-held probe. The fiber tips are aligned to the probe surface. The positions of 9 light source fibers and 4 fiber bundles are arranged in a spatial layout as shown in Fig. 4-17. Table 4-9 shows handheld probe’s dimensions. The surface of the probe is painted black to prevent the optical signals from going back into the phantom/tissue. With this approach, the semi-infinite boundary condition can be applied for tomographic image reconstruction.

A few design criteria have to be taken into account during designing the layout of the hand-held probe. The first rule is the optimization of the dynamic range that the probe could provide. The second rule is the minimum of the data redundancy. The third rule is about the imaging area. Each criterion has been allocated a certain weight during optimization simulation.

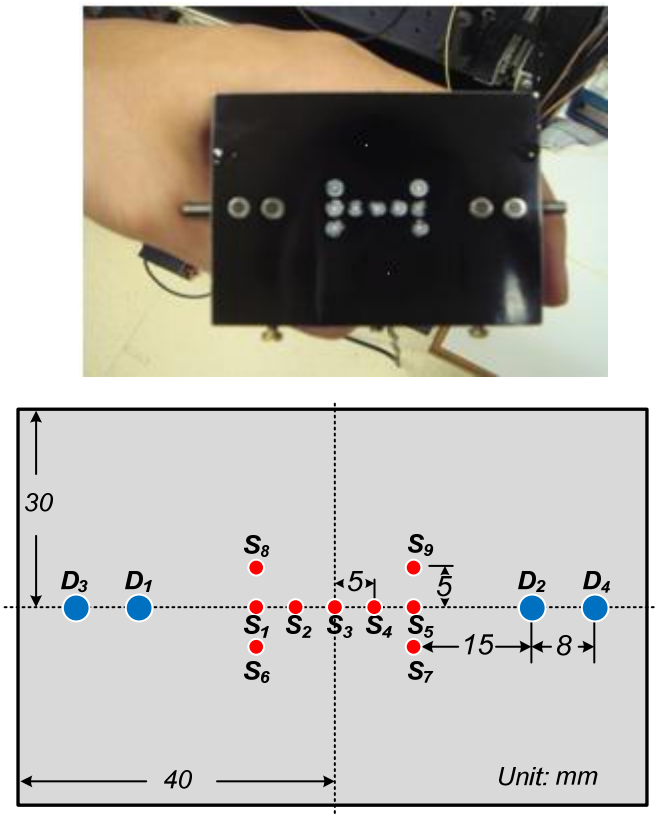

Fig. 4-17 *Top*: Picture of the hand-held probe. *Bottom*: Design of the hand-held probe. The small red spots represent light source fibers. The large blue spots represent detection fiber bundles.

Table 4-9 Separations of source (S_n) to doctor (D_m) on the hand-held probe (unit: cm).

	D_1	D_2	D_3	D_4
S_1	1.5	3.5	2.3	4.3
S_2	2	3	2.8	3.8
S_3	2.5	2.5	3.3	3.3
S_4	3	2	3.8	2.8
S_5	3.5	1.5	4.3	2.3
S_6	1.5811	3.5355	2.3537*	4.329
S_7	3.5355	1.5811	4.329	2.3537*
S_8	1.5811	3.5355	2.3537*	4.329
S_9	3.5355	1.5811	4.329	2.3537*

*source-detection pairs for *in-vivo* spectroscopy experiments.

4.2.6 Auxiliary modules

There are some other devices that are not directly involved in the signal processing. Therefore they are mentioned briefly here.

- Linear mode (MPU series, POWER-ONE, UK) and switch mode (TML series, TRACO) power supplies unit to convert 240 VAC to ±12 V, ±5 V and other DC voltages;
- NECL terminator (PRL-550NQ4, Pulse Lab, US) to convert the NECL signals from the programmable digital delay line into a 50Ω-terminating RF amplifier.
- Photodiode (VTB5051J, PerkinElmer Optoelectronics) for monitoring the feedback from the Y-branch tap coupler;
- A commercialized digital transmission measuring instrument: SDH/SONET analyzer (ME3620A, Anritsu, Japan) for PRBS signal generation. It is used to offer a quick startup for prototype system testing;
- Two digital storage oscilloscopes (DSO) that are intensively used for signal integrity analyzing and circuit trouble-shooting. One DSO is Agilent 54852A (2 GHz bandwidth, maximum sampling rate 10 GS/s) from Agilent, US. The other one is Wave Surfer 422 (200 MHz bandwidth, maximum sampling rate 2 GS/s) from LECROY, US;
- High voltage (HV) linear power supplier (CA02P, EMCO, US) for APDs DC biasing.
- RG-58U coaxial cables with a certain length to assist the PDDL for PRBS transmission delay control and interconnect every lump RF components. RG-58U coaxial cables keep uniform characteristic

impedance of 50 Ω up to few GHz in room temperature which minimizes the reflectance effect of the PRBS signals in transmission paths due to the impedance mismatch.

- A high speed amplified photoreceiver (Model P-101, 850 nm receivers, CSI, US) as the PRBS modulation detector.
- High speed VESEL laser source (Model V-126, 850 nm VESEL, CSI, US) for PRBS modulation verification at quick prototype system startup.

4.2.7 Controlling automation

The prototype system uses data acquisition card (model: USB-6251, National Instrument). LabVIEW™ and Matlab™ compatible user consoles (GUI) are constructed.

4.2.7.1 Data acquisition card (DAQ)

The NI data acquisition card USB-6251 is a high-speed multichannel multifunctional DAQ card, offering superior accuracy with fast sampling rates [176]. It can acquired analog input/output (AI/AO) signal from up to 16 single-end or 8 differential channels at a sampling rate up to 250 KS/s/ch. This capability satisfies our requirement to acquire TPSF signals from 4 channels in parallel. Table 4-10 summarizes the main specifications of USB-6251.

Table 4-10 Main specifications of the DAQ card

Card Model	USB-6251
Channels	16 SE/8 DI AI; 2 AO; 24 DIO;
Sampling rate (*MS/s*)	1.25 (AI); 2.86 (AO);
Voltage range (*V*)	-10 - +10
Max clock rate (*MHz*)	10
Resolution (*bit*)	16
Logic level	TTL
Number of counter/timer	2
Software	LabVIEW, DAQmax
Manufacturer	National Instrument, US

4.2.7.2 User console GUI

The LabVIEW and Matlab based enable user to control systems hardware, monitor system parameters, alarm system failure, enable the acquisition and display of timing histograms (TPSFs), and facilitates fully automatic execution of complete imaging scans.

For this purpose, a full feature DOT/DOS GUI control console interface was programed, which combines the functions including the tomographic imaging and the time-resolved spectroscopy. In addition, the GUI offers real-time information including the temperature monitoring, Mach-Zehnder bias controlling, LD power manipulation, automatic system calibration, optical sweeping control, data analyzing and logging.

The software platform includes LabVIEW (ver. 8.0) and Matlab (xer. 2006a, Mathworks) on the MS windows XP Professional SP3. Real-time data acquisition in LabVIEW and the data processing in the MATLAB are communicated via MS windows ActiveX technique.

Fig. 4-18 and Fig. 4-19 shows the full features DOT/DOS user console. Appendix A.5 details each function of user console.

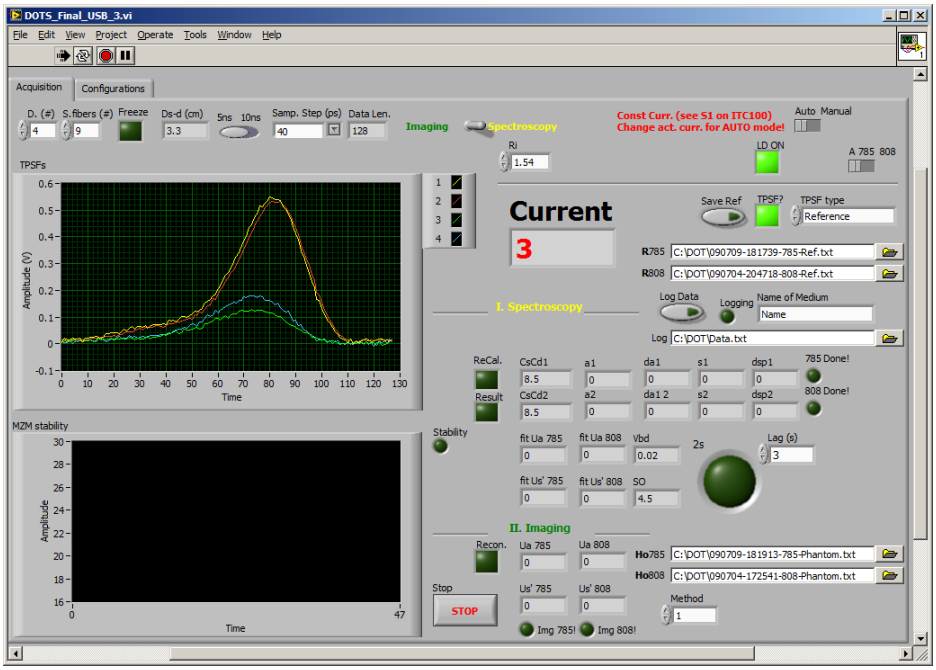

Fig. 4-18 User console GUI for TPSF “Acquisitions”.

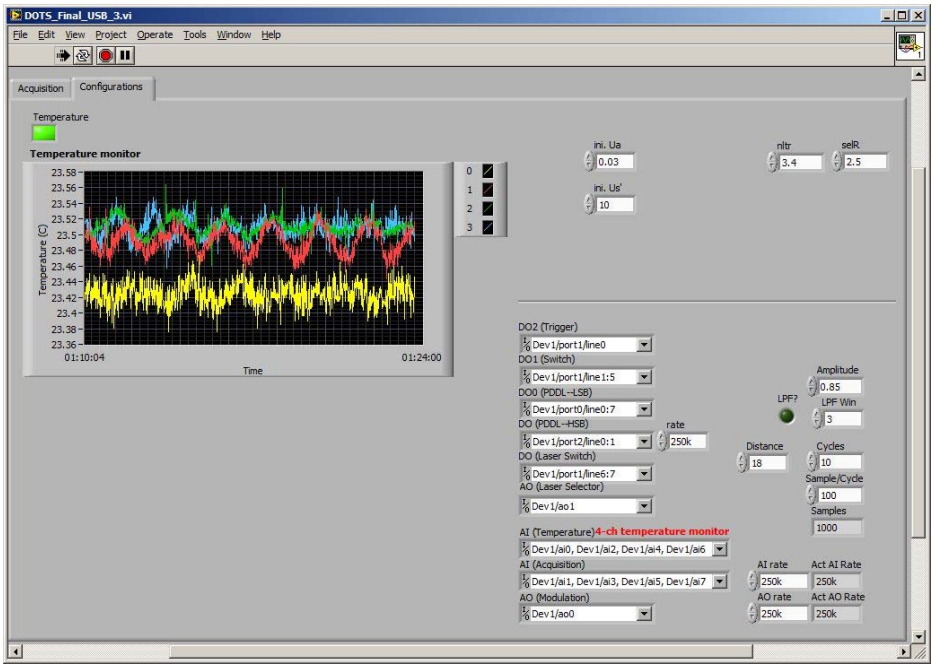

Fig. 4-19 User console GUI for DOT/DOS system “Configurations”.

4.2.7.3 Instrument control and data acquisition

Fig. 4-20 shows the control schematic of the DOT system.

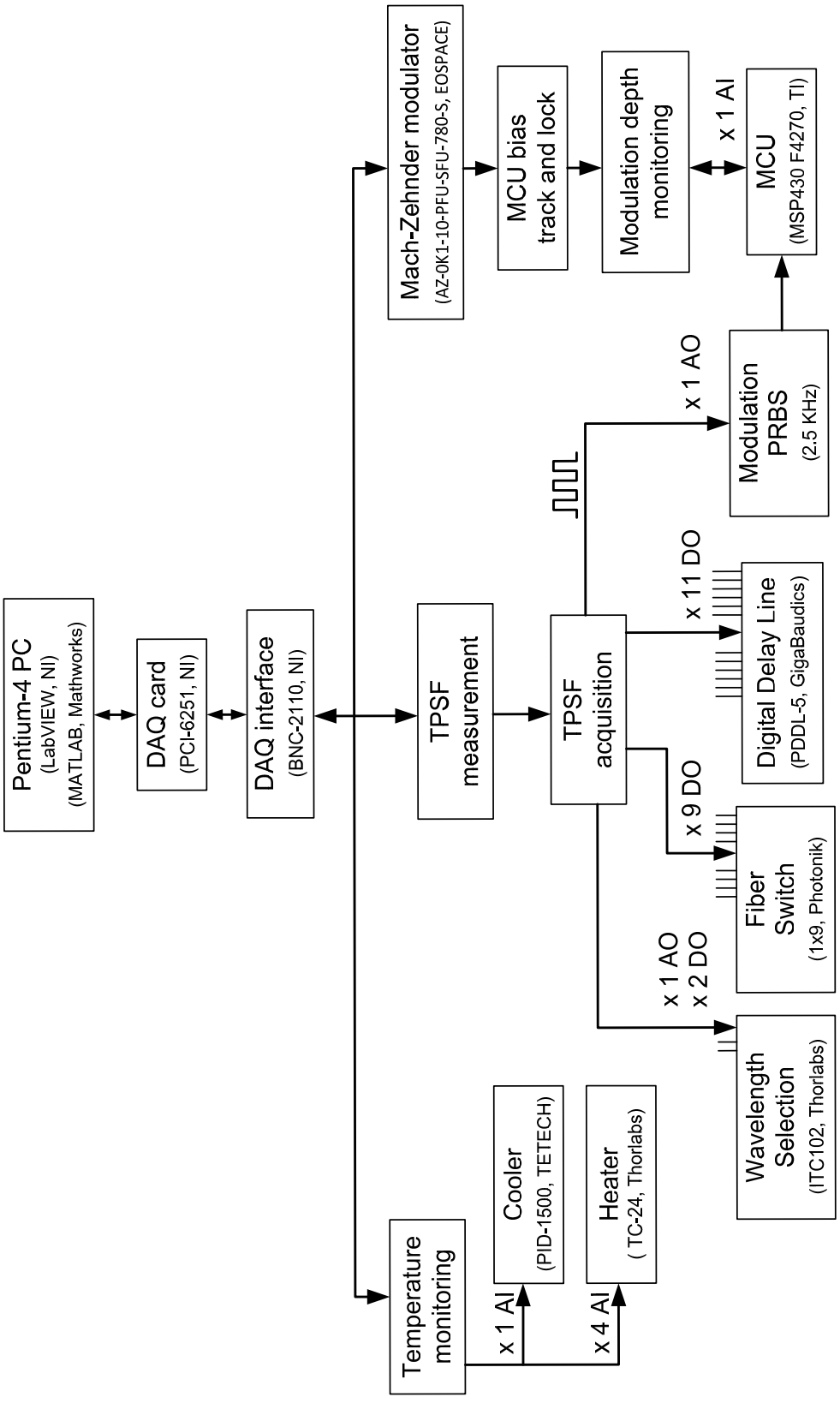

Fig. 4-20 Schematic of user console GUI in DOT prototype system.

4.2.7.4 Data acquisition protocol

4.2.7.4.1 TPSF data format

The TPSF data are saved in three datasets: 1) system response; 2) TPSF from homogeneous phantom and 3) TPSF from tissue/heterogenous. For multiple light source fibers and multiple fiber bundles (e.g. 9 light sources by 4 detectors), the dataset for each source-to-detector pair is organized as:

Line 1: S1, D1
Line2: S1, D2
Line 3: S1, D3
Line 4: S1, D4
Line 5: S2, D1
Line 6: S2, D2
Line7: S2, D3
…
Line 35: S9, D3
Line 36: S9, D4

Here, S denotes the light source which ranges from 1 to N_s ($N_s \leq 9$). D represents the detector which ranges from 1 to N_d ($N_d \leq 4$). Each TPSF line consists of M data (M = 128 and equals to the TPSF data length).

For an example in which all 9 light sources and 4 detectors are involved, each scanning generates 36 TPSFs. All TPSF data are arranged in 36 rows and saved as TEXT ('.txt') file.

4.2.7.4.2 Data logging

The organization of the spectroscopic data is list in rows. Each row has 13 columns. The meaning of each column is described in Table 4-11. The latest spectroscopic data will be appended to the bottom of the existing data.

Table 4-11 Data type of each column in spectroscopic analyses.

Col	**1**	**2**	**3**	**4**	**5**	**6**	**7**	**8**	**9**	**10**	**11**	**12**	**13**
Data type	Name of the tissue	Logging Date & Time (12 bit)	Source numbers	Detector numbers	Sampling step	Wavelength 1(e.g. **785** nm)	Absorption coefficient at **785** nm	Absorption coefficient at **785** nm	Wavelength 2(e.g. **808** nm)	Absorption coefficient at **808** nm	Absorption coefficient at **808** nm	Oxygenation saturation (***SO***)	Total hemoglobin concentration (***THC***)

4.3 System performance evaluation

4.3.1 System warm up

The system should be warmed up sufficiently before conducting experiment. The system warm-up will activate the *Peltier* cooler and heater for temperature stabilization on APD and MZM.

4.3.1.1 Temperature fluctuations

First of all, the temperature stabilization around the APD is very important. As showing in Table 4-6, the temperature coefficient of the APD is 0.65 V/C. Without active temperature control, the heat generated from optoelectric conversions will increase the proximity temperature of the APD. In a short period, the O/E conversion efficiency of the APD will significantly decrease.

Fig. 4-21 shows the temperature stabilization procedure since system warm-up begins by applying the active *Peltier* cooler control. The temperature will reach steady state of $23.4 \pm 0.15\ ^{o}C$ in 15-20 minutes.

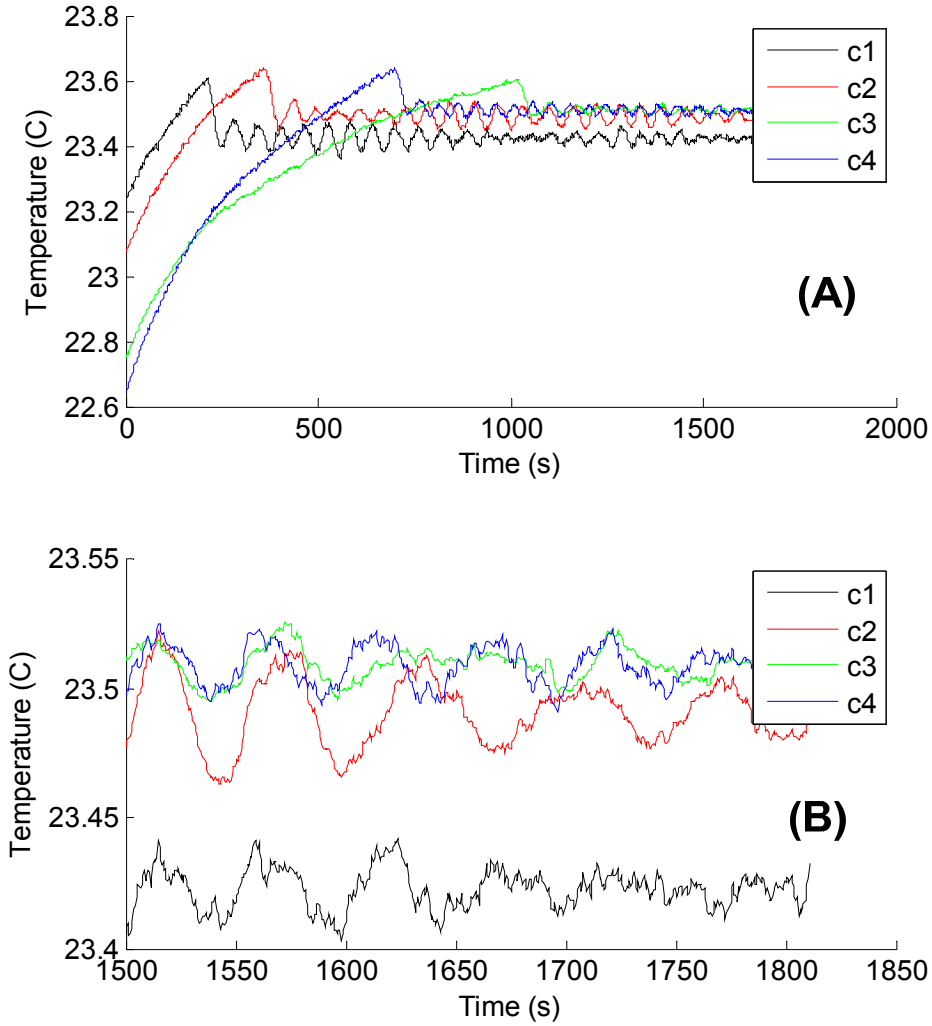

Fig. 4-21 Temperature stabilization around four APDs (c1-c4). (A) Dynamic state. (B) Steady state.

For the other components, fluctuation of a few degrees in the ambient temperature can also induce drift or fluctuations on the TPSF measurement. For example, the RG-58 A/U coaxial cable used in the PRBS transmission has a phase delay specification of ~150 ppm/^{o}C, corresponding to ~1 ps/^{o}C per meter of cable. Keeping the room temperature constant (e.g. 25 ^{o}C) is also crucial to minimize the stability of the TPSF measurement. Similarly, the minimized cable length can also minimize these undesired effects. In the

future design, it may also be advisable to choose cable types that have been designed to exhibit small phase delay variations with temperature.

4.3.1.2 Power drift of the laser diodes

The laser diode driver (ITC 102, Thorlabs, Table 4-2) provides a noise level of < 2 μA and a stability of < 20 μA within 30 minutes. The temperature coefficient is less than ±50 ppm/^{o}C. For a constant current mode, two NIR LDs can work stable within one hour, with power drifting being less than ±1%. The instant power fluctuations are approximately ±1.3%.

4.3.2 System noise

The noise levels in the system can be categorized into two classes. Type I noise is the system floor noise, which is determined by the performance of the system devices. This kind of noise is very small compared with other two kinds of noise level. Fig. 4-22 illustrates the device's inherent noise level in the system. The noise level has consistent peak-to-peak amplitude about Vp-p ≈ ±0.0001 V. Type II noise is cross talk noise, which is majorly caused by the cross talk between PRBS transmission lines as well as the resultant ground bounce. Fig. 4-23 shows the class II noise has a consistent peak-to-peak noise approximately of Vp-p ≈ ±0.01 V, which is about 100-folder larger than class I noise. It thus contributes to the main noise in the DOT/DOS system and the TPSF acquisitions.

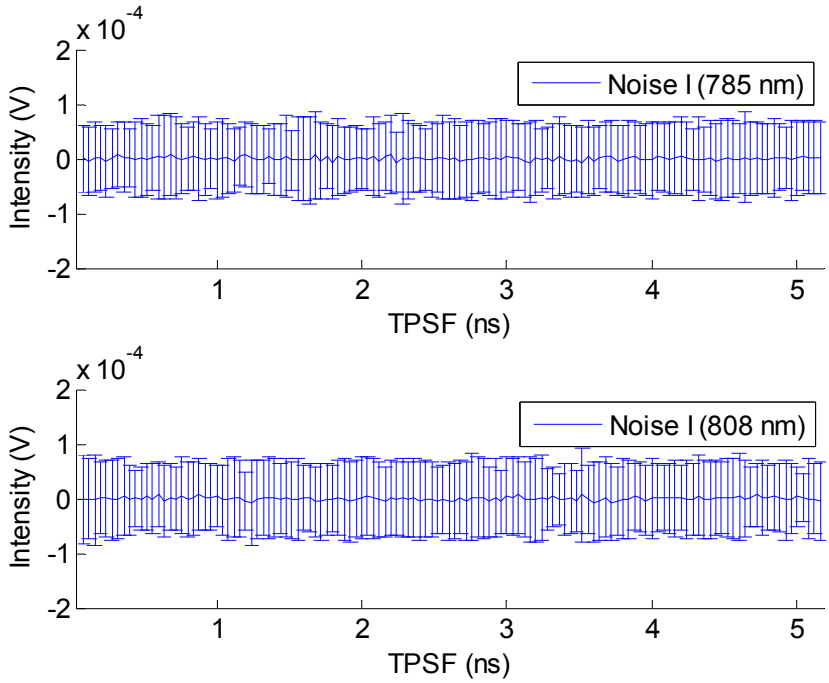

Fig. 4-22 Type I noise (noise floor): random noise associated with system devices. Error bar shows the standard deviation.

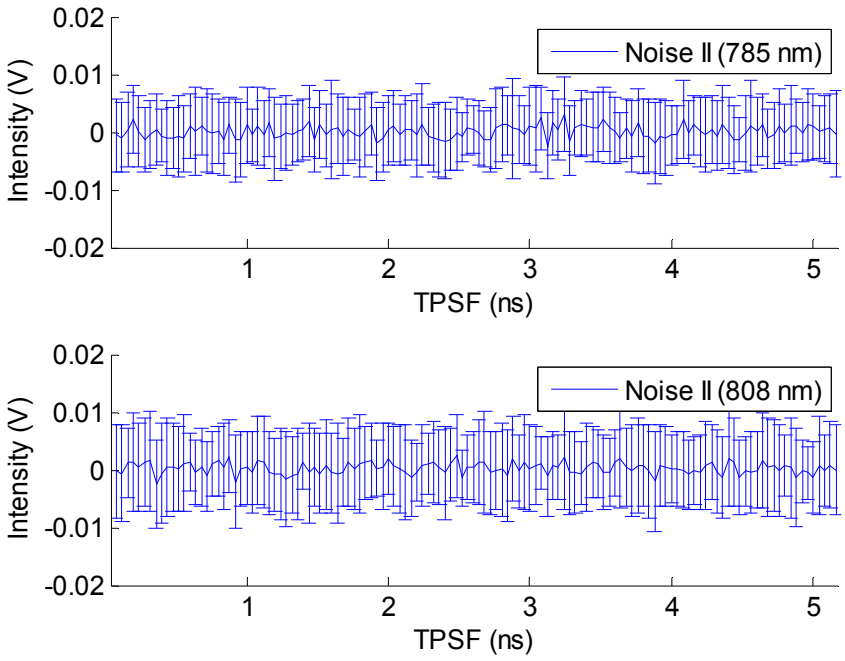

Fig. 4-23 Type II noise: noise level caused by the correlation of PRBS. Error bar shows the standard deviation.

4.3.3 Data acquisition speed

The TPSF data acquisition speed is depended on a couple of factors.

4.3.3.1 Fiber optical switch

As mentioned before, 9 light source fibers multiplexed one by one. The time required for sweeping between adjacent two fibers is less than 10 ms (see Table 4-5). This time consumption is negligible. However, when the fiber returns from fiber 9 back to fiber 1, it requires extra time consumption due to the component's internal electricmechanical mechanism. Therefore the user console pause the data acquisition for 200 ms until the first fiber is ready to start.

4.3.3.2 Modulation and Demodulation for noise minimization

Besides the optics fiber switch effect, the auxiliary system noise minimization also slow down the TPSF data acquisition speed. Because of the crosstalk effect, the TPSF signals are susceptible to the PRBS interference. It is difficult to minimize the noise caused by this effect. A passive solution is to use an additional modulation and demodulation technique to minimize this noise. In our system, a 2.5 kHz square wave from NI-DAQ injects into the DC port of the MZM. In addition, this 2.5 kHz square wave modulates the PRBS-modulated light in a very low frequency comparing with the PRBS modulation (see Fig. 4-14). The low frequency of 2.5 kHz is specified to avoid interference with the broad spectrum PRBS signal.

After PRBS demodulation finishes, i.e. at the mixer's IF port (see Fig. 4-14), the TSPFs should be additionally demodulated using software to reduce the signal noise. The cross-correlation with reference 2.5 kHz square wave can significantly increase the signal-to-noise ratio of TPSF acquisition. Yet the overall data acquisition time will elongates. This is because the DAQ card can

only support data acquisition rate up to 250 KS/s for 8 differential AI/AO channels in parallel.

For the optimal configuration, the 2.5 kHz modulation square wave is sampled in a rate of 250 KS/s, the data length for each modulation is 10 cycle. Each cycle consists 100 sampling points: 50 positive ones and 50 negative ones. Then the time to acquire 1000 sampling points (= 10 cycles × 100 S/cycles) in a rate of 250 KS/s would be 1000/250KS/s = 4 ms. To acquired a TPSF of 128 sampling points, it will take 128 × 4 = 512 ms. With regardto the fiber switch from fiber 1 to fiber 9, the total time is approximately 512 × 9 + 10 × 9 = 4.698 s for one complete scanning.

4.3.4 System calibration

4.3.4.1 System response

In order to assess the system's impulse response (SIR), we place a piece of diffusive white paper 18 cm away in front of the handheld probe (see Fig. 4-24). Since the light beam from an optical fiber is diverging to the paper and the reflection from the white paper is diffusive, the specified distance of 18 cm provides an appropriate attenuation of the light intensity which is collected by the fiber bundles and fiber coupled to the APDs eventually. To minimize the undesired photon splashing, an absorptive medium (e.g. an absorptive black cloth) is placed in between the probe and the diffusive plane.

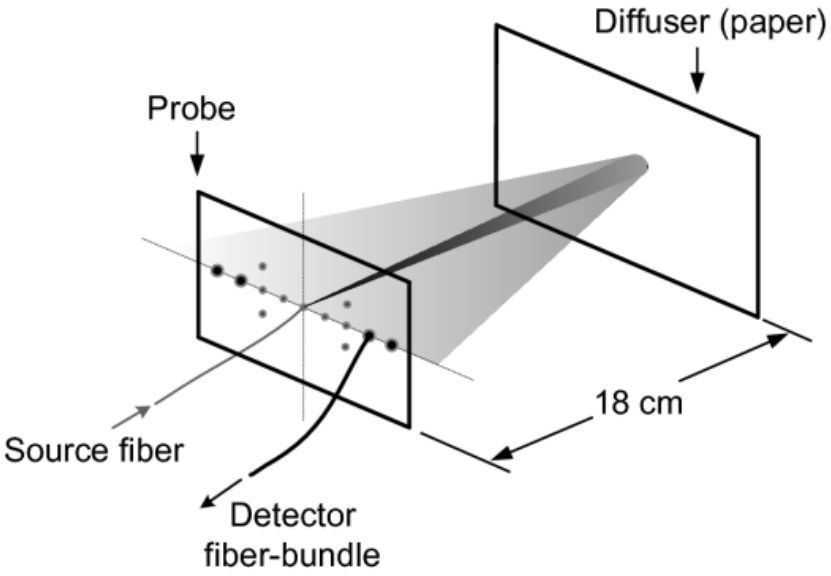

Fig. 4-24 System setup for system impulse response assessment.

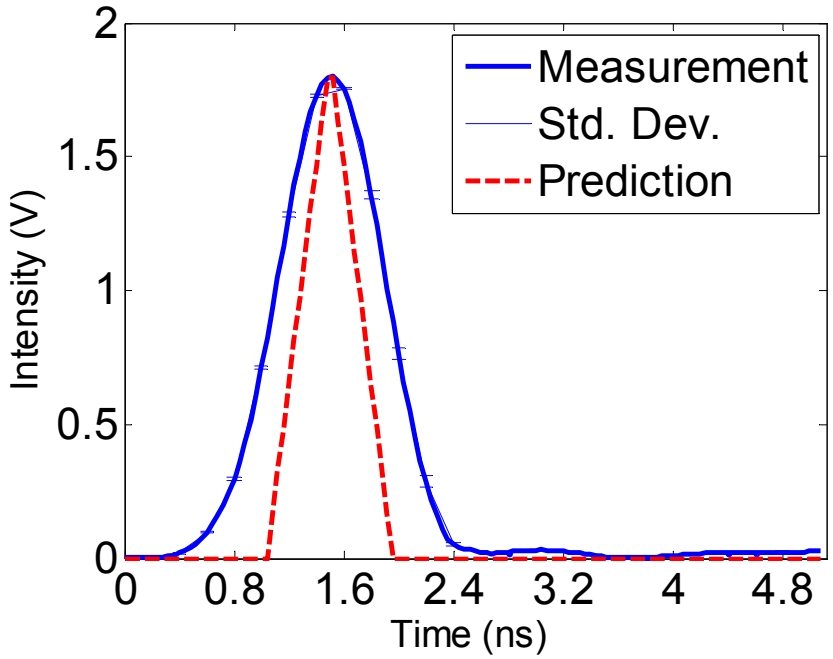

Fig. 4-25 SIR acquisition vs. prediction of the PRBS autocorrelation.

Fig. 4-25 plots one of 36 SIR TPSFs (blue solid curve) together with the theoretical prediction (red dashed curve), i.e., the PRBS autocorrelation. The acquired SIR TPSF has a FWHM approximately of 810 ps. The rise time and the fall time (10% - 90%) are both around 600 ps. These values are larger than the theoretical prediction whose FWHM is at 402 ps and the rise time of 360

ps (see Fig. 4-3). This signal integrity degradation is mainly caused by the junction capacitance (≈ 6 pF, see Table 4-6) of the APDs and the insufficient bandwidth of the components along the PRBS signal transmission path. If all components in the system have an adequate bandwidth, the shape of the measured SIR TPSFs would approach to the prediction curve.

4.3.4.2 System repeatability

The SIR is also selected to quantify the stability of the acquired time-resolved signals. The error bars in Fig. 4-25 represent the standard deviations of the measured SIR among different channels. The variation is less than ± 2%, which shows a very good uniformity among the acquisitions.

4.3.4.3 System stability

The overall system stability is dominated by the stability of modulation depth.

4.3.4.3.1 Evaluation

In order to quantitatively evaluate the bias tracking performance and the stability improvement of the TPSF measurements by adopting the active bias controller described in section 4.2.4.8, TPSFs were acquired from tissue-like phantom experiments. As showing in Fig. 4-26, each TPSF consists of 128 temporal sampling points with temporal interval of 40 ps. The normalized summation of TPSF amplitudes, denoted by $A_{norm}^{TPSF} = \frac{1}{S} \cdot \sum_{i=1}^{128} A^{TPSF}(i)$ is selected to quantify the stability of the modulation depth. Here $A^{TPSF}(i)$ denotes the *i*th ($i \in [1...128]$) amplitude of a TPSF. The normalization constant

$S = \sum_{i=1}^{128} A_{quad+}^{TPSF}(i)$ is the summation of all TPSF amplitudes for MZM biasing around the 'quad+' point.

Table 4-12 Configurations of bias controller for 'quad+' point tracking

Configurations (unit)	Values
Wavelength (nm)	785; 808
Temperature of MZM (^oC)	25 ± 0.03; 40 ± 0.03
Dither signal: frequency, f_{dither}^{sqr} (kHz)	2.5
Dither signal: duty cycle *(%)*	50
Dither signal: amplitude (V)	V_π
Sweeping step-size, V_b^{step} (V)	0.01 V_π – 0.05 V_π
Initial bias, V_b^{start} (V)	1
Max sweeping span, V_b^{span} (V)	$4V_\pi$
Samples of the dither signals	16

It is reasonable to use quantity A_{norm}^{TPSF} to evaluate the bias shifting effect because $A^{TPSF}(i)$ is proportional to the modulated optical power. The modulated optical power is determined by the modulation depth of MZM when the factor of temperature becomes negligible. So the quantity A_{norm}^{TPSF} directly reflects the modulation depth with respect to the maximal value which is achievable only is MZM biased at the 'quad+' point.

From the perspective of image reconstruction, the accuracy of TPSF measurements is extraordinarily critical because the distortions of the TPSF signals induced by the modulation depth instability would be regarded as the contribution from heterogeneous optical properties locating in the objects. And eventually it may lead to errors on the image reconstruction results. This also

proves that A_{norm}^{TPSF} is a good indicator to quantify the stability of our TD-DOT system.

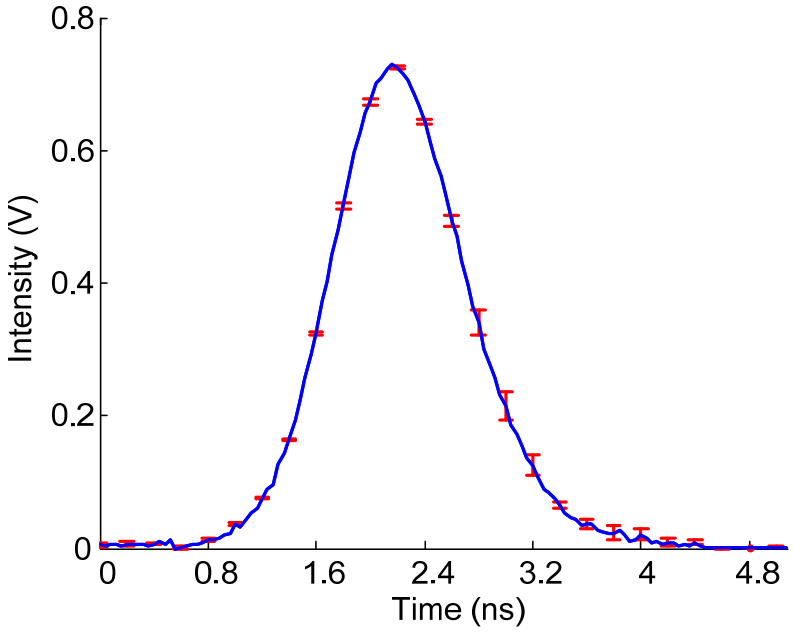

Fig. 4-26 TPSF acquired from phantom experiments. The error bars shows the standard deviations of measurements.

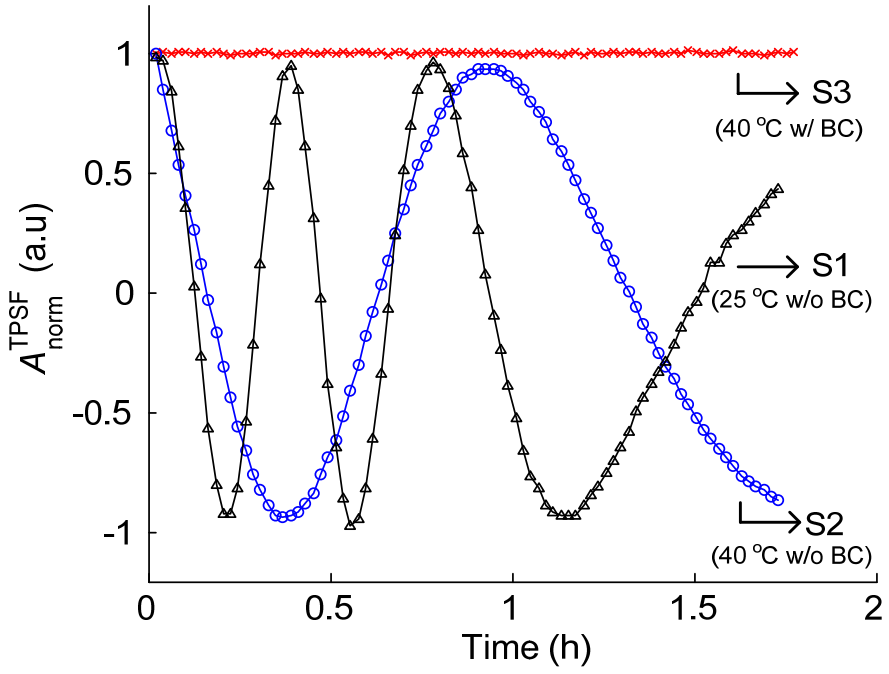

Fig. 4-27 Stability improvement of TPSF signals. (S1) at 25 °C w/o bias control, (S2) at 40 °C w/o bias control and (S3) at 40 °C w/ bias control.

Fig. 4-27 compares the stability improvement of the TPSF measurements A_{norm}^{TPSF} before and after applying the bias controller implemented in section 4.2.4.8. Curve S1 and S2 show the stability of the TPSF measurements A_{norm}^{TPSF} at temperatures of 25 ^{o}C and 40 ^{o}C without applying bias controller, respectively. Clearly the bias voltage fixed at system initialization stage fails to stabilize the modulation depth because the TPSF measurements fluctuate with time. A higher temperature of the MZM can only help slow down the oscillation of TPSFs [172]. Curve S3 shows a stabilized TPSF measurement after applying the proposed bias control. The oscillation of the TPSF measurements is almost eliminated. The amplitude fluctuation of A_{norm}^{TPSF} is less than ± 2% in hours' duration.

Figs. 4-28 (a) and (b) show the zoom-in views (blue curves) of the stabilized TPSF acquisition, A_{norm}^{TPSF} at a source-detector pair at two wavelengths (785 nm and 808 nm) after applying the proposed bias control. We chose the standard deviation σ_s of A_{norm}^{TPSF} in 1 minute to estimate controller's short-term stabilizing capability. Five such 1-minute periods were randomly selected and the mean value $\overline{\sigma}_s$ of five $\sigma_s(i)$ ($i \in [1...5]$) were found to be 0.0025 and 0.0027 for 785 nm and 808 nm, respectively. To evaluate the controller's long-term stabilizing capability, we utilized a linear equation $A_{norm}^{TPSF}(t) = at + b$ to fit the TPSF measurements and picked the slope coefficient a to estimate the drifting speed of the stabilized TPSF acquisition over time. The fitting results shown in Table 4-12 are plotted as red lines in Fig. 4-28. For all of 36 source-detector pairs (9 sources and 4 detectors), the mean values and standard deviations of the slope coefficient a are calculated and listed in Table

4-13. Fig. 4-28 and Table 4-13 show excellent short-term and long-term stabilities brought by our TD-DOT controller subsystem, respectively, which make our TD-DOT system eligible to acquire highly reproducible TPSF measurements within a period up to a few hours.

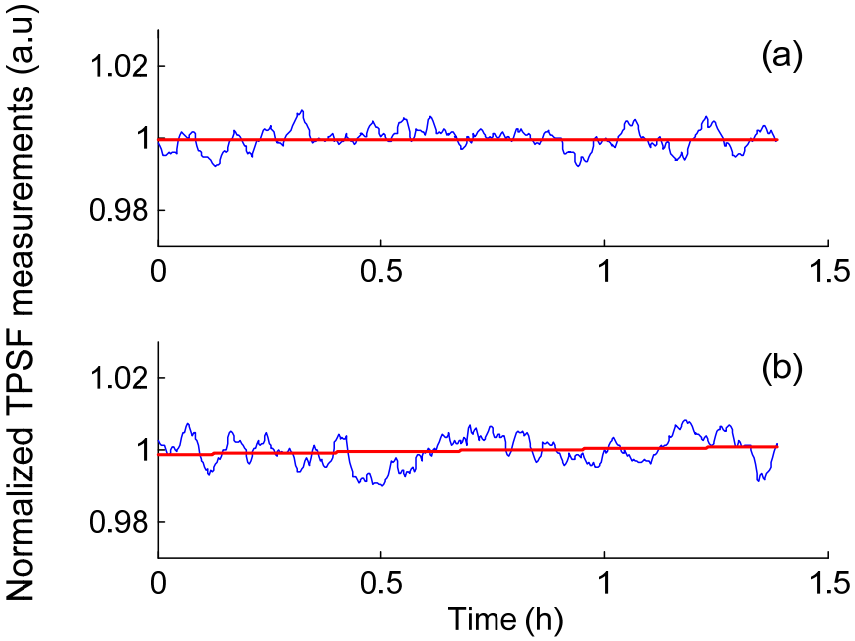

Fig. 4-28 Measurements (blue) and fitting results (red) of the TPSF measurements with time. (a) at 785 nm; (b) at 808 nm.

Table 4-13 Quantification of TPSF signals stability at two wavelengths

	Wavelength (nm)	$\bar{\sigma}_s$	Linear curve fitting $A_{norm}^{TPSF}(t) = at + b$			
			Fitting results	a (h^{-1})	$\bar{a}^*$ (h^{-1})	σ_a^* (h^{-1})
(a)	785	0.0025	$A_{norm}^{TPSF}(t) = 0.0001t + 0.9998$	0.0001	0.0002	0.0062
(b)	808	0.0027	$A_{norm}^{TPSF}(t) = 0.0011t + 0.9992$	0.0011	0.0015	0.0099

* Calculated from all of 36 TPSF acquisitions.

4.3.4.3.2 Bias reconfigurations

In addition to tracking the 'quad+' point, some other meaningful bias points such as the negative quadrature point ('quad-'), the maximum ('max') and the minimum point ('min') can also be tracked and locked using the controller

(see Fig. 4-15). The 'quad-' point can be locked by tracking the zero-crossing point on the rising edge. The 'max' or 'min' point can be locked by tracking the minimum or the maximum modulation difference, respectively. Changing and tracking the bias position of MZM among these four biasing points is easily configured by programming the microcontroller.

4.3.4.4 System parameters

In practice, the fiber coupling between the detection fiber bundles and the corresponding APDs cannot keep uniform. The variation of inter-channel coupling coefficient will bring in a slight difference to the TPSF measurements. Prior to data processing, these inter-channel coupling differences should be quantified.

Fig. 4-29 shows the setup for fiber coupling coefficients characterization. The glass tank was filled with Lipofundin (B. Braun, MCT/LCT 20%) lipid emulsion. The concentration of Lipofundin lipid emulsion was 0.6%, which can mimic the normal human breast tissue. The optical properties of these liquid tissue-like phantoms include the absorption coefficient $\mu_a \approx 0.02$ cm^{-1} and the reduced scattering coefficient $\mu_s' \approx 6.0$ cm^{-1} [11, 177 178]. The total volume of the Lipofundin solution is 17 cm (length) × 15 cm (width) × 10 cm (depth). The hand-held probe was placed on the solution surface. For this setup, the Lipofundin volume can be regarded as a semi-infinite background medium.

The calibration procedure and algorithms can be found in section 5.2.1 and Appendix A.6.

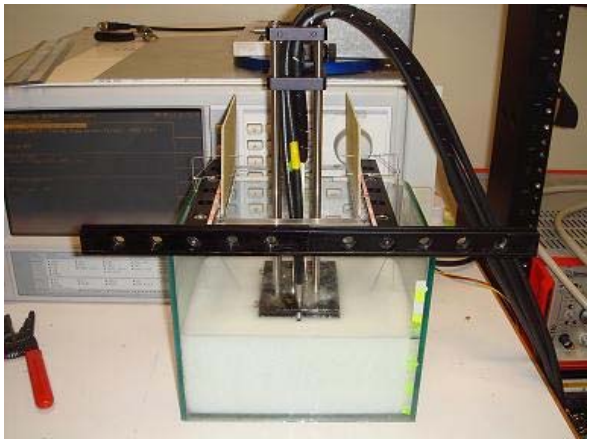

Fig. 4-29 System setup for phantom experiment.

4.3.5 System limitations

In addition to the limitation of temporal resolution (~ 800 ps), the prototype system has some other limitations, which deserves very careful handlings.

4.3.5.1 Dynamic range

The linear voltage signal that DAQ card can detect is [-10…+10] V. Signals beyond this range will saturate the TPSF acquisition. This will happen especially in the following two situations:

1) The absorption coefficient of the tissue is very low, e.g. aged women with very fatty breast tissues;
2) The incident optical power is too high, which leads to a high emission power.

According to Fig. 4-23, the acquisition subsystem has floor noise about 5-10 mV. If the maximum linear detectable range is 10 V, the maximum dynamic range is approximately of $20 \times \lg (10V/10mV) = 60$ dB, which is obviously smaller than that of PMT devices.

4.3.5.2 Handheld probe

In order to mount 9 light source fibers and 4 detection fiber bundles, the handheld probe is designed to have a size of 8 cm by 6 cm (see Fig. 4-17). This size is comparatively larger for breast tissue examination especially for Southeast Asian women.

Meanwhile, the black paint on the hand-held surface can only absorb majority of the photons emitting out of the medium. However a minority amount of photons will reenter the medium, causing another reemission. This effect will degrade the quality of TPSF signals and consequently the image reconstruction accuracy with undermining the assumption of semi-infinite boundary condition in solving the forward model.

4.4 Comparison to conventional TD-DOTs

Table 4-14 compares and summarizes the pros and cons of this novel prototype TD-DOT technique and prototype system developed in this research with respect to conventional time-domain DOT designs (by 4 famous examples).

4.5 Summary

This chapter describes a novel TD-DOT technique and the implementation of prototype system. Key modules are described in detail technically. The prototype system has realized most desired favorable features, like fast data acquisition speed, sub-nanosecond temporal resolution, reflectance mode (reflectrometry) and relatively low system cost.

The prototype system can be configured further as a time-domain diffuse optical tomography system or a time-resolved spectroscopy system. Either is

ready for phantom-based imaging experiments and preclinical *in vivo* application.

Table 4-14 Comparison of novel TD-DOT technique with conventional TD-DOT technique

Features	Conventional TD-DOTs (by 4 famous examples)	This TD-DOT
Data acquisition speed	1. 25 images/s (~ 0.04 s/TPSF) [141]; 2. ~ 18.5-33.5s /TPSF using TCPSC & MCP-PMT [157]; 3. ~ 10 min to acquire 16 TPSFs using PMT (~ 37.5 s/TPSF) [149]; 4. ~ 30 min to acquire 64 TPSFs using PMT (~ 29 s/TPSF) [146];	~ 4.5 s to acquire 36 TPSFs (~ 0.5 s/TPSF); ~ 40x – 70x faster.
Complexity	1. Streak Camera: Moderate complexity; 2. – 4. TCSPC & MCP-PMT: High complexity;	Moderate complexity;
Cost	1. Extremely high cost of streak camera; 2. - 4. High cost of multi PMTs channels;	Low cost even for multi APD channels;
Temporal resolution	1. High temporal resolution; 2. - 4. Moderate temporal resolution;	Moderate temporal resolution using programmable digital delay line;
Dynamic range	1. Moderate dynamic range; 2. - 4. High dynamic range due to PMT;	Lower dynamic range due to APDs.

Chapter 5. Phantom experiments

This chapter describes the phantom-based diffuse optical tomography (DOT) imaging experiments using the fast TD-DOT prototype system described in Chapter 4. The first part in this chapter describes the study on solid and liquid phantoms. The second part derives the equations and algorithm, which are used to solve the forward model and the inversed problem in Laplace domain. The last part shows the experiment results from phantom experiments.

5.1 Design of tissue-like phantoms

Prior to preclinical application, all imaging systems must be tested and evaluated for their safety and accuracy. This procedure can be evaluated by using phantoms to simulate the real clinical conditions. A phantom refers to a mimicry created in laboratories which aims to approximate the properties of the tissue of interest. Usually the optical properties of phantoms are known and manipulated during fabrication.

For normal human breast tissue, it is possible to fabricate a standardized tissue-like phantom because the optical properties of human breast tissue have a good consistency, as proven in Table 2-1. The primary optical properties of interest are absorption coefficient μ_a and the reduced scattering coefficient μ_S'. Their values, for normal breasts, are found to be $\mu_s' = 9 \pm 2$ cm^{-1} and $\mu_a = 0.04 \pm 0.01$ cm^{-1}. Tumors have found to be at least four-folder greater of absorption contrast with a lower scattering contrast. These factors will guide

the phantom fabrications, instrument calibration and assessments of the image reconstruction results throughout this research [136, 178-183].

It would be advantageous to use ingredients with primarily absorption contrast (e.g. blood, ink) and with primarily scattering contrast (e.g. Intralipid, Lipofundin and titanium dioxide) to fabricate the *tissue*-like and *tumor*-like phantom phantoms. There are a couple of fabrication methods and recipes available so far [136, 178, 179, 181, 183]. In general, phantoms can be classified into five different categories: solid resin, liquid, gelatin, semisolid, and those using excised tissue. In this study, only solid resin and liquid phantom are fabricated.

5.1.1 Solid resin phantoms

Solid phantoms were fabricated to mimic the optical properties (μ_a and μ_s') of normal breast tissues in this research. The optical properties of the tissue-like phantom would be approximately of $\mu_s' = 6 \pm 1$ cm^{-1} and $\mu_a = 0.02 \pm 0.01$ cm^{-1}. The optical properties of the tumor-like phantom would be around $\mu_s' = 6 \pm 1$ cm^{-1} and $\mu_a = 0.06 \pm 0.01$ cm^{-1}.

5.1.1.1 Materials and optical properties

The constituents of the solid resin phantom contain epoxy-resin, hardener, Indian ink and titanium dioxides (TiO_2). The fabrication procedure is similar to the one described by Hebden [136]. These solid phantoms are permanent and can be machined (shaped and drilled) using standard machining equipments. Titanium dioxide (powder, 99.8%) (Sigma-Aldrich) serves as the scatterers due to its high refractive index (n = 2.7) over the surrounding epoxy medium. The scatter-free India ink (Pelikan Drawing Ink A 17 Black, Hanover,

Germany) serves as NIR wavelength absorber. Scatter-free epoxy-resin (n = 1.46) and resin hardener (n = 1.48) from commercially available products (Epicote 1006 system, mixing by weight ratio 10:6, Wee Tee Tong Chemicals Pte Ltd Singapore) with low absorption (μ_a = 0.025 cm^{-1}) properties serves as the solvent. The fabrication procedure is detailed in Appendix A.4.

5.1.1.2 Fabrication

All of the tissue-like solid resin phantoms are machined into slices disc (Fig. 5-1) with a diameter of 85 mm and a thickness of 5 mm. Holes are perpendicularly drilled on several slices at different positions. The diameter of holes is 7 mm. The tumor-like phantom also has a cylindrical shape but in a smaller size. The diameter is 7 mm and the thickness is 5 mm so that they can be inserted into the holes on the tissue-like phantoms without air gaps.

Fig. 5-1 (*Left)* Phantom discs with holes at different positions. (*Center*) Tumor-like phantom. (*Right*) Dimensions of the optical phantom.

5.1.2 Liquid phantom

5.1.2.1 Materials

The liquid phantoms were prepared using Lipofundin emulsion and distilled water. Fig. 5-2 shows the commercially available Lipofundin emulsion product (Lipofundin MCT/LCT 20%, B.Braun Melsungen AG, Germany) [184]. The water for lipofundin dilution is cool distilled water. The concentration of the lipofundion is 0.6% v/v.

Fig. 5-2 Lipofundin emulsion.

5.1.2.2 Optical properties

For 785 nm and 808 nm lasers, the μ_a and μ_s' of the liquid phantom are dominated by water and Lipofundin, respectively. At room temperature (25 ^oC), the absorption coefficient of water is 0.0252 cm^{-1} at 785 nm and 0.0212 cm^{-1} at 808 nm, respectively. The absorption contributed from Lipofundin emulsion is negligible. The scattering property is dominated by scattering properties of Lipofundin. In order to estimate its scattering property, the Mie theory was used to calculate the intrinsic μ_s' of Lipofundin solution. The calculation procedure can be found in Appendix A.4. The results show the reduced scattering coefficient μ_s' of 0.6% Lipofundin liquid phantom is approximately of 6.7 cm^{-1}.

5.2 Diffuse optical spectroscopy experiments

This part describes the theories which are used for image reconstruction in the DOT system. In order to achieve fast imaging performance, the derivations of forward and inversed problems were converted from time-domain to Laplace domain.

The entire image reconstruction procedure can be divided into two steps. The first step aims to figure out the system coupling coefficients of each fiber-to-

APD channel, with respect to the system impulse response (SIR) signals. Step two aims to acquire the background signals from homogeneous medium and the signals from the heterogeneous medium. The spatial heterogeneities distribution was inferred by using the perturbation theory. A couple of 2.5-D images were reconstructed at last using the pseudo-inverse image reconstruction technique.

5.2.1 Reconstruction of optical properties

As mentioned in section 3.2, the time-resolved diffuse optical measurements using a short pulse laser can be equivalently converted to frequency-domain. Although the information in frequency-domain technique is limited by spectra, its solutions to the diffusion equation are more time-efficient in solving the absorption and scattering properties.

Therefore in this TD-DOT system, we borrow idea from frequency-domain DOT techniques to get a fast image reconstruction speed.

5.2.1.1 Fitting method for background μ_a and μ_s'

The time-domain diffusion equation, Eq. (3-1) has a transmitted form in Laplace domain as

$$\left[\nabla^2 - k^2(p)\right] \cdot \varphi(p) = \frac{C_s C_d}{4\pi D} \cdot S(p) \tag{5-1}$$

where

$$\varphi(p) = \int_0^{+\infty} \varphi(t) \cdot e^{-pt}\, dt \tag{5-2}$$

Here p is the Laplace transformation parameter, C_s and C_d are channel specific constants which relate to the source intensity and the detector gains,

respectively. $S(p)$ is the system impulse response (SIR) in Laplace domain. k is the wave number, which is defined by

$$k^2(p) = \frac{\mu_a + p/c}{D} \tag{5-3}$$

For a reflective probing scheme, the semi-infinite boundary condition is adopted. And the corresponding analytical solution to the diffusion equation is:

$$\varphi(p) = \frac{C_s C_d S(p)}{4\pi D}\left(\frac{e^{-kr}}{r} - \frac{e^{-kr'}}{r'}\right) \tag{5-4}$$

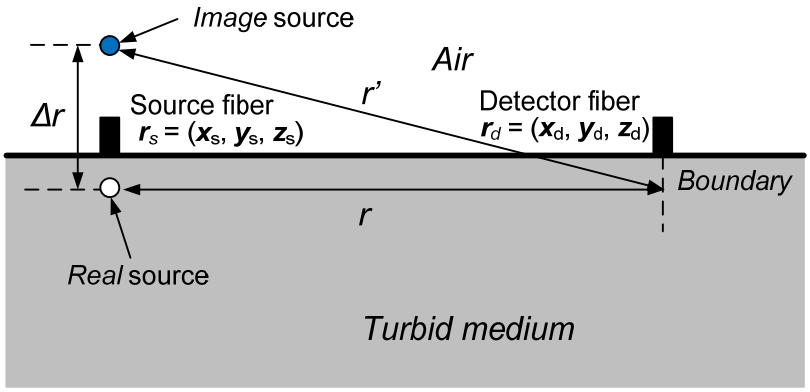

Fig. 5-3 Semi-infinite boundary condition for solving the forward problem.

From Fig. 5-3, we have

$$r' = \sqrt{r^2 + (\Delta r)^2} = r\sqrt{1 + \left(\frac{\Delta r}{r}\right)^2} \tag{5-5}$$

$$\approx r\left[1 + \frac{1}{2}\cdot\left(\frac{\Delta r}{r}\right)^2\right] = r + \frac{(\Delta r)^2}{2r} = r + \delta r \tag{5-6}$$

where

$$\delta r = \frac{(\Delta r)^2}{2r} \tag{5-7}$$

For an absorbing boundary,

$$\Delta r \approx 3.4 l_{tr} = 10.2 D \tag{5-8}$$

If neglecting higher order terms in Δr, Eq. (5-4) can be rewritten as

$$\varphi(p,r) = \frac{C_s C_d S(p)}{4\pi D}\left(\frac{e^{-kr}}{r} - \frac{e^{-kr'}}{r'}\right) \tag{5-9}$$

$$= \frac{C_s C_d S(p)}{4\pi D} \cdot \frac{e^{-k(p)r}}{r}\left(\frac{1}{2r^2} - k(p)\frac{1}{2r}\right) \cdot (\Delta r)^2 \tag{5-10}$$

$$= \frac{C_s C_d S(p)(\Delta r)^2}{8\pi D r^3} \cdot \left[1 + k(p)r\right] \cdot e^{-k(p)r} \tag{5-11}$$

Guessing the initial values of μ_{a0}, μ_0' and D_0, then

$$k_0(p) = \sqrt{\frac{\mu_{a0} + p/c}{D_0}} \tag{5-12}$$

and

$$k^2 = (k_0 + \delta k)^2 = k_0^2 + 2k_0 \cdot \delta k + \delta k^2 \approx k_0^2 + 2k_0 \cdot \delta k \tag{5-13}$$

$$k = k_0 + \delta k = \sqrt{\frac{\mu_{a0} + \delta\mu_a + p/c}{D_0 + \delta D}} \tag{5-14}$$

$$\delta k = \frac{1}{2k_0}\left(k^2 - k_0^2\right) \approx k_0\left(-\frac{\delta D}{2D_0} + \frac{\delta\mu_a}{2(\mu_{a0} + p/c)}\right) \tag{5-15}$$

Taking logarithm on both sides in Eq.(5-11) yields,

$$\ln\varphi(p,r) = \ln\frac{C_s C_d (\Delta r)^2}{8\pi D r^3} + \ln(1 + k(p)r) - kr \tag{5-16}$$

where

$$\ln\left[1 + k(p)r\right] = \ln(1 + k_0 r + \delta k \cdot r) \tag{5-17}$$

$$= \ln\left[(1 + k_0 r) \cdot \left(1 + \frac{\delta k \cdot r}{1 + k_0 r}\right)\right] \tag{5-18}$$

$$= \ln(1 + k_0 r) + \ln\left(1 + \frac{\delta k \cdot r}{1 + k_0 r}\right) \tag{5-19}$$

where

$$\ln\left(1+\frac{\delta k\cdot r}{1+k_0 r}\right)\approx\frac{\delta k\cdot r}{1+k_0 r}=\frac{rk_0}{1+k_0 r}\left(\frac{\delta D}{2D_0}+\frac{\delta\mu_a}{2\left(\mu_{a0}+\frac{p}{c}\right)}\right) \tag{5-20}$$

Substituting Eqs.(5-18), (5-19),(5-20) into Eq.(5-17) yields,

$$\ln\varphi(p,r)=\ln\frac{C_s C_d(\Delta r)^2}{8\pi Dr^3}+\ln(1+k_0 r)-k_0 r$$

$$+\frac{k_0 r}{2(1+k_0 r)}\left(\frac{\delta\mu_a}{\mu_{a0}+\frac{p}{c}}-\frac{\delta D}{D_0}\right)-\left(\frac{\delta\mu_a}{2\left(\mu_a+\frac{p}{c}\right)}-\frac{\delta D}{2D_0}\right)k_0 r \tag{5-21}$$

Rearranging Eq.(5-21) we have

$$\ln S(p)+\ln(1+k_0 r)-k_0 r-\ln\varphi(p,r)+\ln\frac{(\Delta r)^2}{8\pi Dr^3}=$$

$$-\ln(C_s C_d)+\frac{k_0 r}{2D_0}\left(\frac{1}{1+k_0 r}-1\right)\cdot\delta D+\frac{k_0 r}{2(\mu_{a0}+\frac{p}{c})}\left(1-\frac{1_a}{1+k_0 r}\right)\cdot\delta\mu_a \tag{5-22}$$

The coefficients of system coupling factor $\Delta\phi(f)$ is -1.

The coefficients for δD is defined as C_D, which equals to

$$C_D(p)=\frac{k_0 r}{2D_0}\left(\frac{1}{1+k_0 r}-1\right) \tag{5-23}$$

The coefficients for $\delta\mu_a$ is defined as C_μ, which equals to

$$C_\mu(p)=\frac{k_0 r}{2(\mu_{a0}+p/c)}\left(-\frac{1}{1+k_0 r}+1\right) \tag{5-24}$$

Choosing a set of Laplace parameters p_1, p_2, $p_3\ldots p_n$, we can have a set of linear equations in terms of $\ln(C_s C_d)$, δD and $\delta\mu_a$. Solving the equations we can obtain parameters $C_s C_d$, δD and $\delta\mu_a$ simultaneously.

The corresponding matrix form is

$$\begin{bmatrix} -1 & C_D(p_1) & C_\mu(p_1) \\ -1 & C_D(p_2) & C_\mu(p_2) \\ \vdots & \vdots & \vdots \\ -1 & C_D(p_n) & C_\mu(p_n) \end{bmatrix} \cdot \begin{bmatrix} \ln(C_s C_d) \\ \delta D \\ \delta\mu_a \end{bmatrix} = \begin{bmatrix} \varphi(r_s, r_d, p_1) \\ \varphi(r_s, r_d, p_2) \\ \vdots \\ \varphi(r_s, r_d, p_n) \end{bmatrix} \quad (5\text{-}25)$$

5.2.1.2 Fitting procedures

The fitting procedure is illustrated in Fig. 5-4. The procedure is followed by:

Step 1. Fitting program starts with initial values $(C_s C_d)^0$, μ_a^0 and $\mu_s'^0$;

Step 2. Calculating the parameters $(C_s C_d)$, μ_a and μ_s';

Step 3. Determine if the fitted absorption coefficients μ_a has sufficiently converged by judging if the difference is less than the acceptance threshold α.

Step 4. Determine whether the fitting procedure of the reduced scattering coefficients μ_s' has converged sufficiently by judging whether the difference is less than the acceptance criteria β;

Step 5. If requirements in step 4 or step 5 are fulfilled, the fitting iterations will terminate and the fitted parameters $(C_s C_d)$, μ_a and μ_s' are regarded as the true value of the background and the system coupling parameters. Else the calculated values of μ_a and μ_s' are replaced by the initial values $(C_s C_d)^0$, μ_a^0 and $\mu_s'^0$ until the fitting is converged.

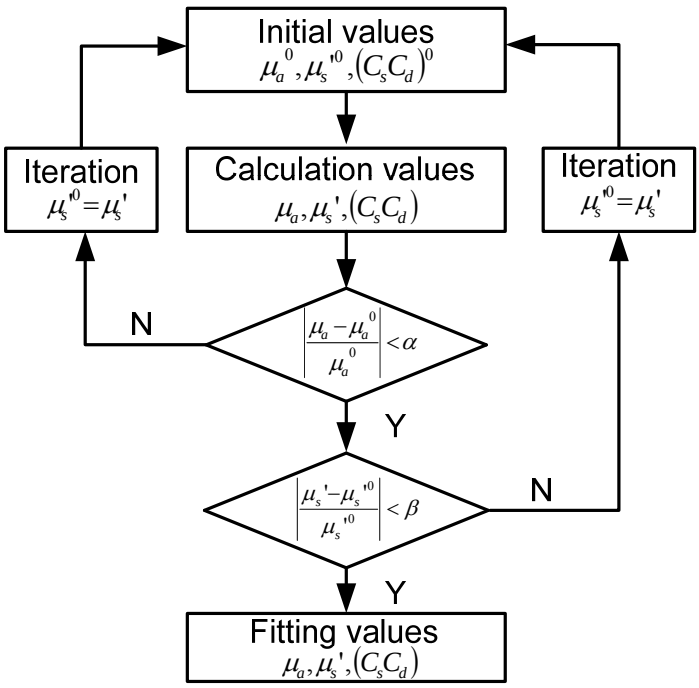

Fig. 5-4 Flow chart of optical parameters fitting.

5.2.1.3 Evaluation of fitting accuracy

To evaluate whether the designed fitting performance is qualified for the fast TD-DOT system, liquid phantom experiments were conducted and assessed. The experiment setup is as same as Fig. 4-29. The concentration of Lipofundin is 0.6%. The optical properties are absorption coefficient $\mu_a \approx 0.0252$ cm^{-1} and reduced scattering coefficient $\mu_s' \approx 6.0$ cm^{-1} for 785 nm. The overall liquid phantom has a volume of 17 cm (length) × 15 cm (width) × 10 cm (depth), which can be regarded as a semi-infinite boundary if the handheld probe is placed on the top surface.

Table 5-1 shows two fitting results with two sets of initial values (set I: $\mu_a^0 =$ 0.03 cm^{-1} and $\mu_s'^0 =$ 6.00 cm^{-1}. In set II: $\mu_a^0 =$ 0.05 cm^{-1} and $\mu_s'^0 =$ 8.00 cm^{-1}). These values are firstly selected from reasonable guessing. The fitting algorithm converges from two opposite convergence directions. The fitting goodness is evaluated as below.

The convergence criteria were selected to be $\alpha = 2 \times 10^{-5}$ and $\beta = 5 \times 10^{-6}$, respectively. Table 5-1 shows both initial values can converge to the desired values in several iteration steps (convergence objective: μ_a = 0.0252 cm^{-1} – absorption coefficients of water and μ_s' = 6.09 cm^{-1} - reduced scattering coefficients of Lipofundin solution). According to our observations, the fitting scheme shows a robust convergence performance for any given initial conditions and the fitting procedure can get to the desired value within tens of iterations. Meanwhile, the convergence speed is almost instantaneous. The convergence acceptance criteria, $\alpha = 2 \times 10^{-5}$ and $\beta = 5 \times 10^{-6}$, are picked to balance the fitting accuracy versus the converging speed. The results of fitting performance are plotted in Fig. 5-5. The Matlab code for fitting can be found in Appendix A.6.

Table 5-1 Convergence analysis of the fitting method

Set	Iterations	$C_s C_d$	μ_a (cm^{-1})	$\Delta\mu_a$ (Norm.)	μ_s' (cm^{-1})	$\Delta\mu_s'$ (Norm.)
I	start	-	0.03	-	6.00	-
	1	69.4932	0.0244	0.1859	6.0679	0.0113
	2	71.1275	0.0251	0.0259	6.0903	0.0037
	3	71.4042	0.0252	4.4666×10^{-3}	6.0907	6.417×10^{-5}
	terminate	71.4118	0.0252	3.4895×10^{-7}	6.0907	1.0971×10^{-7}
II	start	-	0.05	-	8.00	-
	1	71.6320	0.0160	0.6803	6.0556	0.2431
	2	68.1451	0.0230	0.04387	6.0044	0.0085
	3	70.2509	0.0251	0.0901	6.0873	0.0138
	4	71.3719	0.0252	0.0039	6.0907	5.5667×10^{-4}
	terminate	71.4118	0.0252	4.1971×10^{-6}	6.0907	1.1572×10^{-7}

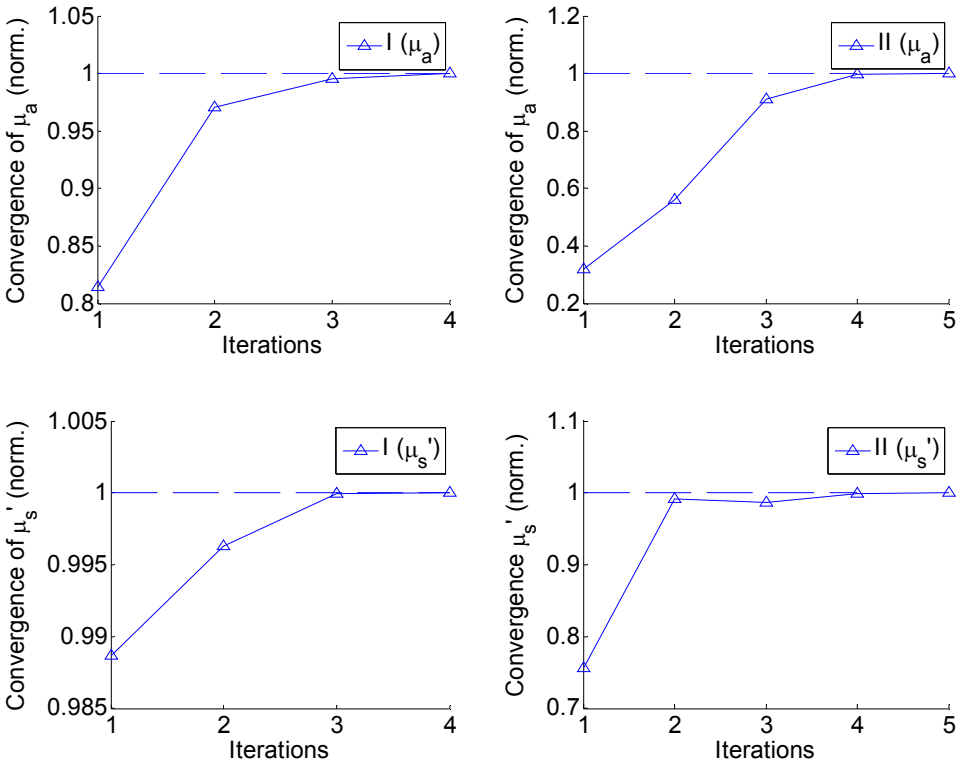

Fig. 5-5 Fitting μ_a and μ_s' by starting with two sets of arbitrary guesses.

5.3 Diffuse optical tomography experiments

5.3.1 Image reconstruction algorithm

The 2.5 dimensions images were reconstructed in this experiment. Showing in Fig. 5-6(A) are the image reconstruction structure in *x*-*z* plane. Three cross sectional planes along *y* direction are picked up to image the depth information. The step size in *y* direction is 2.5 mm, in sequence of y2, y0 to y1. In each *x*-*z* cross sectional plane, the absorption coefficient mapping is reconstructed.

The first step is to solve the reversed problem, in which the Jacobian matrix is built up in advance for the known spatial layout of light sources and detectors. For a voxel inside the tissue (see Fig. 5-6(B)), the distances to the real source

and image source are noted as r_{st} and r_{st}'. The distances to the real and image detectors are noted as r_{td} and r_{td}'. For the semi-infinite boundary condition, we have

$$\phi_{st} \approx \frac{1}{4\pi D r_{st}} \cdot \left(e^{-kr_{st}} - e^{-kr_{st}'}\right) \tag{5-26}$$

$$\phi_{td} \approx \frac{1}{4\pi D r_{td}} \cdot \left(e^{-kr_{td}} - e^{-kr_{td}'}\right) \tag{5-27}$$

Then the photon density from source to the detector via voxel V is

$$\phi_{sd} \approx \frac{1}{4\pi D r_{td}} \cdot \frac{1}{4\pi D r_{td}} \cdot \left(e^{-kr_{st}} - e^{-kr_{st}'}\right) \cdot \left(e^{-kr_{td}} - e^{-kr_{td}'}\right) \tag{5-28}$$

Meanwhile, the photon density from source to the detector directly, as showing in Fig. 5-6 (C) is

$$\phi_{sd}' = \frac{1}{4\pi D r_{sd}} \cdot \left(e^{-kr_{sd}} - e^{-kr_{sd}'}\right) \tag{5-29}$$

where r_{sd} and r_{sd}' are distances from real and image light sources to the detector.

Thus the normalized Jacobian matrix can be rewriteen as

$$J\left(x_s, y_s, z_s; x_d, y_d, z_d; v_{x,y,z}\right) = \frac{\phi_{sd}\left(x_s, y_s, z_s; x_d, y_d, z_d; v_{x,y,z}\right)}{\phi_{sd}'\left(x_s, y_s, z_s; x_d, y_d, z_d\right)} \tag{5-30}$$

where $\left(x_s, y_s, z_s\right)$ and $\left(x_d, y_d, z_d\right)$ are the positions of the ligth source and detector. $v_{x,y,z}$ is the position of voxel V in the tissue.

Similarly, the normalized perturbation $\Delta\varphi_p^N$ resulting from the homogeneous measurements φ_h and the inhomogeneous measurements φ_i

$$\Delta\varphi_p^N = \frac{L(\varphi_i) - L(\varphi_h)}{L(\varphi_h)} = \frac{\sum_{i=1}^{N} \phi_i e^{-pT_i} \Delta t - \sum_{i=1}^{N} \phi_h e^{-pT_i} \Delta t}{\sum_{i=1}^{N} \phi_h e^{-pT_i} \Delta t} \tag{5-31}$$

where $L(\varphi_h)=\sum_{i=1}^{N}\phi_i e^{-pT_i}\Delta t$ represents the discrete Laplace transformation of the homogeneous measurements, $L(\varphi_i)=\sum_{i=1}^{N}\phi_h e^{-pT_i}\Delta t$ represents the discrete Laplace transofmraiton of the inhomogeneous measurements. N represents the sampling numbers. ϕ_h and ϕ_i represent homogeneous and heterogeneous measurements, respectively.

In order to reconstruct the tomography images, we substitute the perturbation Eq. (5-31) and the Jacobian matrix, Eq. (5-30) into Eq. (3-12), yielding,

$$\Delta\mu_a=\left[J^T\cdot J+\lambda I\right]^{-1}\cdot J^T\cdot\Delta\varphi_p^N \tag{5-32}$$

where the Tinkhonov regulator λ is optimized and the value is configured to be 0.2. $\Delta\mu_a$ represents the spatial distribution of the absorption coefficients. The inhomoegeneties $\Delta\mu_a$ is rearranged in the predefined volume and the image can be reconstructed.

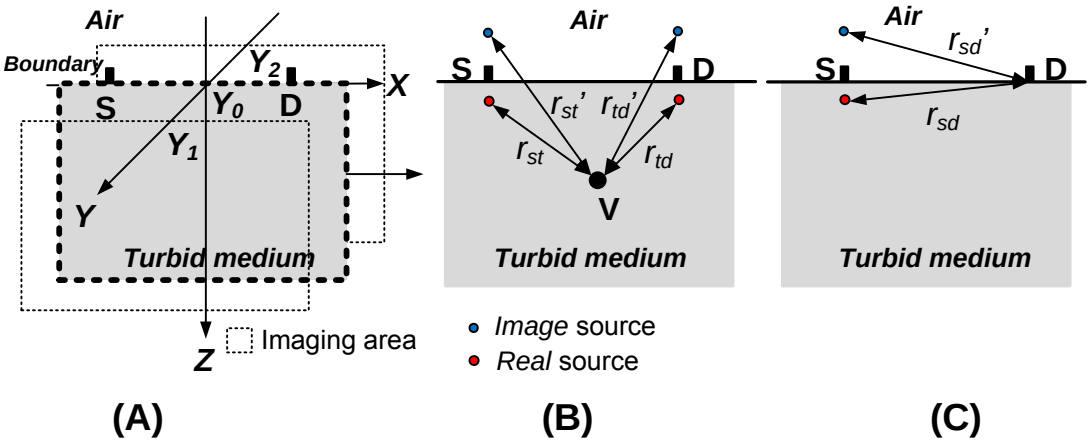

Fig. 5-6 Cross sectional imaging structure in semi-infinite medium. S: light source position. D: detector position. V: voxel position.

5.3.2 Data acquisition

To assess the image reconstruction performance of the fast TD-DOT prototype system, we conducted phantom experiments. The small cylindrical plastic

absorbers (diameter = 7 mm, length = 10 mm, $\mu_a \approx 0.06$ cm^{-1}, $\mu_s' \approx 6.0$ cm^{-1}) are use to mimic tumors (see Fig. 5-1). These tumor-like phantoms (target) were immersed in Lipofundin solution at depth of 2 cm. Their axial directions were parallel to the X-axis (positions P1 and P2 in Fig. 5-7). The handheld probe was placed on top surface of the solution as showing in Fig. 4-29. The TPSFs acquired from the liquid phantom with and without absorber immersed were regarded as homogeneous TPSF (φ_h) and heterogeneous TPSF (φ_i), respectively.

For 9 light source fibers and 4 detection fiber-bundles, each scan acquires 36 TPSFs. Fig. 5-8 plots a homogeneous TPSF with the corresponding heterogeneous TPSF acquired from the same channel. The distance from the source to the detector is 3.3 cm. The figure shows that the peak of the heterogeneous TPSF (φ_i) was attenuated by approximately of 5.9% from the homogeneous TPSF (φ_h). Meanwhile, the mean time-of-flight of photons was reduced by 28.57 ps after the absorber was immersed.

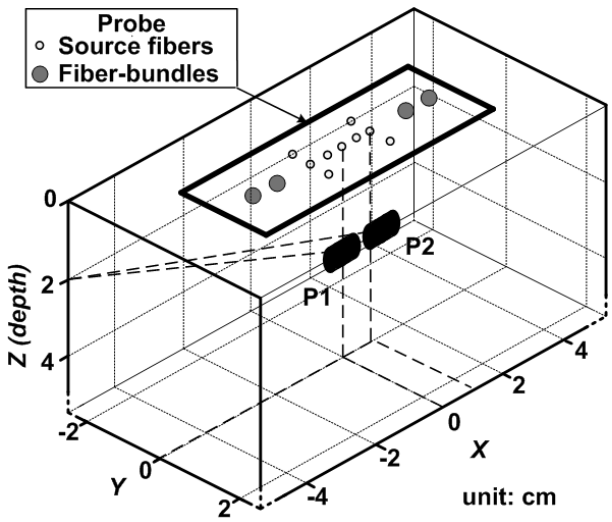

Fig. 5-7 Experimental setup for image reconstruction

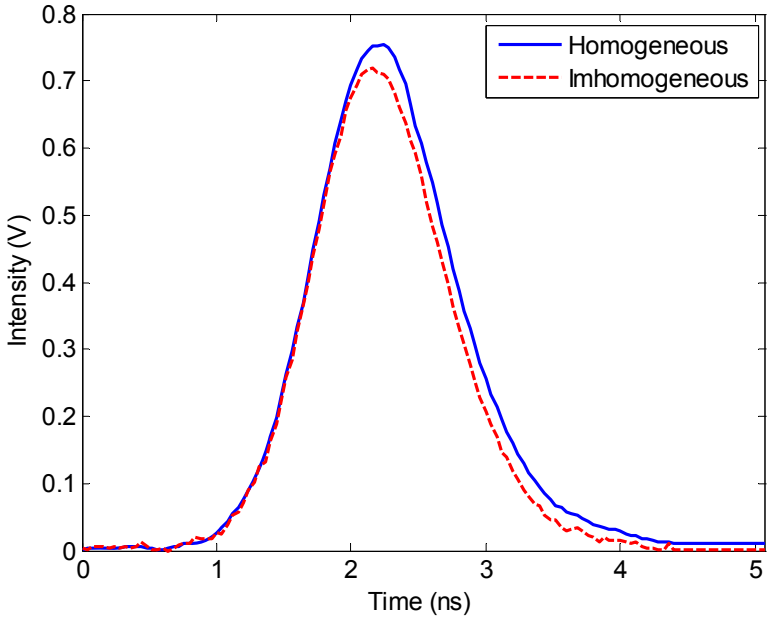

Fig. 5-8 TPSF acquired from homogeneous and inhomogeneous medium.

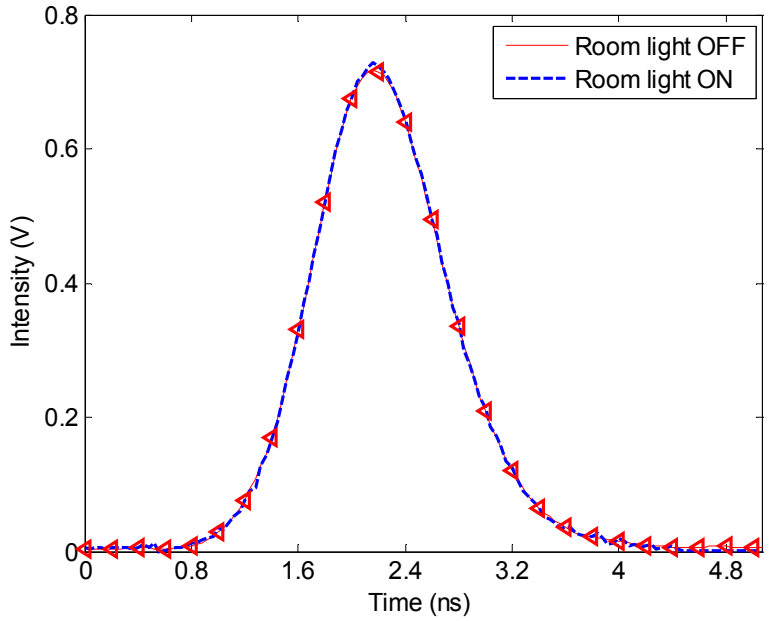

Fig. 5-9 TPSF measurements with room light on (blue line) and room light off (red circles).

From our experiment observations, our system has demonstrated a very attractive feature - the measurements insensitivity to the environmental illuminations. Fig. 5-9 demonstrates this feature by comparing two TPSFs acquired from room light on (dashed line) and off (triangle line). The root of

mean square of the noise has a voltage level approximately of 3.2 mV when room light is on while approximately of 2.7 mV when room light is off. The difference between two curves can be neglected. This feature is practically significant for clinical applications because it can greatly reduce patient's anxiety and improve the operation convenience.

5.3.3 Reconstructed images

After homogeneous and heterogeneous signals acquisition, the tomographic image can be reconstructed. The Matlab code shown in Appendix A.6 is used to reconstruct 2.5-D tomographic images. Fig. 5-10 illustrates the images of absorption coefficients. Each figure has a cross sectional area of 50 mm × 25 mm.

The target is placed at P1 and then P2 in the experiments (see Fig. 5-7). The depth remains to be 2 cm. Fig. 5-10(a-c) shows the image reconstruction results where the target is located at P1 and Fig. 5-10(d-f) shows the image reconstruction results where the target is horizontally moved to P2. From these image reconstruction results, we can rather accurately determine the target's position and size. For example, in Fig. 5-10(a-c), the recovered position of the absorber is ([x, y, z] = [0.013, 0, 1.918] cm), which is very close to the true position ([x, y, z] = [0, 0, 2] cm). In Fig. 5-10(d-f), the recovered position of the absorber is ([x,y,z] = [1.506, 0, 1.958] cm), which is also close to the true position ([x, y, z] = [1.5, 0, 2] cm). Table 5-2 shows the quantitative analysis of the reconstructed absorption coefficient. The mean $\overline{\mu}_a$ and standard deviation $\sigma(\mu_a)$ were calculated with the reconstructed distribution within the

true target region. It is evident that the reconstructed values are rather close to the true value.

The total image reconstruction took about 3-5 s using a PC with core 2 dual CPU at 1.8 GHz and 2 GB RAM. It is worthy to note that the handheld probe is right now optimized for 2.5-D cross-sectional image reconstruction. For real 3-D imaging in future, more TPSF signals from more the sources and detectors should be acquired.

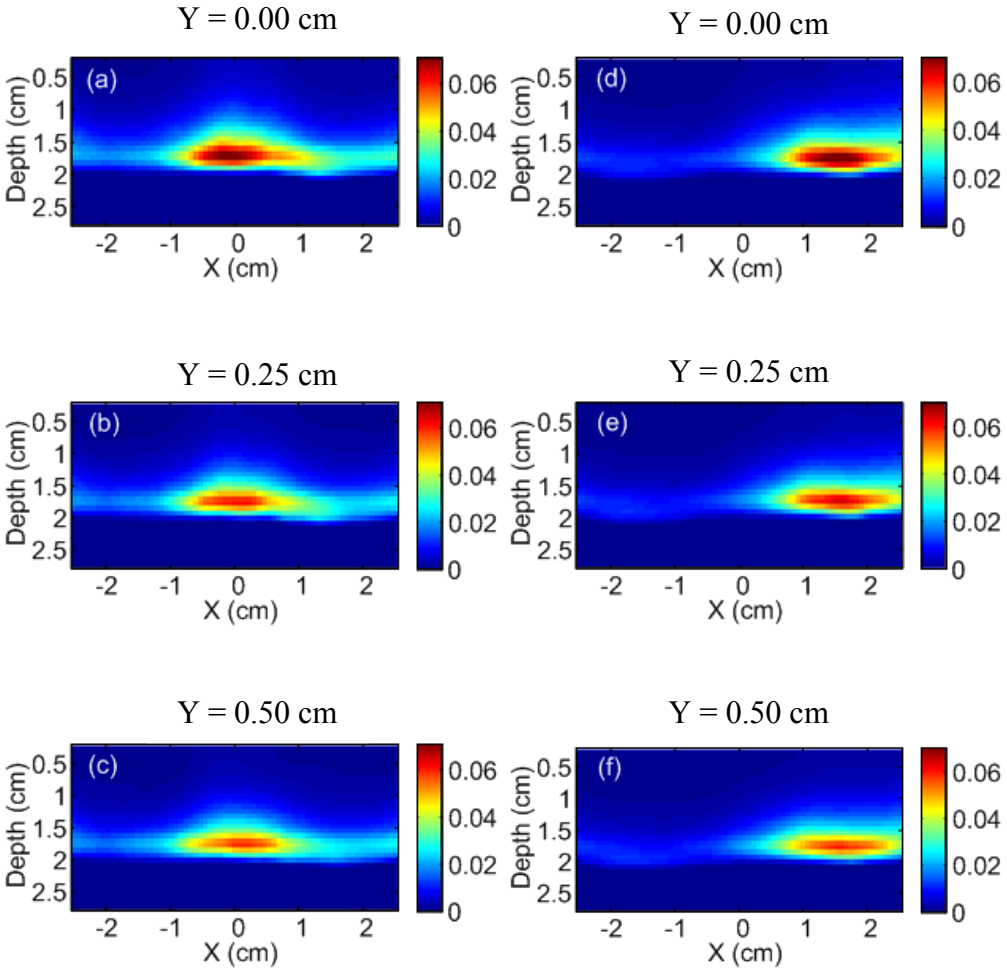

Fig. 5-10 Image reconstructions of absorption coefficient. (a-c) images for y = 0.00, 0.25 and 0.50 cm, respectively. Target (absorber) position is P1 = [0.0, 0.0, 2.0] cm. (d-f) images for y = 0.00, 0.25 and 0.50 cm, respectively. The target is horizontally 1.5 cm away from P1.

Table 5-2 Analysis of the reconstructed absorption coefficient μ_a.

	True value (cm^{-1})	Reconstructed value (cm^{-1})	
		Mean $\overline{\mu}_a$	Standard deviation $\sigma(\mu_a)$
Case 1 (P1)	0.06	0.0442	0.0198
Case 2 (P2)		0.0407	0.0140

5.4 Reliability improvement with a bias controller

As mentioned in section 4.3.4.3, bias controller was used to stabilize the modulation depth of MZM. In order to assess the corresponding improvements on image reliability after stabilizing the modulation depth of MZM, the same phantom-based experiment was repeated. The cylindrical absorber was placed at position $P(x, y, z)$ = (-1.0, 0.0, 1.5) cm. The cross-sectional images at y = 0.0 cm are reconstructed and shown in Fig. 5-11(A)-(D). Fig. 5-11(E) shows the bias voltages of MZM at which the TPSF signals for image (A)-(C) are acquired. Each two biases are separated by approximately $\Delta = V_\pi / 6$. Fig. 5-11(A) shows the image when the MZM biases at the 'quad+' point at system initialization stage. Fig. 5-11(B)-(C) shows image results after the bias of MZM drifts away from the 'quad+' point, respectively. Clearly, it is the bias-drift that cause the position (mass center) of the absorber in images gradually shifts leftward from its expected position. This effect degrades image quality and reproducibility. Meanwhile, undesirable image artifacts emerge at the right-hand side, which increases the risk of false-positive rates for target identification. Fig. 5-11(D) shows the image when the MZM is kept locking at the 'quad+' point after one hour brought by the bias controller. Comparing with image Fig. 5-11(A) at the starting stage, the target position (mass center) is almost unchanged and the artifacts do not appear. The image quality and reproducibility have been greatly improved.

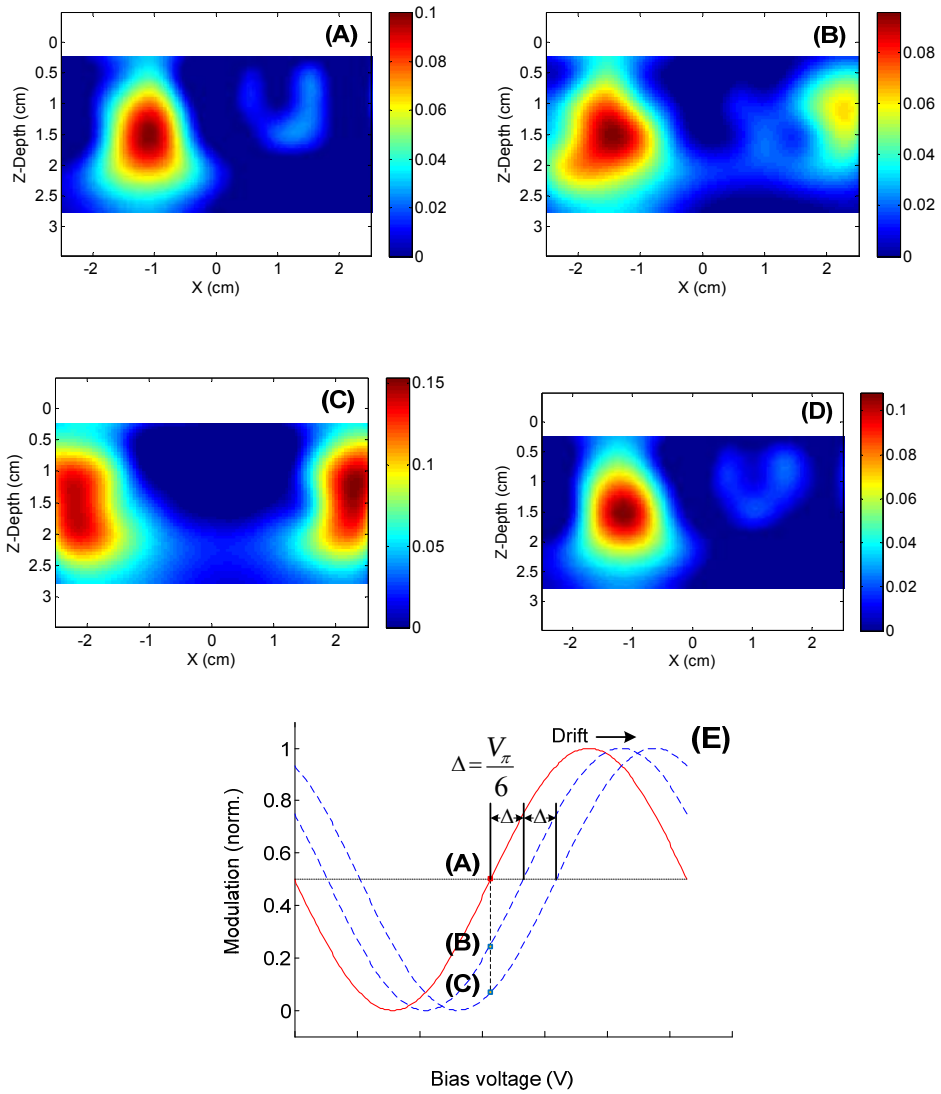

Fig. 5-11 Reliability improvement of image reconstruction results after using MZM bias controller. (A-C) w/o bias control; (D) w/ bias control. (E) MZM bias for image (A)-(C) are reconstructed, respectively.

5.5 Summary

This chapter describes in detail the fabrication of tissue phantoms as well as the phantom-based diffuse optical tomography imaging experiments. The image reconstruction results are assessed quantitatively. The heterogeneities of absorption coefficient can be spotted easily on imaging results. The bias voltage controller greatly improves the image reliability and repeatability.

In summary, the fast time-domain DOT prototype developed in this research has demonstrated a couple of advantageous features over the conventional time-domain DOT systems, including the high speed on TPSF acquisition and system SNR, relatively simple system structure and low cost have been realized. To expand these valuable advantages, we conducted preclinical experiments on normal human breast tissue *in vivo*. Details are reported in the next chapter.

Chapter 6. Optical and physiological characterizations of breast tissue *in-vivo*

This chapter describes the *in-vivo* preclinical experiments on human breast tissues by using the novel time-domain diffuse optical spectroscopy (DOS) prototype system.

In this study, two bundles of information are quantified from the time-resolved acquisitions. The first bundle is optical properties, especially the absorption coefficient (μ_a) and the reduced scattering coefficient (μ_s'). The second bundle is physiological parameters, specifically the concentration of oxyhemoglobin (HbO) and the concentration of deoxyhemoglobin (Hb), the total hemoglobin concentration (THC) and the oxygenation saturation (SO). In addition, this study analyzes the correlation of these two bundles of information with the physiological factors including menopausal states, ages and body mass index (BMI).

According to the *in vivo* experiment results, the optical properties of breast (especially the μ_a) and physiological parameters (THC and SO) varied significantly between premenopausal and postmenopausal women. Meanwhile, the experiment results also showed a conspicuous contrast in optical and physiological parameters between young (below 40-year-old) and old women (above 40-year-old). Quantitative analysis shows that there is a close correlation of optical/physiological parameters with the age, BMI and the menopausal states of women.

6.1 Human study protocols

6.1.1 Recruit of volunteers

A total number of 19 Singapore women subjects were recruited in this in vivo spectroscopy research. All subjects are healthy with no known breast diseases and any artificial implantations. The physical information of all subjects is shown in Table 6-1.

Table 6-1 Statistics of 19 women subjects

#	Age (y/o)	Height (m)	Weight (kg)	BMI	Menopausal
V1	50	1.65	75	27.5	Pre-
V2	48	1.57	53	21.5	Pre-
V3	50	1.63	54	20.3	Pre-
V4	23	1.64	58	21.6	Pre-
V5	41	1.65	68	25.0	Pre-
V6	45	1.56	49	20.1	Pre-
V7	23	1.60	49	19.1	Pre-
V8	49	1.51	57	24.9	Pre-
V9	23	1.58	47	18.8	Pre-
V10	47	1.65	56	20.6	Pre-
V11	49	1.47	43	19.9	Pre-
V12	26	1.60	52	20.3	Pre-
V13	26	1.68	68	24.1	Pre-
V14	50	1.62	80	30.6	Post-
V15	44	1.58	53	21.2	Post-
V16	43	1.64	55	20.4	Pre-
V17	51	1.61	64	24.7	Pre-
V18	50	1.59	54	21.4	Pre-
V19	49	1.59	63	24.9	Post-

These subjects were divided into groups by their menopausal states and age in research because aging and menopause states are strongly associated with the replacement of glandular tissue with fatty tissue [151]. As shown in Table 6-2, 3

postmenopausal (Post-) women age from 44, 49 to 50 years old. The rest 16 premenopausal (Pre-) women ages from 23 to 50 years. There are 5 women younger than 40 years old and 14 women are older than 40 years old. The youngest and oldest subjects were 23 and 50 years old, respectively. The average age of all subjects was 41.7 years old and the standard deviation (SD) was 11.1 years.

Table 6-2 Statistics of 19 volunteer women subjects.

	Age		Menopausal states	
	Young (< 40)	Old (≥ 40)	Pre-	Post-
Number of subjects	5	14	16	3
Mean (years)	24.2	47.9	40.8	47.0
SD (years)	1.6	2.8	11.4	2.6
Mean (years)		41.7		
SD (years)		11.1		

6.1.2 RBN approval

The *in-vivo* breast tissue experiments using time-resolved DOS instrument have been approved by Institute Review Board of National University of Singapore.

6.1.3 Pre-scanning preparations

1) Warm up system to stabilize the temperature of the APDs and the MZM. This procedure usually takes approximately 15-25 minutes.
2) Acquire system impulse response by placing a white diffusive paper at 18 cm away from the hand-held probe (see section 4.3.4).

3) System characterization by solving the system coupling coefficients (i.e. the parameters $C_s C_d^{785}$ and $C_s C_d^{808}$ at 785 nm and 808 nm, respectively).
4) System calibration: DOS system to be recalibrated before each scanning session to ensure accuracies before taking measurements, and every 30 minutes thereafter.
5) Operators A and B to be appropriately dressed in lab coat. Gloves should also be worn during the scan.
6) Comfortable chair to be provided to seat subject. The subjects keep sitting posture during data acquisition.
7) Probe surface to be sterilized with denatured alcohol using cotton balls before being used to contact subject.
8) Briefing instructions during experiments are conducted by operator to volunteer subjects. Consents from all volunteer subjects are obtained.

6.1.4 Probing positions

Subjects were probed in a sitting posture without any external compressions upon breast. The hand-held probe was placed on the left and right breasts sequentially. In order to keep the probe fully contact with the breast tissue, a slight pressure will be applied upon the breast. Because of the small effective area, the breasts shape would not change too much to be completely covered. This will not cause any discomfort to subjects. Meanwhile, the fiber tips and the fiber bundles mounted on the probe have been alighted in surface with the probing plane, the laser beam will go into the breast and the emission signals can be collected by fiber bundles without inducing gap reflections. Also, the

small breast shape deformation (normally 1-2 mm due to probe pressure) could be ignored safely comparing with the accuracy of tomography images and the detectable cancer/tumor size (~1.0 cm). For the spectroscopic application, which only cares about the optical properties and physiological parameters of whole breasts, the pressure effect could be completely ignored.

As shown in Fig. 6-1, the probing positions on each breast are 3, 6, 9, 12 o'clock. At each position, 72 TPSFs are acquired from 9 source fibers and 4 detectors for 2 wavelengths. Each scan takes approximately 5 seconds. In this period, the subject was asked to hold breath in order to minimize the breast fluctuation. To further minimize detrimental impact induced by heart beating and operator hand trembling, the scanning at each position repeated 5 times. Thus a total of time-resolved measurements contains $36 \times 2 \times 8 \times 5 = 2\,880$ TPSFs from each subject, which can be accomplished in 10 - 15 minutes.

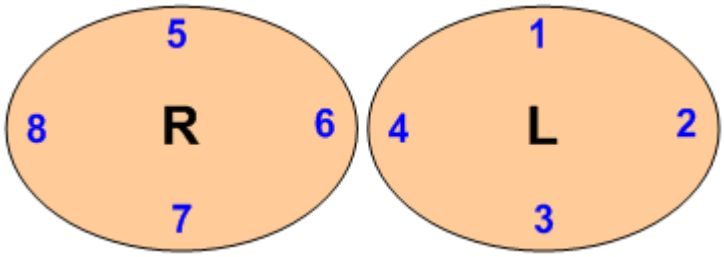

Fig. 6-1 Four probing positions on left (L) and right (R) breasts of each subject.

6.1.5 Scanning procedure and data acquisition

1) Subject will be asked to hold her breath each time when a reading is taken. There is a 3 seconds lapse thereafter, as the system switches from one laser to another, and during this period, the subject will be

able to take a breath (exhale and inhale). Two lasers at different wavelengths are used for each reading.

2) Operators will do a pre-scanning on each subject by placing the probe on locations 5, 6, 7, 8 (see Fig. 6-1) to simulate the actual locations during the scan. One reading is taken at position 5 and position 7, and 2 readings are taken at position 8. A total of 5 readings will be taken during the pre-scanning.

3) 40 sets of TPSF measurements will be taken per subject, 20 sets of TPSF measurements taken from each breast. The probe placed at 4 different locations on the breast (see Fig. 6-1). 5 measurements will be made at each location.

4) During scanning, operator B should monitor the values of the optical parameters calculated by the software from the data. It will be up to the discretion of operator to determine if more measurements should be taken if the data collected is not of a good quality. The experiment results will be automatically saved into data file for post-experiment analysis.

6.2 Spectroscopy data processing

The data processing procedure for spectroscopy is similar to the data processing procedure developed for the spectroscopic study (see section 5.2). The optical properties of the whole breast tissue are calculated from the time-resolved measurements. Instead, two wavelengths (785 nm and 808 nm) NIR laser were simultaneously utilized. In addition, few more physiological information data types are extracted from the resultant optical properties (μ_a

and μ_s'), including the concentration of the hemoglobin C_{HbO} , the concentration of the deoxyhemoglobin C_{HbO} , the total hemoglobin concentration THC , the oxygenation saturation of the blood SO. The calculation formula for these parameters can be found in Eq. (2-21) and Eq. (2-22).

The TPSF obtained from channel with source-to-detector separation of 2.35 cm (channel D3-S6 in Table A-3) was selected to calculate the optical properties (μ_a and μ_s'). This separation allows the incident photons to go into the breast tissue up to centimeters [23]. The μ_a, μ_s', THC and SO of each subject were calculated from 8 probing positions. The results data sets $R(i) = [\mu_a(i), \mu_s'(i), THC(i), SO(i)]$ $(i = 1 \ldots 8)$ of each subject were averaged in order to minimize the positional variations. Results were expressed by (mean value ± standard deviations). The Matlab code of TD-DOS can be found in Appendix A.7.

6.3 Spectroscopy results

Table 6-3 summarizes the optical properties and physiological parameters of all 19 subjects. The mean μ_a of 19 subjects was found to be 0.0503 cm^{-1} with a standard deviation of 0.0151 cm^{-1} at 785nm. At 808 nm, the values of μ_a were (0.0518 ± 0.0153) cm^{-1}. The reduced scattering coefficient showed similar results at two different wavelengths: at 785 nm showing (10.53 ± 1.19) cm^{-1} and at 808 nm showing (10.49 ± 1.17) cm^{-1}. The blood oxygenation saturation (SO) of all 19 subjects was found to be (64.8 ± 10.3) % while the total hemoglobin concentration (THC) was found to be (22.3 ± 7.5) μMol/L.

The *in vivo* optical spectroscopy on bulk breast has been investigated worldwide. However, there are a little bit differences between different research groups. The differences can be ascribed to the constitution difference of women subjects (ages, menopausal states, races and so on), different methodologies and apparatus, and the different laser wavelengths used. Table 6-4 compiles some recent *in vivo* research results on healthy breast tissue using different spectroscopy techniques. All data are rounded properly for comparison. Taking the Caucasian women as an example, Durduran *et al* reported the μ_a of (0.04 ± 0.03) cm^{-1} and μ_s' of (9 ± 2) cm^{-1} at 780 nm from experiments on 52 healthy women [26]. Results reported by Pogue *et al* showed a slight difference. The averaged μ_a and μ_s' were (0.05 ± 0.04) cm^{-1} and (10 ± 2) cm^{-1} respectively [31]. In addition to the difference on optical parameters, the physiological parameter results between each group are also slightly different. The average value of *SO* ranges from 61% to 77% and *THC* from 16 μMol/L to 34 μMol/L. So far there are very few reports published for Asian women. Suzuki reported that the average μ_a from 30 Japanese women was (0.05 ± 0.01) cm^{-1} and the average μ_s' was (9 ± 2) cm^{-1} [34]. In this study only Southeast Asian women were involved, the mean values of the optical properties and physiological parameters, as shown in Table 6-4, showed a good agreement with to the data of Caucasian women as well as other regional Asian women.

Table 6-3 Average optical properties and physiological parameters of 19 subjects.

	785 nm	808 nm
μ_a (cm^{-1})	0.0503 ± 0.0151	0.0518 ± 0.0153
μ_s' (cm^{-1})	10.53 ± 1.20	10.49 ± 1.19
SO (%)	64.8 ± 10.3	
THC (μMol/L)	22.3 ± 7.5	

Table 6-4 Comparison of optical/physiological parameters from this study and recent literatures. N refers to the number of subjects involved in different studies while μ_s' and μ_a are rounded properly for consistency.

	N	μ_s'(cm^{-1})	μ_a (cm^{-1})	*SO* (%)	*THC* (μMol/L)
Durduran [26]	52	9 ± 2	0.04 ± 0.03	68 ± 8	34 ± 9
Grosenick [27]	28	10 ± 2	0.04 ± 0.01	74 ± 3	17 ± 8
Tomas [28]	36	8 ± 2	0.04 ± 0.02	77 ± 8	17 ± 10
Spinelli [29]	>50	11 ± 2	0.04 ± 0.01	66 ± 9	16 ± 5
Taroni [30]	101	11 ± 1	0.05 ± 0.01	71 ± 8	20 ± 7
Pogue [31]	46	10 ± 2	0.05 ± 0.04	61 ± 1	22 ± 7
Poplack [32]	23	12 ± 2	0.05 ± 0.02	69 ± 9	24 ± 12
Suzuki [34] *	30	9 ± 1	0.05 ± 0.01	-	-
This study	19	10 ± 1	0.05 ± 0.02	65 ± 10	22 ± 8

*Data was obtained using wavelength at 753 nm

6.4 Correlation of parameters and demographic factors

To assess the performance on spectroscopy, the data result was analyzed with respect to the physiological factors, including the menopausal status, the age, and the body mass index (BMI).

6.4.1 Menopausal status

To explore the relationships between menopausal states and the optical/physiological parameters, 3 postmenopausal women and the 16 premenopausal women were examined, respectively.

6.4.1.1 Optical parameters

Fig. 6-2 (A) and (B) show scatter plots of data μ_s' versus μ_a from premenopausal women (in blue circles) and postmenopausal women (in red blocks) at two wavelengths, respectively. 2-dimensional error bars show the standard deviations on two optical parameters. It can be found that μ_s' and μ_a of postmenopausal women are generally smaller than that of premenopausal women, which show an agreement to the observations in literature [15]. Statistical results in Table 6-5 show that the averaged μ_a of premenopausal women was (0.0541 ± 0.0141) cm^{-1} at 785nm - approximately 60% larger than that of premenopausal women at (0.0338 ± 0.0044) cm^{-1}. At 808 nm, μ_a shows a similar trend of being larger in premenopausal women at (0.0557 ± 0.0141) cm^{-1} - and approximately 61% higher than that in postmenopausal women which was found to be (0.0347 ± 0.0041) cm^{-1} . The difference of μ_s' between 785 nm and 808 nm is not significant. At 785 nm, the μ_s' of premenopausal women were found to be (10.75 ± 1.17) cm^{-1} on average, which is approximately 12% larger than that of postmenopausal women at (9.6 ± 0.83) cm^{-1}. At 808 nm, the contrast is similar. The μ_s' of premenopausal women is about 12% larger than that of postmenopausal women.

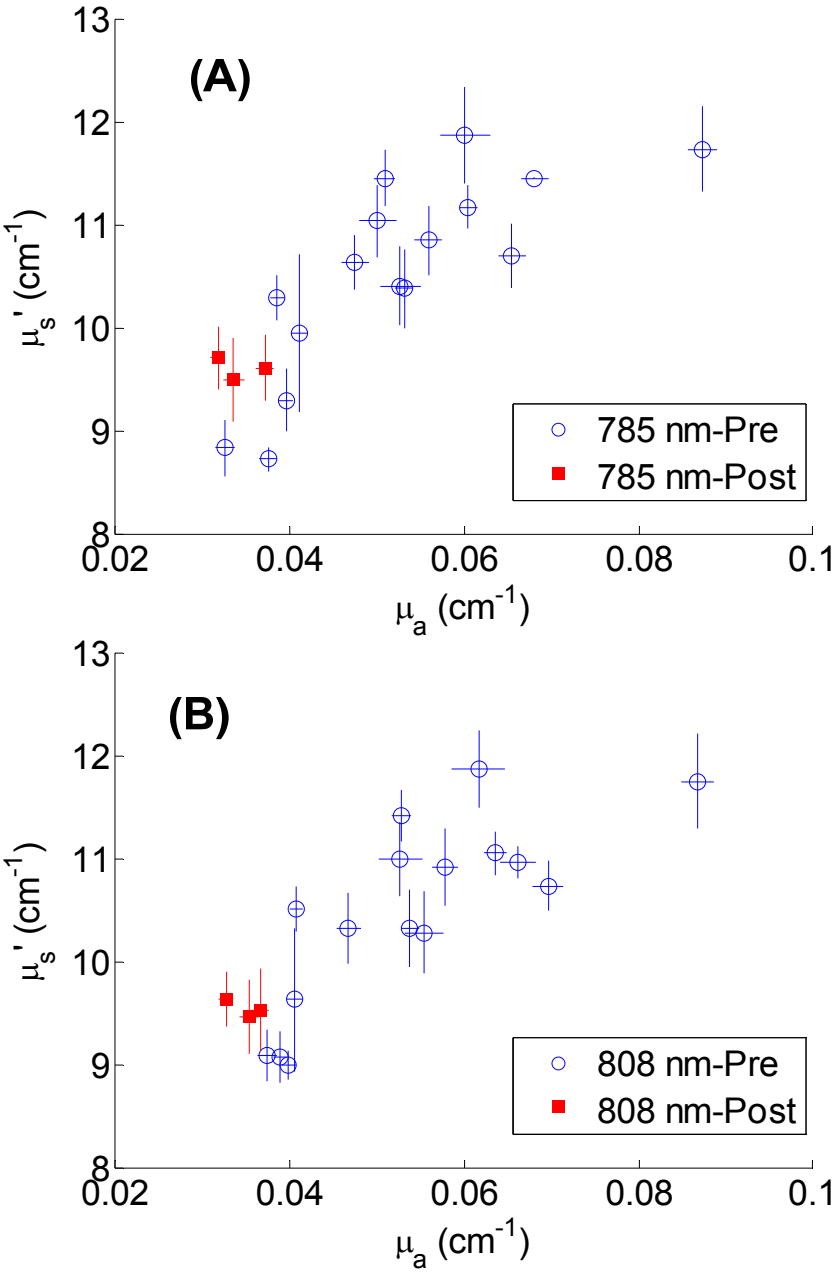

Fig. 6-2 Scatter plot of μ_s' versus μ_a of all subjects. (A): at 785 nm. (B): at 808 nm. Red blocks represent results of postmenopausal subjects. Blue circles represent the results of premenopausal subjects. 2-dimensional error bars are standard deviations of 8 probing positions of each subject.

6.4.1.2 Physiological parameters

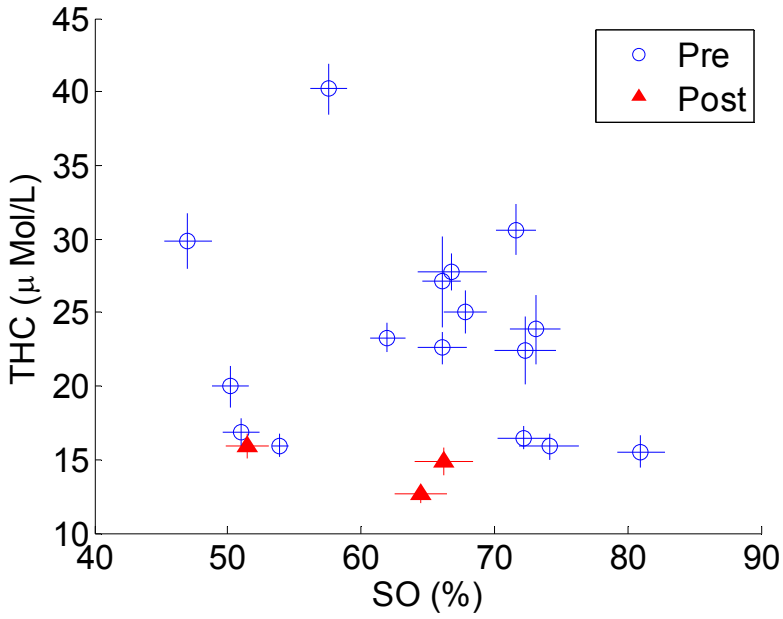

Fig. 6-3 Scatter plot of *THC* versus *SO* of all subjects. Red triangles represent results of postmenopausal subject. Blue circles represent results of premenopausal subject. 2-dimensional error bars represent standard deviation of 8 probing positions of each subject.

Table 6-5 Statistics of optical properties and physiological parameters of post- and pre-menopausal subjects

	Postmenopausal		Premenopausal	
	Mean	Std. Dev.	Mean	Std. Dev.
μ_a at 785nm (cm^{-1})	0.0338	0.0044	0.0541	0.0141
μ_a at 808nm (cm^{-1})	0.0347	0.0041	0.0557	0.0141
μ_s' at 785nm (cm^{-1})	9.60	0.83	10.75	1.17
μ_s' at 808nm (cm^{-1})	9.54	0.81	10.70	1.14
SO (%)	61.6	9.8	65.1	10.3
THC (μMol/L)	14.3	2.3	24.1	7.1

Fig. 6-3 shows a scatter plot of *THC* versus *SO*. It is clear that the *THC* of premenopausal women, in general, is higher than that of postmenopausal

women. Table 6-5 shows THC of the premenopausal group is (24.1 ± 7.1) μMol/L, which is approximately 69% larger than that of postmenopausal group which is (14.3 ± 2.3) μMol/L. The SO difference between the postmenopausal women and premenopausal women is not significant.

6.4.2 Age

In the past two decades, the American Cancer Society has been recommending annual mammograms and other intensive breast cancer examinations beginning at 40s and older for women with a moderate and high breast cancer risk. The starting annual mammograms for women with low breast cancer risk can be postponed to 50s and older [35]. So in this research, we picked 40 years old as the criteria to group the subjects for analyzing the relationship between age and optical/physiological alternations (see Table 6-6). The young women group has 5 women subjects, with ages of (24.2 ± 1.6) years old. The old women group has 14 women subjects, with ages of (47.9 ± 2.8) years old.

6.4.2.1 Optical parameters

Table 6-6 summarizes the averaged optical properties and physiological parameters in terms of age. Significant contrast between two groups can be found in absorption coefficient (μ_a) and total hemoglobin concentration (THC).

The μ_a of young women group at 785 nm was found to be (0.0617 ± 0.0143) cm^{-1}, which is approximately 38% larger than the old women group in which the averaged μ_a was found to be (0.0447 ± 0.0122) cm^{-1}. At 808 nm, the μ_a of young women group was found to be (0.0631 ± 0.1392) cm^{-1}, which is approximately 36% larger than that of aged women group at (0.0462 ± 0.1261)

cm^{-1}. The higher μ_a values associated with young women group may be explained by the greater content of fibroglandular tissue in the mammographically dense breasts. Fig. 6-4 shows a scatter plot of μ_a among young and old women group.

The difference of reduced scattering coefficients μ_s' between young women group and aged women group is not significant. Young women group shows an average μ_s' of (11.307 ± 1.010) cm^{-1} at 785 nm and (11.268 ± 0.987) cm^{-1} at 808 nm. Both are approximately 11% larger than that of old women group.

6.4.2.2 Physiological parameters

Table 6-6 also shows a difference on the physiological parameter of *THC*. The *THC* of young women group was found to be (27.9 ± 7.0) μMol/L while the *THC* of aged women group was (19.6 ± 6.1) μMol/L. The former group is approximately 42% larger than the latter group. Fig. 6-5 shows a scatter plot of *THC* versus the age of subjects in groups of young and old. For easy comparison, data of young women group are shown in red triangles and data of aged women group are plotted in blue circles. Error bar shows the standard deviation on corresponding parameters.

The parameter of *SO* between young women group and aged women group is (63.8 ± 7.6) % versus (64.7 ± 11.4) %. Values are almost the same.

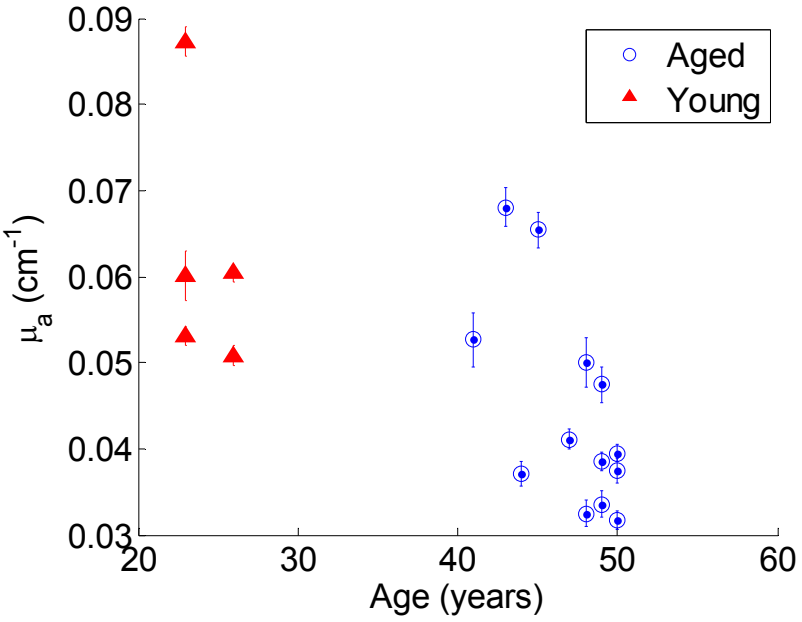

Fig. 6-4 Scatter plot of μ_a versus ages of 19 subjects. Red triangles represent results of young subject group while blue circles represent results of aged subject group. Error bars represent standard deviation of μ_a.

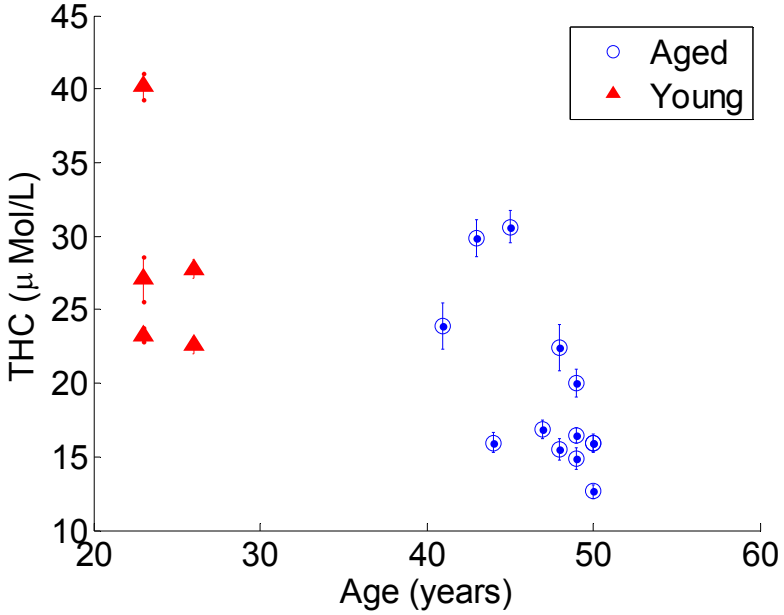

Fig. 6-5 Scatter plot of parameter THC versus ages of 19 subjects. Red triangles represent results of young subject group while blue circles represent results of aged subject group. Error bars represent standard deviation of THC.

Table 6-6 Mean and standard deviation of optical properties and physiological parameters of 19 subjects

	Old (age > 40)		Young (age < 40)	
	Mean	Std.dev.	Mean	Std.dev.
μ_a at 785 nm (cm^{-1})	0.0447	0.0122	0.0617	0.0143
μ_a at 808 nm (cm^{-1})	0.0462	0.1261	0.0631	0.1392
μ_s' at 785 nm (cm^{-1})	10.154	1.103	11.307	1.010
μ_s' at 808 nm (cm^{-1})	10.108	1.077	11.268	0.987
SO (%)	64.7	11.4	63.8	7.6
THC (μMol/L)	19.6	6.1	27.9	7.0

6.4.3 Correlation analysis

In order to examine the correlation between the optical/physiological parameters and women's age, menopausal states and BMI, the correlation analysis using Pearson's correlation coefficients was conducted. The Pearson's correlation coefficient is defined by [185]

$$r = \frac{N\sum_{i=1}^{N} x_i y_i - \sum_{i=1}^{N} x_i \sum_{i=1}^{N} y_i}{\sqrt{\left(N\sum_{i=1}^{N} x_i^2 - \left(\sum_{i=1}^{N} x_i\right)^2\right)\cdot\left(N\sum_{i=1}^{N} y_i^2 - \left(\sum_{i=1}^{N} y_i\right)^2\right)}} \quad (6\text{-}1)$$

where N represent the sampling number. x_i and y_i represent variable and the dependent variable respectively. r represents the correlation results. For menopausal women, the dependent parameter was chosen as 1. For premenopausal women, the dependent parameter was chose as 0.

The correlation analysis using Pearson's correlation coefficients are shown in Table 6-7, the high correlation coefficients shows that the optical properties of μ_a and μ_s' are closely correlated with age, BMI and menopausal status of subject in sequence from high to low. Physiological parameter THC shows

similar close correlation on women's age, BMI and menopausal as well. The correlation to the parameter SO is not significant.

Table 6-7 Pearson's correlation coefficient between optical, physiological parameters and subjects' parameters

	μ_a	μ_s'	SO	THC
Age	-0.6245 [a]	-0.6590 [a]	0.0609 [c]	-0.6294 [a]
BMI	-0.5059 [b]	-0.5245 [b]	0.2427 [c]	-0.5097 [b]
Menopausal states *	-0.4883 [b]	-0.3836 [c]	-0.1485 [c]	-0.4720 [b]

[a] $p < 0.005$; [b] $p < 0.05$; [c] $p < 0.1$;

* 0 for premenopausal women; 1 for postmenopausal women.

6.5 Conclusions

In conclusion, the *in-vivo* spectroscopy functionality of time-domain diffuse optical imaging system has been evaluated. The optical properties and physiological parameters of breast tissues from 19 healthy Singapore women subjects were characterized for the first time. The preliminary experiments results shows a close correlation of optical properties (μ_a and μ_s') and physiological parameters (THC) with age, menopausal states and BMI. Although experiments on a larger series of subjects are highly desired to statistically evaluate the optical properties and physiological parameters in near future, the results presented above still could serve as a rough reference for diseased breast tissue study in near future.

Chapter 7. Summary and future prospects

This final chapter summarizes the state of this research project at present and the likely future prospects in next research stage. Feasible design features for next generation device and the prospects for clinical applications are discussed.

7.1 Summary

This thesis has explored a novel spread spectrum time-domain diffuse optical tomography technique. The prototype system was established. A 2.488-Gbps PRBS was used to modulate the dual near-infrared light. The encoded near-infrared light passed through the phantom or human breast tissue *in-vivo*, the reflectance light was correlated with the reference PRBS. The information of time-of-flight of photon, i.e. the temporal point spread function were acquired. The diffusion equation was used to approximate the model the photon propagation in the turbid medium. The semi-infinite boundary conditions were used to solve the forward problem. The system calibration was conducted prior to the imaging and spectroscopy experiments. The optical properties, especially the absorption coefficient μ_a and the reduced scattering coefficient μ_s' were calculated in the Laplace domain. 2.5-D tomographic images were reconstructed using the pseudo-inverse technique.

This novel TD-DOT/DOS instrument has achieved most desired objectives:

- Fast data acquisition speed: the total time for time-resolved data acquisition, system calibration, imaging reconstruction and

spectroscopic analysis has been greatly reduced down to a few seconds.

- Compactness: this instrument employs two near-infrared laser diodes as the light sources. Meanwhile, it employs 4 avalanche photodiodes as the detectors. This instrument architecture was straightforward and pretty compact including to the peripheral supporting devices and components.
- Low cost: laser diodes and avalanche photodiodes used in the instrument are of low cost, which greatly reduce the overall system cost. Compared to the conventional TD_DOT instruments, in which multichannel of ultrashort pulse laser and single photon counting devices were used, this instrument cost is only up to ten thousand US dollars, approximately 10% cost of the conventional instrument setups.

In addition, the preliminary *in-vivo* experiments on the healthy women subjects were conducted to characterize the breast tissue's optical properties and physiological parameters. Pronounced correlation between optical properties, physiological parameter and the demographic factors were analyzed and established.

7.2 Future prospects

7.2.1 Improvement of system performance

Although this prototype TD-DOT/DOS system has achieved most desired objectives, there are still some limitations, which deserve further improvement and optimization before finalization.

- Noise level

To obtained high quality image reconstruction and spectroscopic results, the time-resolved data should possess a good enough signal-to-noise ratio (SNR) and a sufficient dynamic range. The prototype system right away can only offer a medium range of SNR up to 56 dB and a best image resolution about 1 cm. Although these features are good enough for detection stage I tumor-like heterogeneities at depth of 2-3 centimeters, there is still a lot of rooms for us to increase the detection depth if we can decrease the noise level. The noise showing in the detection signals primarily come from the PRBS cross-correlation (see section 4.3.2), which can be possibly reduced with a more sophisticated circuit and more optimal PCB layout design. Increasing the dynamic range of the signal measurements is another feasible way to improve the system SNR. For a straightforward example, we can replace the linear Op-Amp in the signal amplification circuit (see Fig. 4-11) with non-linear amplification (e.g. using exponential amplifiers) so that we can get an significantly enlarged signal measurement range.

- System expand

The prototype system at present has 9 light sources and 4 detection fiber bundles for TPSF acquisition. These system configurations are still not able to offer high quality imaging performance for large area applications. Increasing light sources and detectors can increase not only the detection area in one-time scanning but also the resolution of the image. We plan to increase the light sources from 9 to 36 and the detectors from 4 to 16 soon. The light source expansion can be easily

realized by cascading a 1 × 4 optical fiber switch component between the MZM and the 1 × 9 optical fiber switch. The expansion of the detection channels can also be easily realized by duplicating 16 avalanche photodiodes in parallel. Consequently, the hand-held probe need to mount all of 36 light source fibers and 16 fiber bundles, which deserves very careful design and mechanical machining. Although the system expansion will slow downthe data acquisition speed a little bit and increase the system cost accordingly, the prices are still cost-effective in terms of its significant performance improvement on image quality/resolution and the imaging area.

7.2.2 Clinical studies on breast

The ultimate objective of this research is to provide a clinically applicable instrument for women breast cancer detection. In the next research stage, research will focus on the functional and structural analyses. Women subjects with healthy and diseased breast tissue will be recruited for system performance evaluations in deep.

Firstly, the spectroscopic analyses will be conducted on healthy and diseased breast tissue respectively. The optical properties and the physiological parameters will be extracted. We will further analyze these spectroscopic parameters to explore and establish the intrinsic correspondence between the spectroscopic results and the breast cancer. Information will be compiled and reorganized as the prior knowledge before conducting clinical cancer diagnosis.

Secondly, the following *in-vivo* experiments will also be explored to evaluate the instrument mapping performance on the reduced scattering coefficient and

the absorption coefficient. The mapping results from healthy and diseased breast tissue will be imaged simultaneously for easy comparison and characterization side-by-side. The hemodynamic information will be imaged and analyzed in real time to offer a functional imaging performance.

Lastly, the instrument will be used to analyze the positional information on the women with cancerous breast. In the *in-vivo* experiments, the women will change her posture from sitting to supine, which will reduce the fluctuations of signal measurements induced by heart-beating and breathing of subject. In addition, the probing positions illustrated in Fig. 6-1 will change to new positions as illustrated in Fig. 7-1 because cancer occurrence rates are significant different at these four quadrants. Generally the regions around the armpits (e.g. R2 and L1 in Fig. 7-1) have higher cancer occurrence rate (> 68%) than the other three quadrant regions. Detection of abnormalities in these two regions would help to determine the cancer presence at the early stage before the cancer cell invades into other quadrants and other parts of body.

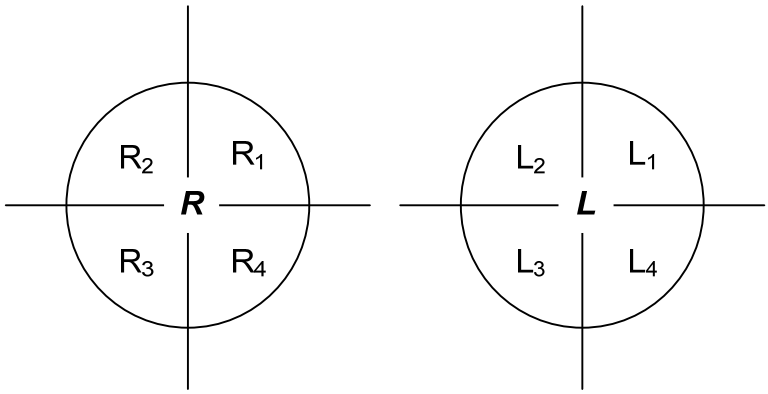

Fig. 7-1 Probing positions on 4 quadrant regions on the Left and Right breast (front view).

Bibliography

1. F. Jobsis, "Noninvasive, infrared monitoring of cerebral and myocardial oxygen sufficiency and circulatory parameters," *Science* **198,** 1264-1267 (1977).

2. Webpage, "Breast Cancer," http://en.wikipedia.org/wiki/Breast_cancer.

3. Webpage, "Breast cancer," (2009), http://en.wikipedia.org/w/index.php?title=Breast_cancer&oldid=302288968.

4. R. Voelker, "The world in medicine: breast cancer in europe," JAMA **284,** 2309 (2000).

5. A. Seow, S. W. Duffy, M. A. McGee, J. Lee, and H. P. Lee, "Breast cancer in Singapore: trends in incidence 1968-1992," *International Journal of Epidemiol* **25,** 40-45 (1996).

6. Webpage, "Cancer," (2009), http://www.who.int/mediacentre/factsheets/fs297/en/index.html

7. W. Mo, and N. Chen, "Fast time-domain diffuse optical tomography using pseudorandom bit sequences," *Otpics Express*, **16,** 13643-13650 (2008).

8. W. Mo, N. Chen, "Design of advanced time-domain diffuse optical tomography system," *IEEE Journal of Selected Topics in Quantum Electronics***, 9(11)**, 1-7, (2009).

9. W. Mo, T. Chan, L. Chen, N. Chen, "Quantitative characterization of optical and physiological parameters in normal breasts using time-resolved spectroscopy: in-vivo results of 19 Singapore women," *Journal of Biomedical Optics***, 16(4)**, 064004, (2009).

10. J. L. Boulnois, "Photophysical processes in recent medical laser developments: A review," *Lasers in Medical Science* **1,** 47-66 (1986).

11. W. F. Cheong, S. A. Prahl, and A. J. Welch, "A review of the optical properties of biological tissues," *Quantum Electronics, IEEE Journal of* **26,** 2166-2185 (1990).

12. M. S. Patterson, B. Chance, and B. C. Wilson, "Time resolved reflectance and transmittance for the non-invasive measurement of tissue optical properties," *Applied Optics*. **28,** 2331-2336 (1989),.

13. Webpage, "Specific Extinction Spectra of Tissue Chromophores", http://www.medphys.ucl.ac.uk/research/borl/research/NIR_topics/spectra/spectra.htm.

14. B. J. Tromberg, N. Shah, R. Lanning, A. Cerussi, J. Espinoza, T. Pham, L. Svaasand, and J. Butler, "Non-invasive in vivo characterization of breast tumors using photon migration spectroscopy," *Neoplasia* **2,** 26-40 (2000).

15. N. Shah, A. Cerussi, C. Eker, J. Espinoza, J. Butler, J. Fishkin, R. Hornung, and B. Tromberg, "Noninvasive functional optical spectroscopy of human breast tissue," *Proceedings of the National Academy of Sciences of the United States of America* **98,** 4420-4425 (2001).

16. J. Li, G. Dietsche, D. Iftime, S. E. Skipetrov, G. Maret, T. Elbert, B. Rockstroh, and T. Gisler, "Noninvasive detection of functional brain activity with near-infrared diffusing-wave spectroscopy," *Journal of Biomedical Optics* **10,** 044002-044012 (2005).

17. A. Cerussi, N. Shah, D. Hsiang, A. Durkin, J. Butler, and B. J. Tromberg, "In vivo absorption, scattering, and physiologic properties of 58 malignant breast tumors determined by broadband diffuse optical spectroscopy," *Journal of Biomedical Optics* **11,** 044005-044016 (2006),.

18. H. J. C. M. Sterenborg, R. L. P. van Veen, A. Pifferi, A. Torricelli and R. Cubeddu, "Optical Absorption of Fat", http://omlc.ogi.edu/spectra/fat/.

19. A. R. Young, "Chromophores in human skin," *Physics in Medicine and Biology* **42,** 789-802 (1997).

20. R. Y. Antony, "Chromophores in human skin," *Physics in Medicine and Biology* **42,** 789 (1997).

21. V. Kondepati, H. Heise, and J. Backhaus, "Recent applications of near-infrared spectroscopy in cancer diagnosis and therapy," *Analytical and Bioanalytical Chemistry,* **390,** 125-139 (2008).

22. S. Prahl, "Optical Absorption of Hemoglobin", http://omlc.ogi.edu/spectra/hemoglobin/index.html.

23. B. Tromberg, A. Cerussi, N. Shah, M. Compton, A. Durkin, D. Hsiang, J. Butler, and R. Mehta, "Imaging in breast cancer: Diffuse optics in breast cancer: detecting tumors in pre-menopausal women and monitoring neoadjuvant chemotherapy," *Breast Cancer Research* **7,** 279 - 285 (2005).

24. A. Zichichi, and K. Goebel, *International Seminar on Nuclear War : 10th session :planetary emergencies* (World Scientific, Singapore, 1992).

25. D. R. W. Leff, Oliver J. Enfield, Louise C. Gibson, Adam Athanasiou, Thanos Patten, Darren K. Hebden, Jem Yang, Guang Zhong, Darzi, Ara, "Diffuse optical imaging of the healthy and diseased breast: A systematic review," *Breast Cancer Research and Treatment* **108,** 9 (2008).

26. T. Durduran, R. Choe, J. Culver, L. Zubkov, M. Holboke, J. Giammarco, B. Chance, and A. Yodh, "Bulk optical properties of healthy female breast tissue," *Physics in Medicine and Biology* **47,** 2847 - 2861 (2002).

27. D. Grosenick, K. T. Moesta, H. Wabnitz, J. Mucke, C. Stroszczynski, R. Macdonald, P. M. Schlag, and H. Rinneberg, "Time-Domain Optical Mammography: Initial Clinical Results on Detection and Characterization of Breast Tumors," *Applied Optics*. **42,** 3170-3186 (2003).

28. S. Tomas, and et al., "Characterization of normal breast tissue heterogeneity using time-resolved near-infrared spectroscopy," *Physics in Medicine and Biology* **50,** 2559 (2005).

29. L. Spinelli, A. Torricelli, A. Pifferi, P. Taroni, G. M. Danesini, and R. Cubeddu, "Bulk optical properties and tissue components in the female breast from multiwavelength time-resolved optical mammography," *Journal of Biomedical Optics* **9,** 1137-1142 (2004).

30. P. Taroni, G. Danesini, A. Torricelli, A. Pifferi, L. Spinelli, and R. Cubeddu, "Clinical trial of time-resolved scanning optical mammography at 4 wavelengths between 683 and 975 nm," *Journal of Biomedical Optics* **9,** 464-473 (2004).

31. B. W. Pogue, S. Jiang, H. Dehghani, C. Kogel, S. Soho, S. Srinivasan, X. Song, T. D. Tosteson, S. P. Poplack, and K. D. Paulsen, "Characterization of hemoglobin, water, and NIR scattering in breast tissue: analysis of intersubject variability and menstrual cycle changes," *Journal of Biomedical Optics* **9,** 541-552 (2004).

32. S. P. Poplack, K. D. Paulsen, A. Hartov, P. M. Meaney, B. W. Pogue, T. D. Tosteson, M. R. Grove, S. K. Soho, and W. A. Wells, "Electromagnetic breast imaging: average tissue property values in women with negative clinical findings," *Radiology* **231,** 571-580 (2004).

33. S. Srinivasan, B. W. Pogue, S. Jiang, H. Dehghani, C. Kogel, S. Soho, J. J. Gibson, T. D. Tosteson, S. P. Poplack, and K. D. Paulsen, "Interpreting hemoglobin and water concentration, oxygen saturation, and scattering measured in vivo by near-infrared breast tomography," *Proceedings of the National Academy of Sciences of the United States of America* **100,** 12349-12354 (2003).

34. K. Suzuki, Y. Yamashita, K. Ohta, M. Kaneko, M. Yoshida, and B. Chance, "Quantitative measurement of optical parameters in normal breasts using time-resolved spectroscopy: in vivo results of 30 Japanese women," *Journal of Biomedical Optics* **1,** 330-334 (1996).

35. Webpage, "National Breast Cancer Awareness Month," (American Cancer Society, 2009).

36. Z. Kmietowicz, "Women aged over 40 who are at increased risk of breast cancer should get annual mammograms," *BMJ* **328,** 1515 (2004).

37. Webpage, "Siemens Rolls Out 1.5 Tesla MRI for Breast Visualization," (2009), http://www.medgadget.com/archives/2009/02/siemens_rolls_out_15_tesla_mri_for_breast_visualization.html.

38. Webpage, "Magnetic Resonance Breast Imaging (MRI, MR)," http://www.imaginis.com/breasthealth/mri.asp.

39. D. L. Hykes, W. R. Hedrick, and D. E. Starchman, *Ultrasound physics and instrumentation* (Mosby-Year Book, St. Louis, 1992).

40. D. Mankoff, "Imaging in breast cancer - breast cancer imaging revisited," *Breast Cancer Research* **7,** 276 - 278 (2005).

41. J. Basilion, "Current and future technologies for breast cancer imaging," *Breast Cancer Research* **3,** 14 - 16 (2001).

42. C. Lehman, and M. Schnall, "Magnetic resonance imaging of the breast," *Breast Cancer Research* **7,** 215 - 219 (2005).

43. M. Leach, "Application of magnetic resonance imaging to angiogenesis in breast cancer," *Breast Cancer Research*, **3,** 22 - 27 (2001).

44. M. Schnall, "Application of magnetic resonance imaging to early detection of breast cancer," *Breast Cancer Research* **3,** 17 - 21 (2001).

45. B. Bolan, M. Nelson, D. Yee, and M. Garwood, "Magnetic resonance spectroscopy of the breast," *Breast Cancer Research* **7,** 149 - 152 (2005).

46. F. Benard, and E. Turcotte, "Imaging breast cancer with signle photon computed tomography and positron emission tomography," *Breast Cancer Research* **7,** 153 - 162 (2005).

47. V. Ntziachristos, and B. Chance, "Probing physiology and molecular function using optical imaging: applications to breast cancer," *Breast Cancer Research* **3,** 41 - 46 (2001).

48. B. Tromberg, A. Cerussi, N. Shah, M. Compton, and A. Fedyk, "Diffuse optics in breast cancer: detection in pre-menopausal women, co-registration with MRI, and monitoring neo-adjuvant chemotherapy," *Breast Cancer Research* **7,** 279 - 285 (2005).

49. N. G. Chen, M. Huang, H. Xia, D. Piao, E. Cronin, and Q. Zhu, "Portable near-infrared diffusive light imager for breast cancer detection," *Journal of Biomedical Optics* **9,** 504-510 (2004).

50. D. J. Faber, M. C. G. Aalders, E. G. Mik, B. A. Hooper, M. J. C. van Gemert, and T. G. van Leeuwen, "Oxygen Saturation-Dependent Absorption and Scattering of Blood," *Physical Review Letters* **93,** 028102 (2004).

51. S. Jiang, B. W. Pogue, K. D. Paulsen, C. Kogel, and S. Poplack, "In vivo near-infrared spectral detection of pressure-induced changes in breast tissue," *Optics Letters* **28,** 1212-1214 (2003).

52. S. H. Tseng, A. Grant, and A. J. Durkin, "In vivo determination of skin near-infrared optical properties using diffuse optical spectroscopy," *J Journal of Biomedical Optics Opt* **13,** 014016 (2008),.

53. Y. Hoshi, "Functional near-infrared spectroscopy: current status and future prospects," *Journal of Biomedical Optics* **12,** 062106 (2007).

54. S. C. Bunce, M. Izzetoglu, K. Izzetoglu, B. Onaral, and K. Pourrezaei, "Functional near-infrared spectroscopy," *Engineering in Medicine and Biology Magazine, IEEE* **25,** 54-62 (2006).

55. T. M. Breslin, F. Xu, G. M. Palmer, C. Zhu, K. W. Gilchrist, and N. Ramanujam, "Autofluorescence and diffuse reflectance properties of malignant and benign breast tissues," *Ann Surg Oncol* **11,** 65-70 (2004).

56. X. Chen, M. Moore, C. Lehman, D. Mankoff, T. Lawton, S. Peacock, E. Schubert, and R. Livingston, "Combined use of MRI and PET to monitor response and assess residual disease for locally advanced breast cancer treated with neoadjuvant chemotherapy," *Acad Radiol* **11,** 1115 - 1124 (2004).

57. A. Li, E. L. Miller, M. E. Kilmer, T. J. Brukilacchio, T. Chaves, J. Stott, Q. Zhang, T. Wu, M. Chorlton, R. H. Moore, D. B. Kopans, and D. A. Boas, "Tomographic optical breast imaging guided by three-dimensional mammography," *Applied Optics,* **42,** 5181-5190 (2003).

58. Q. Zhu, S. Kurtzma, P. Hegde, S. Tannenbaum, M. Kane, M. Huang, N. Chen, B. Jagjivan, and K. Zarfos, "Utilizing optical tomography with ultrasound localization to image heterogeneous hemoglobin distribution in large breast cancers," *Neoplasia* **7,** 263 - 270 (2005).

59. Q. Zhu, M. Huang, N. Chen, K. Zarfos, B. Jagjivan, M. Kane, P. Hedge, and S. Kurtzman, "Ultrasound-guided optical tomographic imaging of malignant and benign breast lesions: initial clinical results of 19 cases," *Neoplasia* **5,** 379 - 388 (2003).

60. Webpage, "Breast Cancer Imaging Reviewed," (2005), http://www.snm.org/index.cfm?PageID=4672&RPID=7320.

61. P. Martinsen, J.-L. Charlier, T. Willcox, G. Warman, A. McGlone, and R. Kunnemeyer, "Temperature dependence of near-infrared spectra of whole blood," *Journal of Biomedical Optics* ***13,*** 034016-034017 (2008).

62. E. Salomatina, B. Jiang, J. Novak, and A. N. Yaroslavsky, "Optical properties of normal and cancerous human skin in the visible and near-infrared spectral range," *Journal of Biomedical Optics* **11,** 064026 (2006).

63. A. Roggan, M. Friebel, K. Dorschel, A. Hahn, and G. Muller, "Optical Properties of Circulating Human Blood in the Wavelength Range 400--2500 nm," *Journal of Biomedical Optics* **4,** 36-46 (1999).

64. K. J. Jeon, S. J. Kim, K. K. Park, J. W. Kim, and G. Yoon, "Noninvasive total hemoglobin measurement," *Journal of Biomedical Optics* **7,** 45-50 (2002).

65. R. Boushel, J. Olesen, J. Gonzales-Alonzo, J. Bulow, M. Kjar, "Monitoring tissue oxygen availability with near infrared spectroscopy (NIRS) in health and disease," *Scandinavian Journal of Medicine & Science in Sports* **11,** 213-222 (2001).

66. M. Friebel, J. Helfmann, G. Muller, and M. Meinke, "Influence of shear rate on the optical properties of human blood in the spectral range 250 to 1100 nm," *Journal of Biomedical Optics* **12,** 054005-054008 (2007).

67. J. Hebden, T. Yates, A. Gibson, N. Everdell, S. Arridge, D. Chicken, M. Douek, and M. S. Keshtgar, "Monitoring recovery after laser surgery of the breast with optical tomography: a case study," *Applied Optics,* **44(6),** 1898-1904, (2005).

68. T. D. Yates, J. C. Hebden, A. P. Gibson, L. Enfield, N. L. Everdell, S. R. Arridge, and D. T. Delpy, "Time-resolved optical mammography using a liquid coupled interface," *Journal of Biomedical Optics* **10,** 054011-054010 (2005).

69. H. Zhao, F. Gao, Y. Tanikawa, and Y. Yamada, "Time-resolved diffuse optical tomography and its application to in vitro and in vivo imaging," *Journal of Biomedical Optics* **12,** 062107-062113 (2007).

70. L. C. Enfield, A. P. Gibson, N. L. Everdell, D. T. Delpy, M. Schweiger, S. R. Arridge, C. Richardson, M. Keshtgar, M. Douek, and J. C. Hebden, "Three-dimensional time-resolved optical mammography of the uncompressed breast," *Applied Optics,* **46 (6),** 3628-3638, (2007).

71. G. Boverman, Q. Fang, S. A. Carp, E. L. Miller, D. H. Brooks, J. Selb, R. H. Moore, D. B. Kopans, and D. A. Boas, "Spatio-temporal imaging of the hemoglobin in the compressed breast with diffuse optical tomography," *Physics in Medicine and Biology* **52,** 3619-3641 (2007).

72. V. G. Peters, D. R. Wyman, M. S. Patterson, and G. L. Frank, "Opitcal-properties of normal and diseased human breast tissue in the visible and near-infrared," *Physics in Medicine and Biology* **35,** 1317-1334 (1990).

73. J. P. Culver, A. M. Siegel, J. J. Stott, and D. A. Boas, "Volumetric diffuse optical tomography of brain activity," *Optics Letters* **28,** 2061-2063 (2003).

74. J. Hebden, and T. Austin, "Optical tomography of the neonatal brain," *European Radiology* **17,** 2926-2933 (2007).

75. H. Dehghani, and D. T. Delpy, "Near-Infrared Spectroscopy of the Adult Head: Effect of Scattering and Absorbing Obstructions in the Cerebrospinal Fluid Layer On Light Distribution in the Tissue," *Applied Optics,* **39(6),** 4721-4729, (2000).

76. E. Okada, and D. T. Delpy, "Near-Infrared Light Propagation in an Adult Head Model. I. Modeling of Low-Level Scattering in the Cerebrospinal Fluid Layer," *Applied Optics,* **42(6),** 2906-2914, (2003).

77. E. Okada, and D. T. Delpy, "Near-Infrared Light Propagation in an Adult Head Model. II. Effect of Superficial Tissue Thickness on the Sensitivity of the Near-Infrared Spectroscopy Signal," *Applied Optics,* **42(6),** 2915-2922, (2003).

78. Yoko Hoshi, "Functional near-infrared optical imaging: Utility and limitations in human brain mapping," *Psychophysiology* **40,** 511-520 (2003).

79. A. Pifferi, A. Torricelli, P. Taroni, A. Bassi, E. Chikoidze, E. Giambattistelli, and R. Cubeddu, "Optical biopsy of bone tissue: a step toward the diagnosis of bone pathologies," *Journal of Biomedical Optics* **9,** 474-480 (2004).

80. C. A. Piantadosi, and R. Boushel, "Near-infrared spectroscopy for monitoring muscle oxygenation," *Acta Physiologica Scandinavica* **168,** 615-622 (2000).

81. G. Pichler, B. Urlesberger, P. Jirak, H. Zotter, uuml, and W. ller, "Forearm Oxygen Consumption and Forearm Blood Flow in Healthy Children and Adolescents Measured by Near Infrared Spectroscopy," T*he Journal of Physiological Sciences* **56,** 191-194 (2006).

82. D. J. Saltzman. A. E. Cerussi. D. V. Gelfand. J. Milliken. T. Waddington. B. J. Tromberg. J. Lee, and M. Brenner, "Broadband diffuse optical spectroscopy measurement of hemoglobin concentration during hypovolemia in rabbits," *Physiological Measurement* **27,** 757 (2006).

83. B. A. Torkian, A. T. Yeh, R. Engel, C. H. Sun, B. J. Tromberg, and B. J. Wong, "Modeling aberrant wound healing using tissue-engineered skin constructs and multiphoton microscopy," *Arch Facial Plast Surg* **6,** 180-187 (2004).

84. J. W. Meng, H. M. Gu, R. E. Zheng, D. Xing, J. Wang, R. Wang, and Y. D. Zhang, "The non-trauma fluorescence analysis of the porphyrin in the blood of human superficial skin tissue," *Guang Pu Xue Yu Guang Pu Fen Xi* **23,** 325-327 (2003).

85. J. Lee, D. J. Saltzman, A. E. Cerussi, D. V. Gelfand, J. Milliken, T. Waddington, B. J. Tromberg, and M. Brenner, "Broadband diffuse optical spectroscopy measurement of hemoglobin concentration during hypovolemia in rabbits," *Physiol. Meas.* **27,** 757-767 (2006).

86. V. V. Tuchin, "A Clear Vision for Laser Diagnostics (Review)," S*elected Topics in Quantum Electronics, IEEE Journal* of **13,** 1621-1628 (2007).

87. V. Tuchin, *Tissue optics : light scattering methods and instruments for medical diagnosis* (SPIE Optical Engineering Press, Bellingham, WA, 2000).

88. M. Patterson, J. Moulton, B. Wilson, K. Berndt, and J. Lakowicz, "Frequency-domain reflectance for the determination of the scattering and absorption properties of tissue," *Applied Optics,* **30,** 4474 - 4476 (1991).

89. K. Furutsu, and Y. Yamada, "Diffusion approximation for a dissipative random medium and the applications," *Physical Review* E **50,** 3634 (1994).

90. R. Pierrat, J.-J. Greffet, and R. Carminati, "Photon diffusion coefficient in scattering and absorbing media," *J. Opt. Soc. Am. A* **23,** 1106-1110 (2006).

91. S. J. Matcher, "Nonuniqueness in optical tomography: relevance of the P1 approximation," *Optics Letters* **24,** 1729-1731, (1999).

92. C. K. Hayakawa, B. Y. Hill, J. S. You, F. Bevilacqua, J. Spanier, and V. Venugopalan, "Use of the δ-P1 Approximation for Recovery of Optical Absorption, Scattering, and Asymmetry Coefficients in Turbid Media," *Applied Optics,* **43,** 4677-4684, (2004).

93. N. G. Chen, and J. Bai, "Monte Carlo Approach to Modeling of Boundary Conditions for the Diffusion Equation," *Physical Review Letters* **80,** 5321, (1998).

94. S. L. Jacques, and B. W. Pogue, "Tutorial on diffuse light transport," *Journal of Biomedical Optics* **13,** 041302-041319, (2008).

95. R. A. J. Groenhuis, H. A. Ferwerda, and J. J. T. Bosch, "Scattering and absorption of turbid materials determined from reflection measurements. 1: Theory," *Applied Optics,***22,** 2456-2462 (1983).

96. R. A. Simon, and C. H. Jeremy, "Optical imaging in medicine: II. Modelling and reconstruction," *Physics in Medicine and Biology* **42,** 841 (1997).

97. C. Zhu, G. M. Palmer, T. M. Breslin, J. Harter, and N. Ramanujam, "Diagnosis of breast cancer using fluorescence and diffuse reflectance spectroscopy: a Monte-Carlo-model-based approach," *Journal of Biomedical Optics,* **13,** 034015 (2008).

98. G. M. Palmer, C. Zhu, T. M. Breslin, F. Xu, K. W. Gilchrist, and N. Ramanujam, "Monte Carlo-based inverse model for calculating tissue

optical properties. Part II: Application to breast cancer diagnosis," *Applied Optics,* **45,** 1072-1078 (2006).

99. S. Prince, and S. Malarvizhi, "Monte Carlo simulation of NIR diffuse reflectance in the normal and diseased human breast tissues," *Biofactors* **30,** 255-263 (2007).

100. M. Bohnert, R. Walther, T. Roths, and J. Honerkamp, "A Monte Carlo-based model for steady-state diffuse reflectance spectrometry in human skin: estimation of carbon monoxide concentration in livor mortis," *Int J Legal Med* **119,** 355-362 (2005).

101. S. R. Arridge, "Optical tomography in medical imaging," *Inverse Problems* **15,** 53 (1999).

102. W. V. G. Aguilar, Rong Zhang, and J. S. Nelson, "Comparison of diffusion approximation and Monte Carlo based finite element models for simulating thermal responses to laser irradiation in discrete vessels," *Physics in Medicine and Biology* **50,** 4075 (2005).

103. J. C. H. a. S. R. A. A. P. Gibson, "Recent advances in diffuse optical imaging," *Physics in Medicine and Biology* **50,** R1 (2005).

104. R. C. Haskell, L. O. Svaasand, T.-T. Tsay, T.-C. Feng, M. S. McAdams, and B. J. Tromberg, "Boundary conditions for the diffusion equation in radiative transfer," *J. Opt. Soc. Am. A* **11,** 2727-2741 (1994).

105. M. Patterson, B. Chance, and B. Wilson, "Time resolved reflectance and transmittance for the non-invasive measurement of tissue optical properties," *Applied Optics*,**28,** 2331 - 2336 (1989).

106. T. J. Farrell, M. S. Patterson, and B. Wilson, "A diffusion theory model of spatially resolved, steady-state diffuse reflectance for the noninvasive determination of tissue optical properties in vivo," *Medical Physics* **19,** 879-888 (1992).

107. B. W. Pogue, and M. S. Patterson, "Error assessment of a wavelength tunable frequency domain system for noninvasive tissue spectroscopy," *Journal of Biomedical Optics* **1,** 311-323 (1996).

108. A. Ishimaru, *Wave propagation and scattering in random media* (Academic Press, New York, 1978).

109. R. Choe, "Diffuse optical tomography and spectroscopy of breast cancer and fetal brain," (University of Pennsylvania, 2005., 2005), pp. xxii, 226 p.

110. T. Durduran, "Non-invasive measurements of tissue hemodynamics with hybrid diffuse optical methods," (University of Pennsylvania, 2004., 2004), pp. xxi, 266 p.

111. S. R. Arridge, and et al., "The theoretical basis for the determination of optical pathlengths in tissue: temporal and frequency analysis," *Physics in Medicine and Biology* **37,** 1531 (1992).

112. S. R. Arridge, "Photon-measurement density functions. Part I: Analytical forms," *Applied Optics,*. **34,** 7395-7409 (1995).

113. M. Cutler, "Transillumination of the Breast," *Ann Surg* **93,** 223-234 (1931).

114. S. R. Arridge, and W. R. B. Lionheart, "Nonuniqueness in diffusion-based optical tomography," *Optics Letters* **23,** 882-884 (1998).

115. J. C. Schotland, "Continuous-wave diffusion imaging," *J. Opt. Soc. Am. A* **14,** 275-279 (1997).

116. U. Sunar, H. Quon, T. Durduran, J. Zhang, J. Du, C. Zhou, G. Yu, R. Choe, A. Kilger, R. Lustig, L. Loevner, S. Nioka, B. Chance, and A. G. Yodh, "Noninvasive diffuse optical measurement of blood flow and blood oxygenation for monitoring radiation therapy in patients with head and neck tumors: a pilot study," *Journal of Biomedical Optics* **11,** 064021-064013 (2006).

117. U. Sunar, S. Makonnen, C. Zhou, T. Durduran, G. Yu, H.-W. Wang, W. M. Lee, and A. G. Yodh, "Hemodynamic responses to antivascular therapy and ionizing radiation assessed by diffuse optical spectroscopies," *Optics Express* **15,** 15507-15516 (2007).

118. L. B. Randall, A. Randy, S. Quan, L. G. Harry, and S. Ira, "Development and evaluation of the IRIS-OPTIscanner, a general-purpose optical tomographic imaging system," in *Advances in Optical Imaging and Photon Migration*, (Optical Society of America, 1998), p. ATuB3.

119. J. M. Masciotti. J. M. Lasker. M. Schoenecker. C. H. Schmitz, and H. H. Andreas, "Digital-signal-processor-based dynamic imaging system for optical tomography," *Review of Scientific Instruments* **78,** 083706 (2007).

120. Y. Yamashita, A. Maki, and H. Koizumi, "Measurement System for Noninvasive Dynamic Optical Topography," *Journal of Biomedical Optics* **4,** 414-417 (1999).

121. B. Chance, M. Cope, E. Gratton, N. Ramanujam, and B. Tromberg, "Phase measurement of light absorption and scatter in human tissue," *Review of Scientific Instruments* **69,** 3457-3481 (1998).

122. R. A. J. Groenhuis, J. J. T. Bosch, and H. A. Ferwerda, "Scattering and absorption of turbid materials determined from reflection measurements. 2: Measuring method and calibration," *Applied Optics,***22,** 2463-2467 (1983).

123. S. R. Arridge. J. C Hebden, and T. D. David, "Optical imaging in medicine: I. Experimental techniques," *Physics in Medicine and Biology* **42,** 825 (1997).

124. F. Gao, H. Zhao, and Y. Yamada, "Improvement of Image Quality in Diffuse Optical Tomography by use of Full Time-Resolved Data," *Applied Optics,* **41,** 778-791 (2002).

125. J. R. Lakowicz, and K. Berndt, "Frequency-domain measurements of photon migration in tissues," *Chemical Physics Letters* **166,** 246-252 (1990).

126. J. Wang, S. C. Davis, S. Srinivasan, S. Jiang, B. W. Pogue, and K. D. Paulsen, "Spectral tomography with diffuse near-infrared light: inclusion of broadband frequency domain spectral data," *Journal of Biomedical Optics* **13,** 041305-041310 (2008).

127. B. J. Tromberg, O. Coquoz, J. B. Fishkin, T. Pham, E. R. Anderson, J. Butler, M. Cahn, J. D. Gross, V. Venugopalan, and D. Pham, "Non-invasive measurements of breast tissue optical properties using frequency-domain photon migration," *Philos Trans R Soc Lond B Biol Sci* **352,** 661-668 (1997).

128. J. Zhao, H. S. Ding, X. L. Hou, C. L. Zhou, and B. Chance, "In vivo determination of the optical properties of infant brain using frequency-domain near-infrared spectroscopy," *Journal of Biomedical Optics* **10,** 024028-024027 (2005).

129. M. A. O'Leary, D. A. Boas, B. Chance, and A. G. Yodh, "Experimental images of heterogeneous turbid media by frequency-domain diffusing-photon tomography," *Optics Letters*. **20,** 426-428 (1995).

130. E. G. Michael Maris, John Maier, William Mantulin, Britton Chance,, "Functional near-infrared imaging of deoxygenated hemoglobin during exercise of the finger extensor muscles using the frequency-domain technique," *Bioimaging* **2,** 174-183 (1994).

131. W. M. M. E. Gratton, M. J. vande Ven, J. B. Fishkin, M. B. Maris, and B. Chance, "A novel approach to laser tomography," *Bioimaging* **1,** 40-46 (1993).

132. M. Franceschini, K. Moesta, S. Fantini, G. Gaida, E. Gratton, H. Jess, W. Mantulin, M. Seeber, P. Schlag, and M. Kaschke, "Frequency-domain techniques enhance optical mammography: initial clinical results," *Proceedings of the National Academy of Sciences of the United States of America* **94,** 6468 - 6473 (1997).

133. G. Mitic, J. Kozer, J. Otto, E. Plies, G. Sokner, and W. Zinth, "Time-gated transillumination of biological tissues and tissuelike phantoms," *Applied Optics,* **33,** 6699-6710 (1994).

134. S. B. B. Colak, D. G. Papaioannou, G. W. t'Hooft, and M. B. van der Mark, "Optical image reconstruction with deconvolution in light diffusing media," in *Photon Propagation in Tissues*, (SPIE, Barcelona, Spain), 306-315 (1995).

135. G. Pal, S. Basu, K. Mitra, and T. Vo-Dinh, "Time-resolved optical tomography using short-pulse laser for tumor detection," *Applied Optics,***45,** 6270-6282 (2006).

136. J. C. Hebden, D. J. Hall, M. Firbank, and D. T. Delpy, "Time-resolved optical imaging of a solid tissue-equivalent phantom," *Applied Optics,***34,** 8038 (1995).

137. S. V. Patwardhan, and J. P. Culver, "Quantitative diffuse optical tomography for small animals using an ultrafast gated image intensifier," *Journal of Biomedical Optics* **13,** 011009-011007 (2008).

138. A. Gibson, R. M. Yusof, H. Dehghani, J. Riley, N. Everdell, R. Richards, J. C. Hebden, M. Schweiger, S. R. Arridge, and D. T. Delpy, "Optical Tomography of a Realistic Neonatal Head Phantom," *Applied Optics,* **42(6),** 3109-3116, (2003).

139. V. Y. Soloviev, K. B. Tahir, J. McGinty, D. S. Elson, M. A. A. Neil, P. M. W. French, and S. R. Arridge, "Fluorescence lifetime imaging by using time-gated data acquisition," *Applied Optics, **46(6),** 7384-7391, (2007).*

140. F. E. W. Schmidt, M. E. Fry, E. M. C. Hillman, J. C. Hebden, and D. T. Delpy, "A 32-channel time-resolved instrument for medical optical tomography," *Review of Scientific Instruments* **71,** 256-265 (2000).

141. C. V. Zint, W. Uhring, M. Torregrossa, B. Cunin, and P. Poulet, "Streak Camera: A Multidetector for Diffuse Optical Tomography," *Applied Optics,***42,** 3313-3320 (2003).

142. D. T. Delpy, and et al., "Estimation of optical pathlength through tissue from direct time of flight measurement," *Physics in Medicine and Biology* **33,** 1433 (1988).

143. P. P. Ho, P. Baldeck, K. S. Wong, K. M. Yoo, D. Lee, and R. R. Alfano, "Time dynamics of photon migration in semiopaque random media," *Applied Optics,* **28,** 2304-2310 (1989).

144. R. K. David, and T. D. David, "Measurement of tissue temporal point spread function (TPSF) by use of a gain-modulated avalanche photodiode detector," *Physics in Medicine and Biology* **41,** 939 (1996).

145. M. Oda, Y. Yamashita, H. Kan, H. Miyajima, A. Sawaki, T. Nakano, S. Suzuki, A. Suzuki, K. Shimizu, S. Muramatsu, N. Sugiura, K. Ohta, and Y. Tsuchiya, "Advanced devices for near-infrared time-resolved spectroscopy and optical computed tomography: high-sensitive/fast PMT, high-power PLP, miniaturized CFD/TAC module, and high-speed

multichannel signa," in *Optical Tomography and Spectroscopy of Tissue: Theory, Instrumentation, Model, and Human Studies II*, (SPIE, San Jose, CA, USA), 765-773, (1997).

146. H. Eda, I. Oda, Y. Ito, Y. Wada, Y. Oikawa, Y. Tsunazawa, M. Takada, Y. Tsuchiya, Y. Yamashita, M. Oda, A. Sassaroli, Y. Yamada, and M. Tamura, "Multichannel time-resolved optical tomographic imaging system," *Review of Scientific Instruments* **70,** 3595-3602 (1999).

147. H. Arimoto, M. Egawa, and Y. Yamada, "Depth profile of diffuse reflectance near-infrared spectroscopy for measurement of water content in skin," *Skin Res Technol* **11,** 27-35 (2005).

148. H. Zhao. F. Gao. Yukari Tanikawa, and Y. Yukio, "Time-resolved diffuse optical tomography and its application to in vitro and in vivo imaging," *Journal of Biomedical Optics* **12,** 062107 (2007).

149. V. Ntziachristos, X. Ma, A. G. Yodh, and B. Chance, "Multichannel photon counting instrument for spatially resolved near infrared spectroscopy," *Review of Scientific Instruments* **70,** 193-201 (1999).

150. V. Ntziachristos, and B. Chance, "Probing physiology and molecular function using optical imaging: applications to breast cancer," *Breast Cancer Research* **3,** 41-46 (2001).

151. V. Ntziachristos, A. G. Yodh, M. D. Schnall, and B. Chance, "MRI-guided diffuse optical spectroscopy of malignant and benign breast lesions," *Neoplasia* **4,** 347-354 (2002).

152. S. Nioka, S. Wen, J. Zhang, J. Du, X. Intes, Z. Zhao, and B. Chance, "Simulation study of breast tissue hemodynamics during pressure perturbation," *Adv Exp Med Biol* **566,** 17 - 22 (2006).

153. N. Shah, A. E. Cerussi, D. Jakubowski, D. Hsiang, J. Butler, and B. J. Tromberg, "Spatial variations in optical and physiological properties of healthy breast tissue," *Journal of Biomedical Optics* **9,** 534-540 (2004).

154. A. Cerussi, R. Van Woerkom, F. Waffarn, and B. Tromberg, "Noninvasive monitoring of red blood cell transfusion in very low birthweight infants using diffuse optical spectroscopy," *Journal of Biomedical Optics* **10,** 051401 (2005).

155. A. Cerussi, D. Hsiang, N. Shah, R. Mehta, A. Durkin, J. Butler, and B. J. Tromberg, "Predicting response to breast cancer neoadjuvant chemotherapy using diffuse optical spectroscopy," *Proceedings of the National Academy of Sciences of the United States of America* **104,** 4014-4019 (2007).

156. B. J. Tromberg, B. W. Pogue, K. D. Paulsen, A. G. Yodh, D. A. Boas, and A. E. Cerussi, "Assessing the future of diffuse optical imaging technologies for breast cancer management," *Medical Physics* **35,** 2443-2451 (2008).

157. F. E. W. Schmidt, M. E. Fry, E. M. C. Hillman, J. C. Hebden, and D. T. Delpy, "A 32-channel time-resolved instrument for medical optical tomography," *Review of Scientific Instruments* **71(6),** 256-265,(2000).

158. T. Yates, J. Hebden, A. Gibson, N. Everdell, S. Arridge, and M. Douek, "Optical tomography of the breast using a multi-channel time-resolved imager," *Physics in Medicine and Biology* **50,** 2503 - 2517 (2005).

159. N. G. Chen, and Q. Zhu, "Time-resolved optical measurements with spread spectrum excitation," *Optics Letters* **27,** 1806-1808 (2002).

160. W. Mo, and N. Chen, "Source stabilization for high quality time-domain diffuse optical tomography," in *Design and Quality for Biomedical Technologies II*, (SPIE, San Jose, CA, USA, 2009), pp. 71700N-71709.

161. Webpage, "DL 100, Toptica," http://www.toptica.com/index.php?categorie=1&itemid=32&linkitemid=1111.

162. Webpage, "Modulator, EOSPACE," http://www.eospace.com/.

163. Webpage, "SM/MM Fiber Optic Switches," http://www.photonik.com.sg/products/Passive_Fiber_Optical_Modules/Fiber_Optic_Switch/index.asp.

164. Webpage, "XUPV2P documentation," http://www.xilinx.com/univ/xupv2p.html.

165. Webpage, "CDCE913," http://focus.ti.com/docs/prod/folders/print/cdce913.html.

166. Webpage, "Si APD S2383, Hamamtasu," http://jp.hamamatsu.com/products/sensor-ssd/pd078/pd079/pd080/S2383/index_en.html.

167. Webpage, "Ultra-high performance signal control equipment, GigaBaudics, Co," http://www.gigabaudics.com/.

168. Webpage, "Thermistor, MP-2371, TE Technology, Inc.," http://www.tetech.com/Thermistors/MP-2371.html.

169. Webpage, "PID-1500, WAVELENGTH," (2008), ftp://ftp.teamwavelength.com/pub/downloads/pidseries.pdf.

170. Webpage, "TH10K Thermistor, THORLABS," http://www.thorlabs.com/thorProduct.cfm?partNumber=TH10K.

171. Webpage, "TC-24-10, TE Technology, INC," http://www.tetech.com/Temperature-Controllers/TC-24-10.html.

172. R. A. Becker, and R. C. Williamson, "Photorefractive effects in $LiNbO_3$ channel waveguides: Model and experimental verification," *Applied Physics Letters* **47,** 1024-1026 (1985).

173. H. Nagata, K. Kiuchi, and T. Saito, "Studies of thermal drift as a source of output instabilities in Ti:$LiNbO_3$ optical modulators," *Journal of Applied Physics* **75,** 4762-4764 (1994).

174. J. Snoddy, Y. Li, F. Ravet, and X. Bao, "Stabilization of electro-optic modulator bias voltage drift using a lock-in amplifier and a proportional-integral-derivative controller in a distributed Brillouin sensor system," *Applied Optics,* **46,** 1482-1485 (2007).

175. J. R. Hamilton, and K. D. Masterson, "Accurate bias point control for an electrically isolated Mach-Zehnder interferometric modulator via an analog optical-fiber link," in *Interferometry XII: Techniques and Analysis*, (SPIE, Denver, CO, USA, 2004), pp. 323-331.

176. Webpage, "NI USB-6251," http://sine.ni.com/nips/cds/view/p/lang/en/nid/202597.

177. B. D. Price. A. P. Gibson. J. C Hebden, and R. Gary, "A soft deformable tissue-equivalent phantom for diffuse optical tomography," *Physics in Medicine and Biology* **51,** 5581 (2006).

178. M. Firbank, M. Oda, and D. T. Delpy, "An improved design for a stable and reproducible phantom material for use in near-infrared spectroscopy and imaging," *Physics in Medicine and Biology* **40,** 955-961 (1995).

179. F. E. Schmidt, J. C. Hebden, E. M. Hillman, M. E. Fry, M. Schweiger, H. Dehghani, D. T. Delpy, and S. R. Arridge, "Multiple-slice imaging of a tissue-equivalent phantom by use of time-resolved optical tomography," *Applied Optics* **39,** 3380-3387 (2000).

180. J. C. Hebden, J. Brunker, T. Correia, B. D. Price, A. P. Gibson, and N. L. Everdell, "An electrically-activated dynamic tissue-equivalent phantom for assessment of diffuse optical imaging systems," *Physics in Medicine and Biology* **53,** 329-337 (2008).

181. J. C. Hebden, B. D. Price, A. P. Gibson, and G. Royle, "A soft deformable tissue-equivalent phantom for diffuse optical tomography," *Physics in Medicine and Biology* **51,** 5581-5590 (2006).

182. C. U. Devi, R. M. Vasu, and A. K. Sood, "Design, fabrication, and characterization of a tissue-equivalent phantom for optical elastography," *Journal of Biomedical Optics* **10,** 44020 (2005).

183. R. Srinivasan, and M. Singh, "Development of biological tissue-equivalent phantoms for optical imaging," *Indian J Exp Biol* **40,** 531-535 (2002).

184. Webpage, "Lipofundin MCT/LCT, B. Braun," http://www.bbraun.co.id/index.cfm?0E9182739CF946FAAFF0B8EED491348C.

185. P. Kline, *An easy guide to factor analysis* (: Routledge, London ; New York, 1994).

186. O. Lutz, Z. Meraihi, J. Mura, A. Frey, G. Riess, and A. Bach, "Fat emulsion particle size: influence on the clearance rate and the tissue lipolytic activity," Am J Clin Nutr **50,** 1370-1381 (1989), http://www.ajcn.org/cgi/content/abstract/50/6/1370.

187. D. Contini, H. Liszka, A. Sassaroli, and G. Zaccanti, "Imaging of highly turbid media by the absorption method," *Applied Optics,* **35,** 2315-2324 (1996).

188. Prerana, M. R. Shenoy, and B. P. Pal, "Method to determine the optical properties of turbid media," *Applied Optics,* **47,** 3216-3220 (2008).

189. Webpage, "Mie Scattering Calculator," http://omlc.ogi.edu/calc/mie_calc.html.

190. A. Akkar, and R. H. Moler, "Formulation of intravenous Carbamazepine emulsions by SolEmuls®technology," *European Journal of Pharmaceutics and Biopharmaceutics* **55,** 305-312 (2003).

Appendix

A.1 Bias controller using MSP430F4270

A.1.1 Schematic

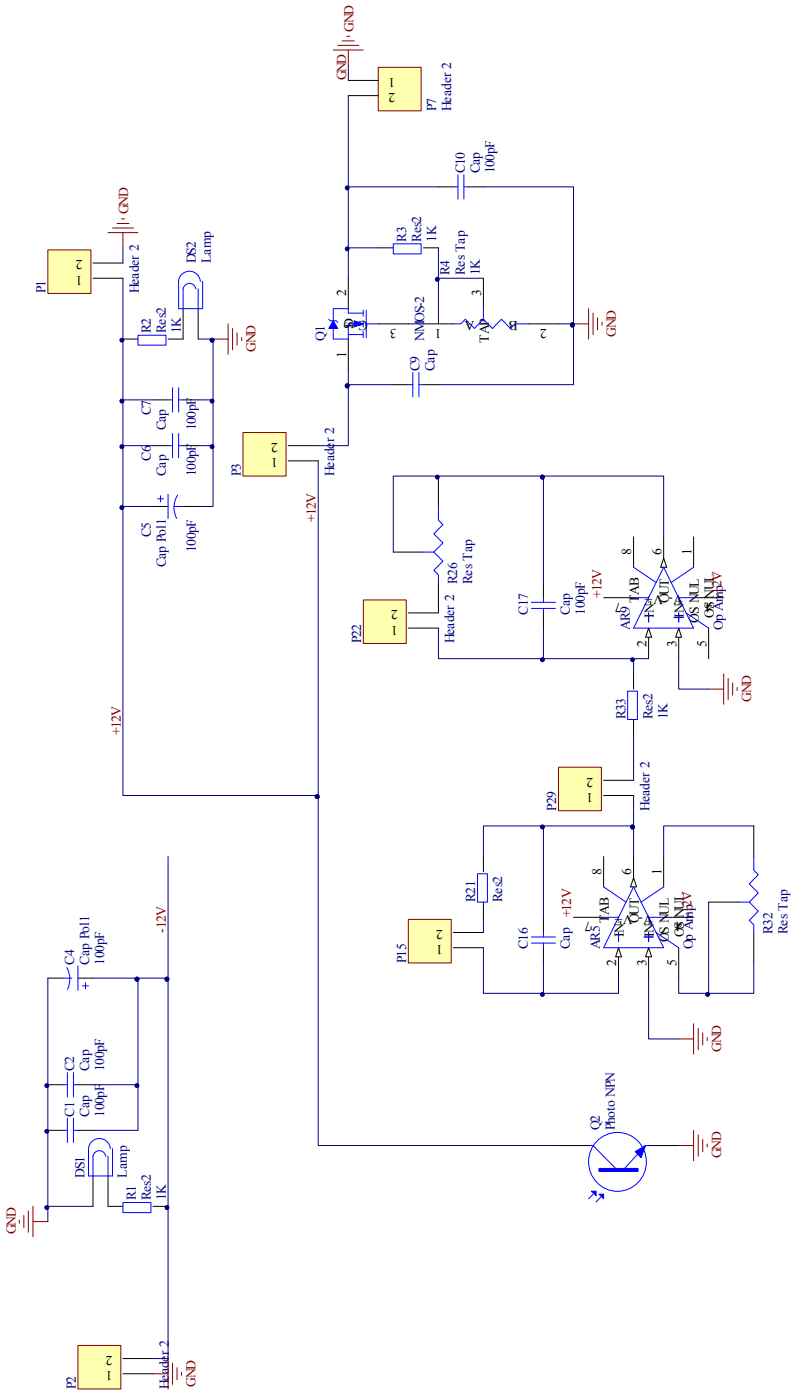

Fig. A- 1 Circuit schematic of bias controller for MZM (1/2).

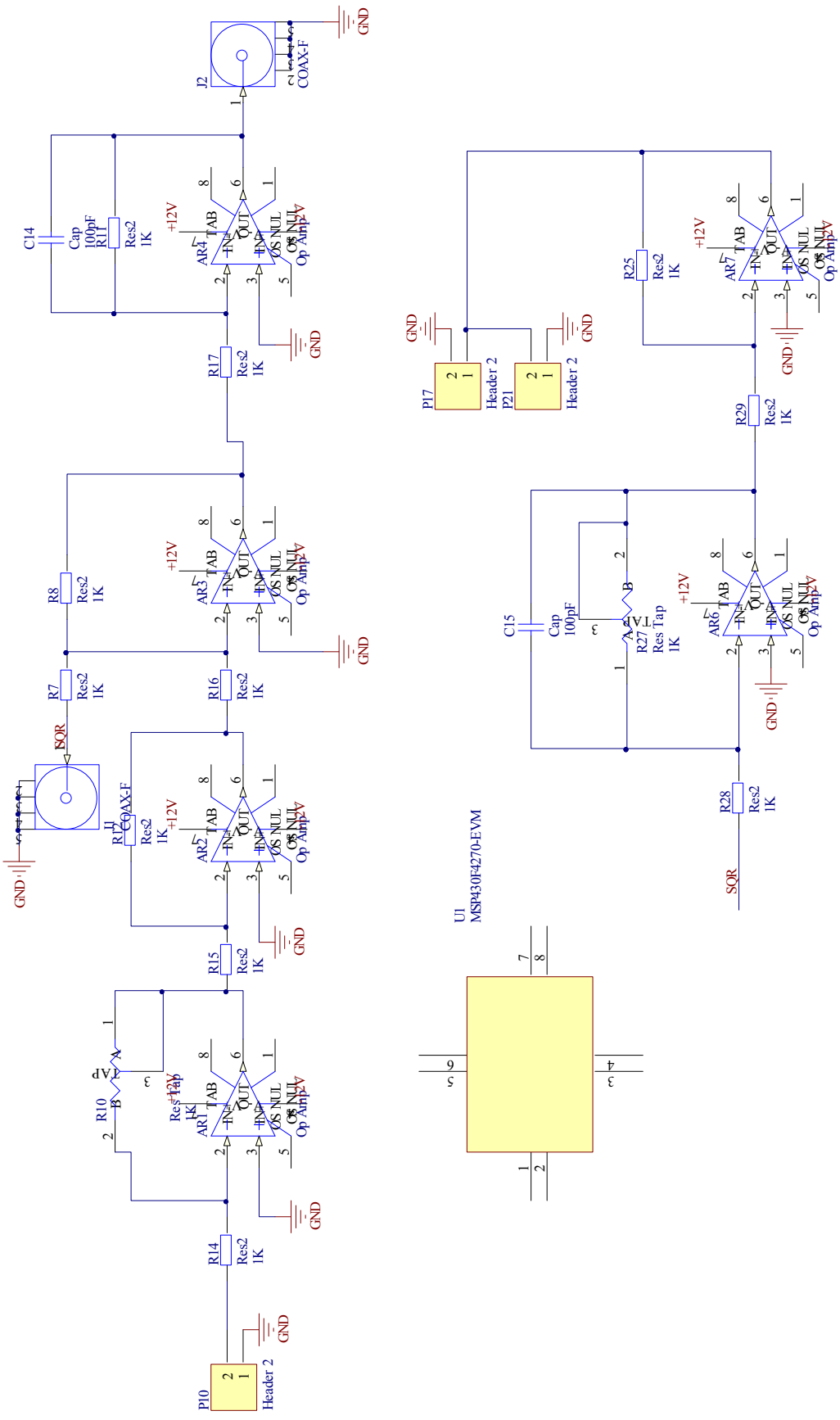

Fig. A- 2 Circuit schematic of bias stabilizer for MZM (2/2).

A.1.2 Software (C-code) – compiled using IAR™ (Ver. 4.11) IDE.

```
////////////////////////////////////////////////////////////
//////
// Intensity modulator stabilizer using MSP430F4270.
////////////////////////////////////////////////////////////
//////
#include  <msp430x42x0.h>

#define Num_of_Results 8  // acq. Samples using 2.5 KHz square
wave
#define Vpi 773           // Vpi = 773 x 3V(ref) x 3(amp)/4096
= 1.698 Vact

#define Ath 400   // accep.thres. btw 1st & 2nd sample datasets
#define OPT 100   // Optimal range btw 1st & 2nd sample
datasets
#define BigStep 8         // step size
#define SmallStep 4       // step size

int DIR;                  // bias shifting direction

unsigned char Vstep  = 8;
                             // step = 10 x 3V (ref) x 3(amp)
                             / 4096 // =  0.035 Vact = 2% Vpi
unsigned char sIndex = 0;     // index of data acquisition

unsigned char tP1IES;         // temp var. to save P1IES

unsigned int V785 = 0;        // bias for 785 nm
unsigned int V808 = 0;        // bias for 808 nm
unsigned int SCount = 0;      // samples (by count) depend on
square wave duration
unsigned int Vout, rVout;     // (dynamic) bias voltage
unsigned int DelayCount;      // delay btw two bias updating
events

unsigned long  fAvg,  sAvg;   // avg. of 1st half & 2nd half
unsigned long rfAvg, rsAvg;   // avg. of 1st half & 2nd half
(ref)

long Diff, rDiff;         // Diff btw 1st & 2nd part of sample
data
static unsigned int results[2 * Num_of_Results];
                          // data: 1st half-'High' & 2nd half-
'Low'

void Sys_Setup(void);         // Function protos.
void Sample (void);

void Sample_H(void);
void Sample_L(void);

void FirstRound (void);
void SecondRound(void);
void ThirdRound (void);

void UpdateBias(void);
void Sys_Delay();
```

```
unsigned long Avg_1st_Half(void);
unsigned long Avg_2nd_Half(void);

//////////////////////////////////////////////////////////////
//////
void Sys_Delay(int DelayCounts)
{
  int i;
  for(i=1; i<=DelayCounts; i++);
}
//////////////////////////////////////////////////////////////
//////
unsigned long Avg_1st_Half(void) // sum of 1st half
{
  unsigned int i;
  unsigned long Avg = 0;
  for (i = 0; i< Num_of_Results; i++)
    Avg += results[i];
  return (Avg);
}

//////////////////////////////////////////////////////////////
//////
unsigned long Avg_2nd_Half(void) // sum of 2nd half
{
  unsigned int i;
  unsigned long Avg = 0;
  for (i = Num_of_Results; i< 2 * Num_of_Results; i++)
    Avg += results[i];
  return (Avg);
}

//////////////////////////////////////////////////////////////
//////
void main(void)
{
  WDTCTL = WDTPW + WDTHOLD;       // Stop watchdog timer
  Sys_Setup();

  tP1IES = P1IES;                 // store the status of P1IES
  while (1)
  {
    SCount = 0;

    P1IE = BIT7;
    P1IFG = 0;
    _EINT();
    LPM0;                         // wait for one LD to be
turned on

    if (P1IES == 0x00)            // LD = 785 nm
    {
      if (V785 != 0) rVout = V785;
      else           rVout = 1365;
                // ini bias = 1365 x 3(ref) x 3 (amp) / 4096 =
1 Vact
    }

    if (P1IES == 0x80)             // LD = 808 nm
    {
      if (V808 != 0) rVout = V808;
```

```
      else           rVout = 1365;
                      // ini bias = 1365 x 3(ref) x 3 (amp) /
4096 = 1 Vact
    }

    FirstRound();

    if ((rDiff > Ath) | (rDiff < -Ath))  //adj. step for 2nd
round
      Vstep = BigStep;
    else
    {
      if (((rDiff >0) & (rDiff <= OPT)) | ((rDiff <0) &
(rDiff >= OPT)))
        Vstep = 2;
      else
        Vstep = SmallStep;
    }
    SecondRound();

    while (SCount <= (128*8))
                          // continuous sample for specified
samples
      ThirdRound();

    P1IES = tP1IES;       // restore P1IES
    if (tP1IES == 0x00)
        V785 = Vout;      // update & store bias for LD = 785
    if (tP1IES == 0x80)
        V808 = Vout;      // update & store bias for LD = 808

    P1IES ^= BIT7;     // toggle BIT7 for next wavelength
    tP1IES = P1IES;    // store the toggled P1IES
  }
}

////////////////////////////////////////////////////////////
//////
void Sys_Setup(void)
{
  // 1. Ports
  P1DIR  = 0x23;           // All P1 as outputs except P1.2,
1.3, 1.4
                           // Do not change 1.4 as output !
  P1OUT  = BIT0;           // lit up indicator LED

  P1IE  = 0x80;                // Disable switch interrupt
  P1IES = 0;                   // L to H transition for
interrupt
  P1IFG = 0;                   // Clear any pending IFGs

  P2DIR = 0xff;                // Output direction, except P2.3
  P2OUT = 0;                   // All P2 low
  P5DIR = 0xff;                // Output direction, except P2.3
  P5OUT = 0;                   // All P5 low

  P6DIR  = 0xfc;               // all P6 as Output except P6.0
& P6.1

  // 2. Registers
```

```
  DAC12_0CTL = DAC12OPS + DAC12SREF_1 + DAC12IR + DAC12AMP_7 +
DAC12ENC;
                  // DAC output external, Ref Voltage = AVcc,
                  // O/p Voltage range = 1x ref, Enable
conversion 1
                  // 1 LSB = 3/4096 = 0.732 mV

  SD16CTL = SD16REFON + SD16SSEL0;  // 1.2V ref, SMCLK
  SD16CCTL0  |= SD16SNGL + SD16IE;  // single conv., Enable
interrupt
  SD16INCTL0 |= SD16INTDLY_0;       // Interrupt on 4TH sample
  Sys_Delay(0x3600);
}

////////////////////////////////////////////////////////////////
//////
void Sample (void) // Begin ADC sampling -> save to global var
'results[]'
{
  _EINT();
  SD16CCTL0 |= SD16SC;          // Set bit to start conversion
  _BIS_SR(LPM0_bits);           // Enter LPM0

  P6OUT ^= BIT2;    // double-check the data acquisition
timepoint
  SCount ++;
}

////////////////////////////////////////////////////////////////
//////
void Sample_H (void)
{
  P1IFG = 0;
  P1IE  = BIT3;                     // enable interrupt
  P1IES = 0;                        // L-> H trigger
  _BIS_SR(LPM0_bits + GIE);         // waiting for trigger
(rise edge)

  P1IE &= ~BIT3;                    // disable trigger
interrupt
  P1IFG = 0;
  Sys_Delay(100);
  Sample();
  Sys_Delay(1050);
}

////////////////////////////////////////////////////////////////
//////
void Sample_L (void)
{
  P1IFG = 0;
  P1IE  = BIT3;                     // enable interrupt
  P1IES = BIT3;                     // H -> L trigger
  _BIS_SR(LPM0_bits + GIE);         // waiting for trigger
(fall edge)

  P1IE &= ~BIT3;                    // disable trigger
interrupt
  P1IFG = 0;
  Sys_Delay(100);
  Sample();
```

```
  Sys_Delay(1050);
}

////////////////////////////////////////////////////////////////
//////
void FirstRound(void)      // serve as reference
{
  DAC12_0DAT = rVout;      // output Bias to MZM

  for (sIndex = 0; sIndex < Num_of_Results; sIndex++)
    Sample_H();
  for (sIndex = Num_of_Results; sIndex < 2*Num_of_Results;
sIndex++)
    Sample_L();

  rfAvg = Avg_1st_Half();         // analyze modulation depth
  rsAvg = Avg_2nd_Half();
  rDiff = rfAvg - rsAvg;
}

////////////////////////////////////////////////////////////////
//////
void SecondRound (void)
{
  Vout = rVout - Vstep;     // backward 1 step
  DAC12_0DAT = Vout;        // update Bias

  for (sIndex = 0; sIndex < Num_of_Results; sIndex++)
    Sample_H();
  for (sIndex = Num_of_Results; sIndex < 2*Num_of_Results;
sIndex++)
    Sample_L();

  fAvg = Avg_1st_Half();         // analyze modulation depth
  sAvg = Avg_2nd_Half();
  Diff = fAvg - sAvg;
}

////////////////////////////////////////////////////////////////
//////
void UpdateBias(void)        // 'PID' ctrl based on Hysteresis
ctrl
{
  // difference in acceptable range
  if (((Diff <= Ath) & (Diff >=0)) | ((Diff >= -Ath) & (Diff
<0)))
  {
    // keep curr. direction & reduce step-size to fine correct
bias
    Vstep = SmallStep;

    // difference is very small
    if (((Diff <= OPT) & (Diff >=0)) | ((Diff >= OPT) & (Diff <
0)))
    {
      DIR = 0;        // maintain the current direction
      rVout = Vout;   // maintain current bias
      return;         // without any correction actions
    }
  }
```

```
  else   // difference is outside of acceptable range
  {
    Vstep = BigStep;  // restore large step to approach bias
quickly
    if (Diff > Ath)
    {
      DIR = 1;
      if (fAvg <= rfAvg)
      {
        if (rVout < Vout)
        {
          rVout = Vout;
          rDiff = Diff;
          rfAvg = fAvg;
          rsAvg = sAvg;
        }
      }
      else
      {
        if (rVout < Vout)
        {
          rVout = Vout;
          rDiff = Diff;
          rfAvg = fAvg;
          rsAvg = sAvg;
        }
      }
    }

    else
    {
      DIR = -1;
      if (fAvg <= rfAvg)
      {
        if (Vout < rVout)
        {
          rVout = Vout;
          rDiff = Diff;
          rfAvg = fAvg;
          rsAvg = sAvg;
        }
      }
      else
      {
        if (Vout < rVout)
        {
          rVout = Vout;
          rDiff = Diff;
          rfAvg = fAvg;
          rsAvg = sAvg;
        }
      }
    }
  }

  Vout = rVout + DIR * Vstep;  // shift bias according to the
'DIR'
  if (Vout > 3120)     // hop back if bias > 4 Vpi (773 x 4 =
3092)
    Vout -= 2 * Vpi;
  if (Vout < 800)      // hop up if bias is < 1 Vpi (773)
```

```
    Vout += 2 * Vpi;
}

//////////////////////////////////////////////////////////////
//////
void ThirdRound (void)
{
  UpdateBias();                // update rVout & Vout
  DAC12_0DAT = Vout;

  for (sIndex = 0; sIndex < Num_of_Results; sIndex++)
    Sample_H();
  for (sIndex = Num_of_Results; sIndex < 2*Num_of_Results;
sIndex++)
    Sample_L();

  fAvg = Avg_1st_Half();       // analyze modulation depth
  sAvg = Avg_2nd_Half();
  Diff = fAvg - sAvg;
}

// interrupt service routines
//////////////////////////////////////////////////////////////
//////
#pragma vector=PORT1_VECTOR //P1.3 ISR to 2.5 KHz square wave
(trig.)
__interrupt void P1_ISR (void)
{
  if ((P1IFG & BIT3) == BIT3)   // only P1.3 & mask other
interrupts
  {
    P1IFG = 0;
    LPM0_EXIT;
  }

  if ((P1IFG & 0x80) == 0x80)   // P1.7 interrupt for sampling
  {
    P1IFG = 0;
    LPM0_EXIT;
  }
}

#pragma vector=SD16_VECTOR
__interrupt void SD16ISR(void)
{
  switch (SD16IV)
  {
  case 2:                          // SD16MEM Overflow
    break;
  case 4:                          // SD16MEM0 IFG
    results[sIndex] = SD16MEM0;    // Save CH0 (clear IFG auto.)
    break;
  }
  LPM0_EXIT;
}
```

A.2 Optical detector

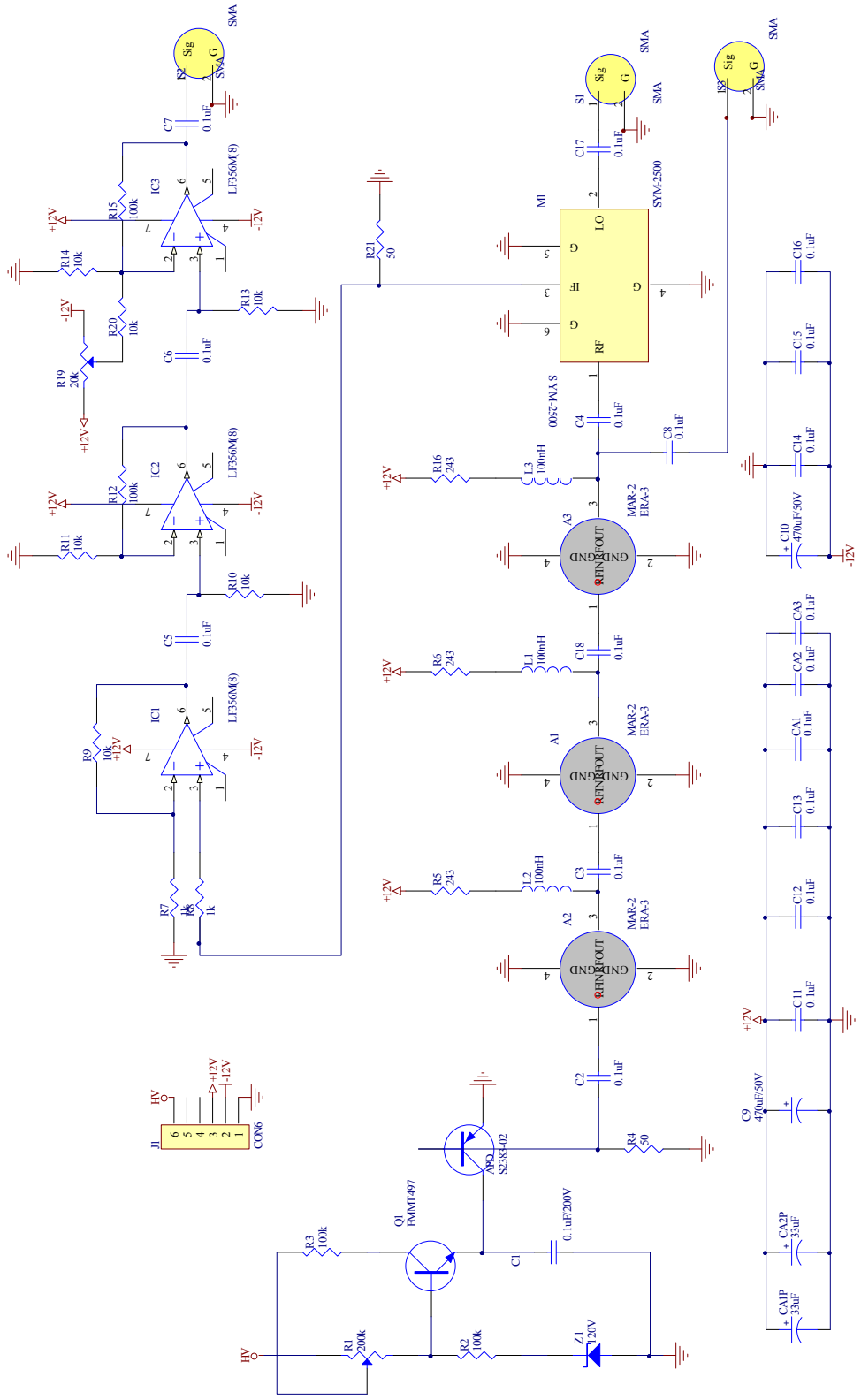

Fig. A- 3 Circuit schematic of PRBS correlation.

A.3 PRBS transceiver

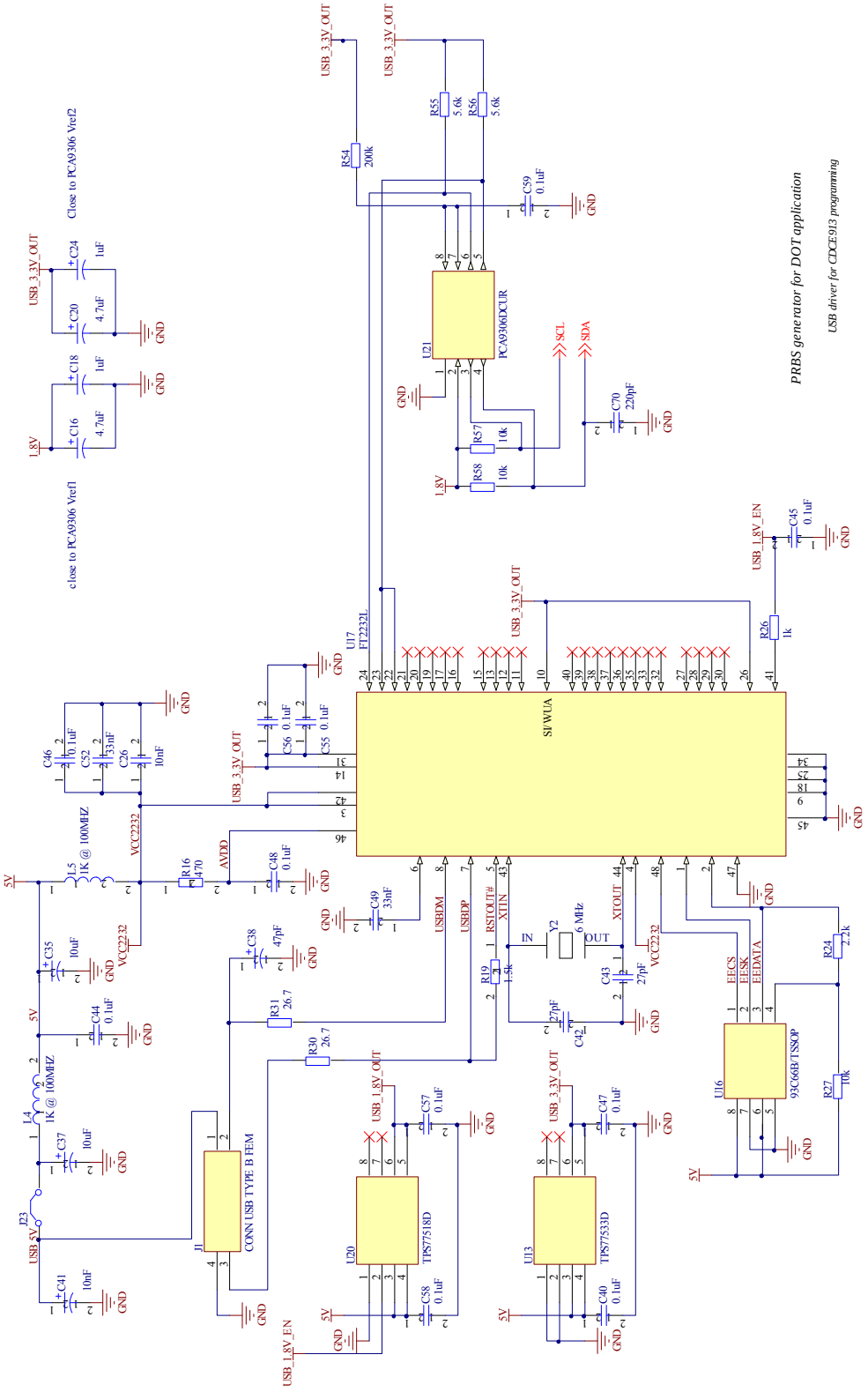

Fig. A- 4 Circuit schematic of PRBS (2.488 Gb/s, pattern length 127 bit) (1/3).

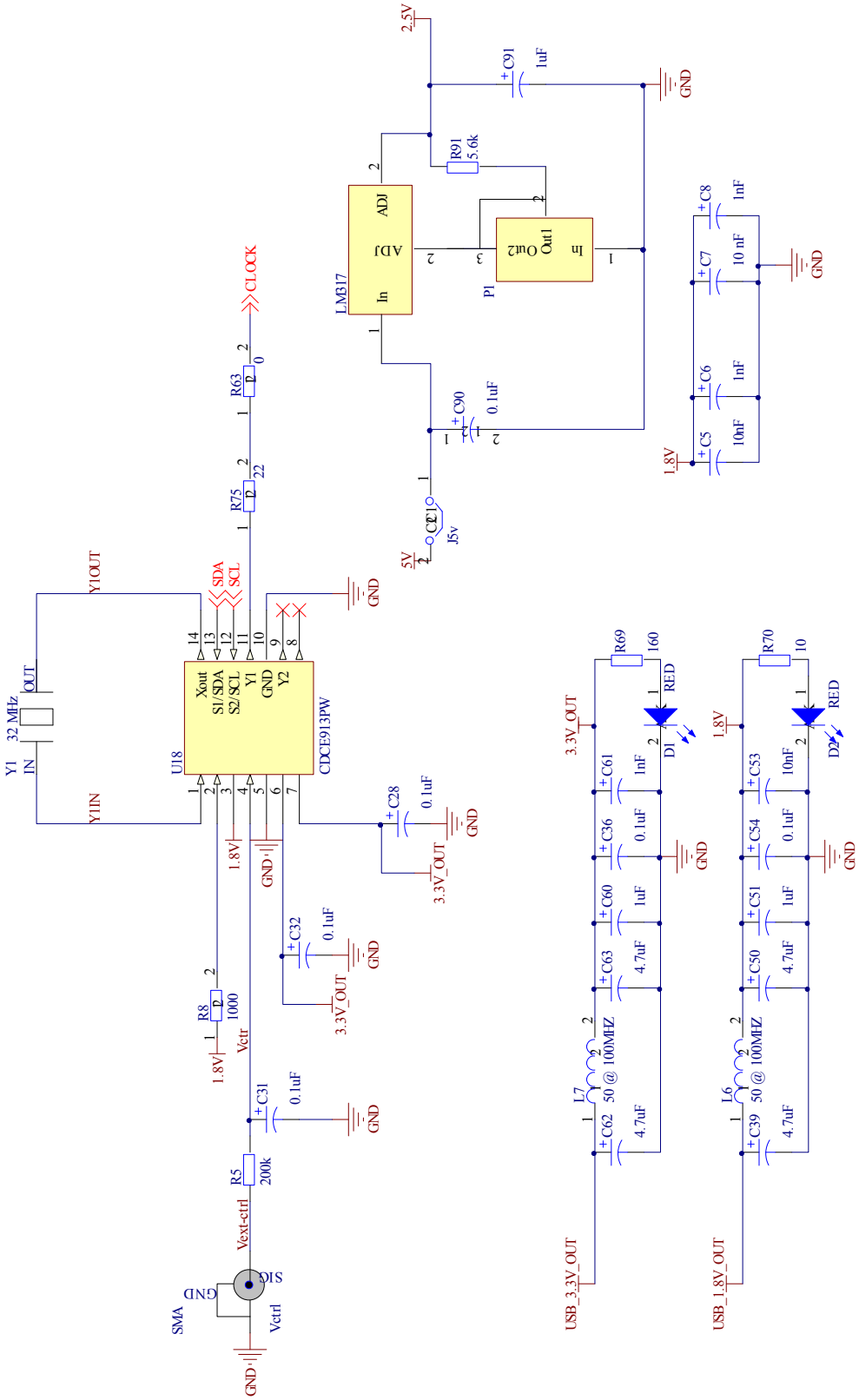

Fig. A- 5 Circuit schematic of PRBS (2.488 Gb/s, pattern length 127 bit) (2/3).

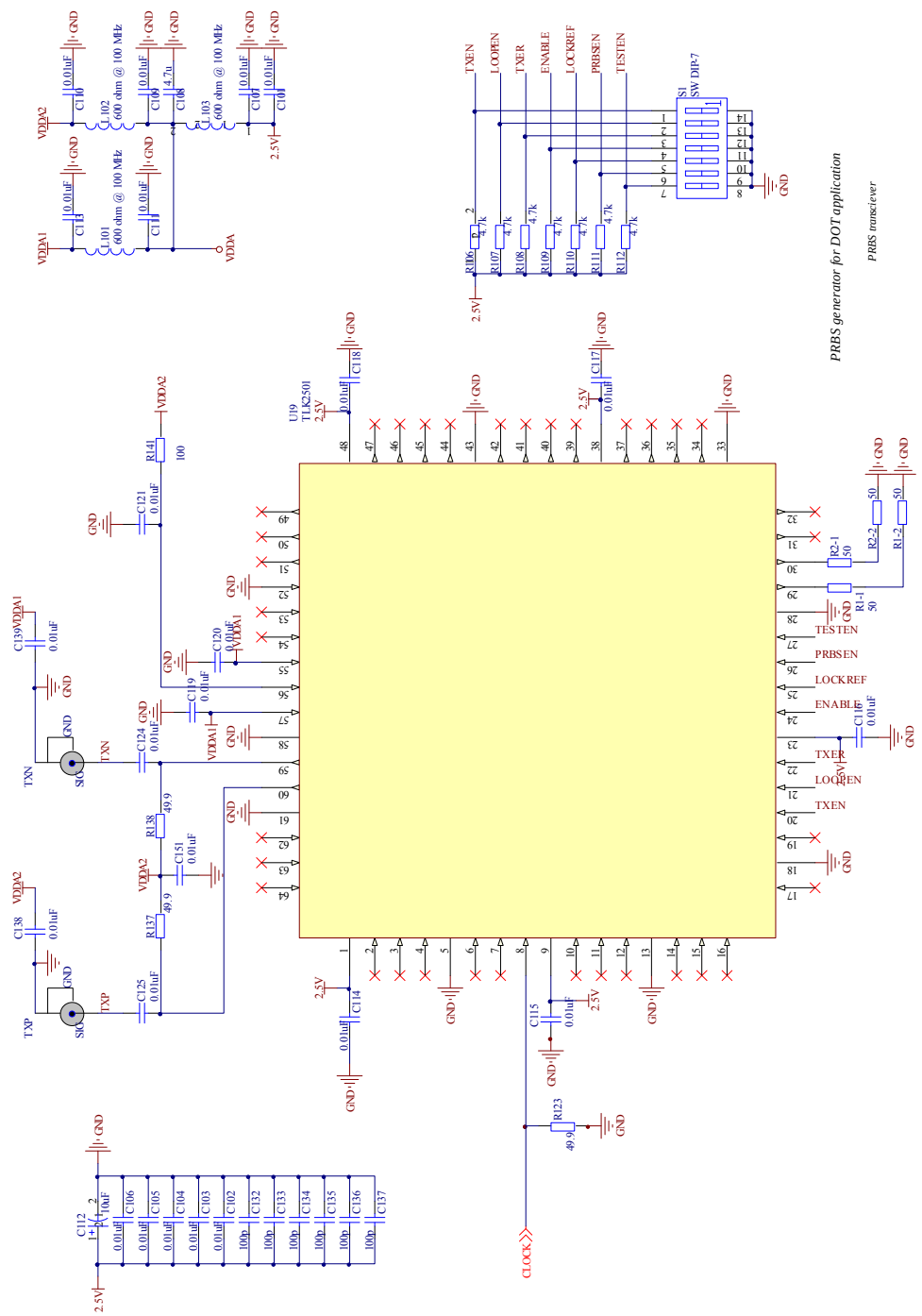

Fig. A- 6 Circuit schematic of PRBS (2.488 Gb/s, pattern length 127 bit) (3/3).

A.4 Phantom fabrication

A.4.1 Calculating the μ_s' of liquid phantom (Lipofundin solution)

The Lipofundin emulsion was purchased from product (Lipofundin MCT/LCT 20%, B.Braun Melsungen AG, Germany). Every 1000 ml Lipofundin emulsion contains

* Oil: Soya oil 100.0 g
* Phospholipids: Egg Lecithin 12.0 g
* Isotonic substance: Glycerol 25.0 g
* Medium-chain Triglycerides: 100.0 g

The physical parameters are [186 187 188] :

* Particles size in 20% emulsion: ~ 265 um;
* Number of particles for 20% MCT: ~ 140×10^{15} /Liter.

To use Mie calculator [189], a real refractive index of 1.46 and an imaginary refractive index of 0 were selected for Lipofundin emulsion [190].

According to the calculation results (see Table A-1), the isotropic scattering factor g is about 0.35, which gives a reduced scattering coefficient approximately of $\mu_s' = (1-g) \times \mu_s = (1- 0.35) \times 10.3$ cm^{-1} = 6.5 cm^{-1}. The overall absorption coefficient of the Lipofundin solution is solely contributed by distilled water, which is approximately of 0.022 cm^{-1} at 785 nm at room temperature. These values were used for prototype system calibration.

Table A- 1 Calculation results using Mie scattering calculation

Parameters	Value	Unit
Sphere Diameter	0.265	microns
Refractive Index of Medium (20^{o}C)	1.3316	
Real Refractive Index of Sphere	1.46	
Imaginary Refractive Index of Sphere	0.000016	
Wavelength in Vacuum	0.785	microns
Concentration	0.84*	spheres/micron^3
Wavelength in Medium	0.58952	microns
Size Parameter	1.4122	
Average Cosine of Phase Function	0.3478	
Scattering Efficiency	0.02233	
Extinction Efficiency	0.022378	
Backscattering Efficiency	0.01038	
Scattering Cross Section	0.0012316	micron^2
Extinction Cross Section	0.0012342	micron^2
Backscattering Cross Section	0.0005725	micron^2
Scattering Coefficient	1.0346	mm^{-1}
Total Attenuation Coefficient	1.0368	mm^{-1}

*0.6% Lipofundin solution × (140×10^{15}/liter) = 0.84 sphere/um^3

A.4.2 Fabrication of solid phantom

A.4.2.1 Quantities of ingredients

In Hebden's recipe [136], 330g of resin and 99 g of hardener were used. 1.4 g of titanium dioxide and 0.5 ml of 2% ink were added. The ingredients used in this research were similar to this recipe.

The amount of TiO_2 was assumed to be 0.325% of the total amount of resin and hardener (accelerator component is included if used). The factor of 0.325% is given by:

Factor for TiO_2 usage = Weight of TiO_2 / Total weight of ingredients, less ink

$$= \frac{1.4}{330 + 99 + 1.4}$$
$$= 0.325\%$$

The 2% ink was first prepared using 98ml of distilled water and 2ml of Pelikan 4001 ink. This 2% ink solution is subsequently used for all experiments. The amount of ink used was also assumed to be relative to the fraction of volume of ink used over the total weight of the epoxy resin in the above recipe. For example,

Factor for ink used = volume of ink used / total weight of ingredients, less ink

$$= \frac{0.5}{330 + 99 + 1.4}$$
$$= 0.1162\%$$

In this study, the elementary recipe contains 10 g epoxy resin, 6 g hardener, 0.04 g TiO_2 and 0.02 ml 2% ink. The Petri dishes (molds) that are used require a total volume of about 40 g (25 g resin, 15 g hardener). Thus the new factors involved are:

- Amount of TiO_2 = 0.325% × (Total amount of epoxy resin used)

  = 0.325% × (25 + 15)

  = 0.13 g (rounded up to 1 d.p.)
- Factor for ink used remains as 0.1162% as the amount of ink remains unchanged.

Amount of 2% ink = 0.1162% × (Total amount of epoxy resin used)

= 0.1162% × (25 + 15)

= 0.047 ml

Therefore the quantities of ingredients for making the optical phantom (disc) are:

* 25 g resin (Epicote 1006 System, Wee Tee Tong Chemicals Pte Ltd, SG);
* 15 g hardener (Epicote 1006 System, Wee Tee Tong Chemicals Pte Ltd, SG);
* 0.13 g titanium dioxide;
* 47 µl 2% ink (Pelikan 4001 ink).

A.4.2.2 Fabrication procedure

1. Mix appropriate amounts of resin, ink well in glass beaker.
2. Add appropriate amount of TiO_2 in glass beaker and mix well.
3. Degas mixture in desiccators/ break vacuum and repeat 3-4 times.
4. Add 50% of hardener and mix well especially bottom.
5. Add remaining hardener; mix well.
6. Degas again in desiccators as before, taking note of the viscosity/texture (indication of curing).
7. Remove from desiccators before it gets hot/ starts to react.
8. Pour mixture slowly into container/mold.
9. Let cure in hood (room temp.) or oven (higher temp.), not under vacuum.
10. When hardened, machine to finished cylinder.

A.5 DOT/DOS GUI

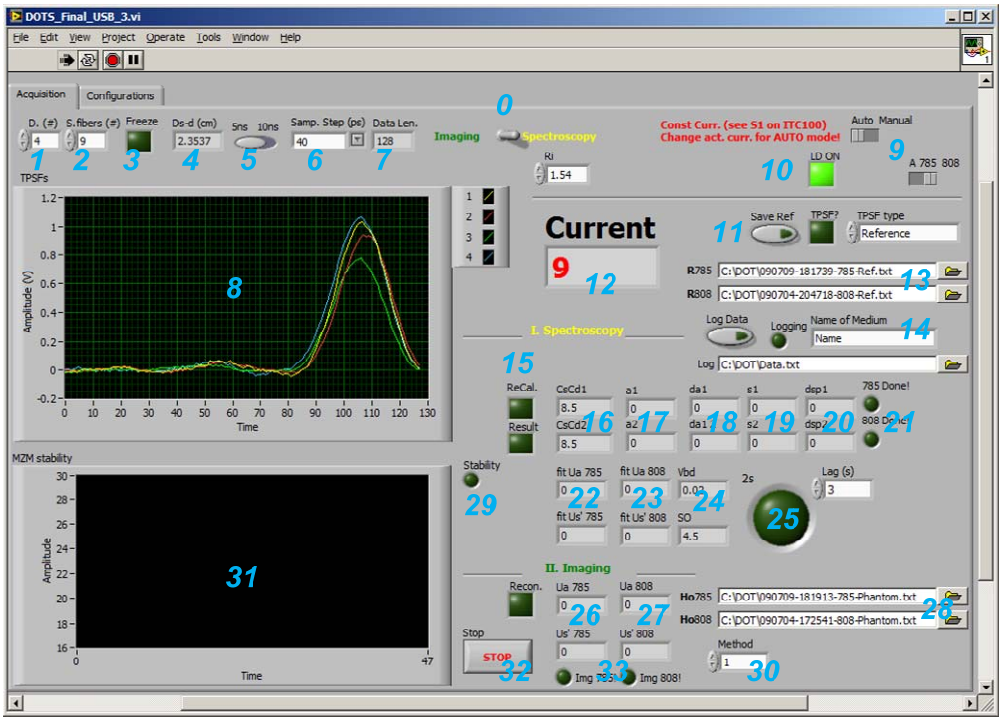

Fig. A- 7 Console of TPSF acquisition.

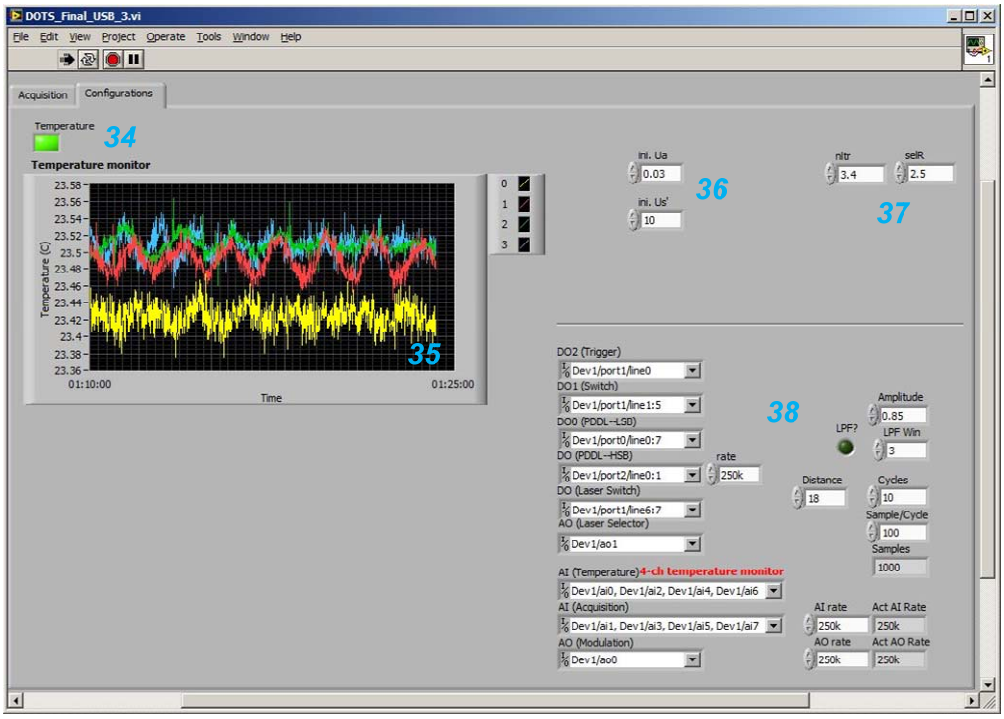

Fig. A- 8 Console of instrument configuration.

Table A- 2 Function descriptions (C: controller; I: Indicator)

#	Label	Type	Function description
0	Imaging/Spectroscopy	C	Function selection
1	Det.	C	Detectors number
2	Fibers	C	Source fibers number
3	Freeze	C	Freeze fiber sweeping.
4	Ds-d (cm)	I	Separation of optode.
5	5ns 10ns	C	TPSF length (5.12ns / 10.24 ns)
6	Samp. Step(ps)	C	Sampling interval (40ps / 80 ps)
7	Data Len.	I	TPSF data length (64 /128 / 256 / 512)
8	TPSF	I	TPSF display
9	Auto/Manual	C	Switch NIR LD “auto” or “manually”
10	LD ON	C	LD software switch
11	Save ref	C	Save current signal to data file
12	Current	I	Current light source fiber.
13	R785/R808	C	Data file for 785 nm & 808 nm
14	Name of Medium	C	Name of medium
15	Recal./Result	C	Show spectroscopic results
16	CsCd1, CsCd2	I	Calibration value of 785nm and 808 nm
17	a1, a2	I	μ_a of 785 nm and 808 nm
18	da1,da2	I	Fitting error of a1 & a2
19	s1,s2	I	μ_s’ at 785 nm and 808 nm
20	ds1, ds2	I	Fitting error of s1 & S2.
21	785/808 Done	I	Indicator for system calibration done
22	Fit Ua 785/Us’ 785	I	Fitted μ_a at 785 nm and fitted μ_s’ at 785 nm
23	Fit Ua 808/Us’ 808	I	Fitted μ_a at 808 nm and fitted μ_s’ at 808 nm
24	Vbd/SO	I	Physiological parameter: THC and SO
25	2s	C	Extra pause for operator to relocate probe
26	Ua 785 / Us’ 785	I	Fitted μ_a at 785 nm and fitted μ_s’ at 785 nm
27	Ua 808 / Us’ 808	I	Fitted μ_a at 808 nm and fitted μ_s’ at 808 nm
28	Ho785 / Ho808	C	Data file for homogeneous measurements
29	Stability	C	Show on/off stability monitoring
30	Method	C	Reconstruction method
31	MZM stability	I	Stability monitoring of the MZM

32	Stop	C	Stop and quit program
33	Img done	I	Indicator of image reconstruction finish
34	Temperature	C	Show on/off temperature
35	Tempearture	I	Temperature monitoring
36	Ini Ua Us’	C	Initial Ua Us’ guess
37	nLtr/separations	C	Separation of the optode for spectroscopy
38	“Configurations”	C	System hardware configurations

A.6 Matlab code for DOT

The main functions of TD-DOT are shown in Fig. A- 9 in a hierarchy view. The codes are listed below.

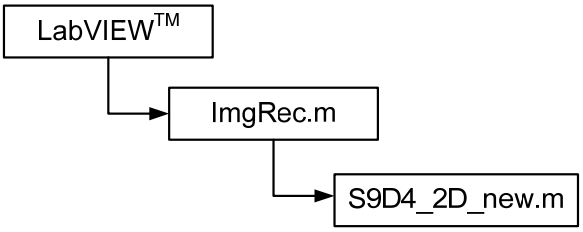

Fig. A- 9 Code hierarchy of TD-DOT functions.

A.6.1 Function "ImagRec.m"

```
%% DOT image reconstruction for single wavelength (785 nm)
function [fitMua fitMusp im_mua] = ImgRec(RefFile, HomoFile,
TPSF, mua0, musp0, Ri, nltr)
% input argument:
%   RefFile  - input data file of reference
%   HomoFile - input data file of homogeneous medium
%   TPSF     - acquired TPSF data
%   mua0     - ini. absorption coef. of background (0.02)
%   musp0    - ini. reduced scattering coef. of background (4.5)
%   Ri       - refractive index (H2O=1.33; epoxy resin= 1.56)
%   nltr     - numbers of ltr for the extropolated boundary
%
% output arguments:
%    fitMua   - fitted mua of the background;
%    fitMusp  - fitted mus'of the background;
%               & the reconstructed image data

%% define source and detector
source = 9;
detect = 4;

temp1 =  fliplr(importdata(RefFile));
temp2 =  fliplr(importdata(HomoFile));

s9d4_2D_new;  % define geometry of hand-held probe

ns = size(s_geom,1);
nd = size(d_geom,1);

%% Fig out CsCd
cscd = zeros(1,36);
bgMusp = zeros(1,36);
bgMua = zeros(1,36);

ref = zeros(1,128);
sig = zeros(1,128);
dmua = 1000; dmusp = 1000;
% count = 0;
while (dmua>=0.0005) | (dmusp > 0.001)
```

```
%     count = count +1
    for ss = 1:9
        for dd = 1: 4
            sd_num = (ss-1)*detect + dd;  %% index the S-D pair;
            ref(1, :) = temp1(sd_num,:);
            sig(1, :) = temp2(sd_num,:);
            % clear temp1 temp2;

            s_end = 0.3;
            s_laplace = [0.05 : 0.05 : s_end] * 1e9;
            s_num = length(s_laplace);

            Dstep = Dstep * 1e-12;
            t_insec = 0 : Dstep : (127*Dstep);
            Dstep = 40;

            dt = t_insec(2) - t_insec(1);

            c_light = 3e10 / Ri;
            c = c_light;

            D0 = 1 / 3 / musp0;
            r = sddist;

            clear klp0 k_laplace;
            for kk = 1 : s_num
                k_laplace(kk,:) = exp(-s_laplace(kk) * t_insec);
                klp0(kk)= sqrt((mua0+s_laplace(kk)/c_light)/D0);
            end

            lpd = zeros(s_num,3);
            lpd(:,1) = -1;
            clear lpm;

            for kk = 1 : s_num
                phi_lp(kk)=sum(sig(1,:).*k_laplace(kk,:))*Dstep;
                ref_lp(kk)=sum(ref(1,:).*k_laplace(kk,:))*Dstep;
                temp = klp0(kk) * r(sd_num);
                lpd(kk, 2)=temp*(-1+1/(1+temp))/D0/2 +1/D0;
                lpd(kk, 3) = temp * (1-1/(1+temp)) /
(mua0+s_laplace(kk) / c_light) / 2;
                lpm(kk) = log(1+temp) - temp - log(phi_lp(kk))
+ log(ref_lp(kk)) + log((10.2^2)*D0) - 3*log(r(sd_num));
            end
            lpp = lpd \ lpm';

            bgMusp(sd_num) = 1 / 3 / (D0+lpp(2));
            bgMua(sd_num) = mua0 + lpp(3);
            cscd(sd_num) = exp(lpp(1));
        end;
    end;

    % Mua0 = mean(bgMua);
    % Musp0 = mean(bgMusp);
    mua1  = mean(bgMua (find( (sddist>=2.5) & (sddist<3.5) )))
    musp1 = mean(bgMusp(find( (sddist>=2.5) & (sddist<3.5) )))

    dmua = abs( (mua1 - mua0)/mua0 );
    dmusp = abs( (musp1 -musp0)/musp0 );
```

```
mua0 = mua1
musp0 = musp1
end  % while loop

clear ref sig;

ref = zeros(36,1000);
sig = zeros(36,1000);

%% Figure out Mua, Mus' - based on Laplace transformation
ref(1: source*detect, :) = [temp1(:,:) zeros(source*detect,
1000-128)];
sig(1: source*detect, :) = [temp2(:,:) zeros(source*detect,
1000-128)];

temp3 = fliplr(TPSF);
sig1(1 : source*detect, :)    = [temp3  zeros(source*detect,
1000-128)];

s_end = 0.4;
s_laplace = [0.15 : 0.05 : s_end] * 1e9;
s_num = length(s_laplace);

t_insec = 0 : 40e-12 : (999*40e-12);
dt = t_insec(2)-t_insec(1);

c_light = 3e10 / Ri;
c = c_light;

D0 = 1 / 3 / musp0;
r = sddist;

clear klp0 k_laplace;
for kk = 1 : s_num
    k_laplace(kk,:)  =  exp(-s_laplace(kk) * t_insec);
    klp0(kk) = sqrt( (mua0+s_laplace(kk) / c_light) / D0);
end

lpd = zeros(s_num,3);
lpd(:,1) = -1;
clear lpm;

for sd_num = 1 : 36
    for kk = 1 : s_num
        phi_lp(kk) = sum(sig(sd_num,:) .* k_laplace(kk,:)) *
40e-12;
        ref_lp(kk) = sum(ref(sd_num,:) .* k_laplace(kk,:)) *
40e-12;
        temp = klp0(kk) * r(sd_num);
        lpd(kk, 2) = temp * (-1+1/(1+temp)) / D0 / 2 + 1/D0;
        lpd(kk, 3) = temp * (1-1/(1+temp)) / (mua0+s_laplace(kk)
/ c_light) / 2;
        lpm(kk) = log(1+temp) - temp - log(phi_lp(kk)) +
log(ref_lp(kk)) + log((10.2^2)*D0) + log(cscd(sd_num)) -
3*log(r(sd_num));
    end
    lpp = lpd \ lpm';
    musp(sd_num) = 1 / 3 / (D0+lpp(2));
```

```
    mua(sd_num) = mua0 + lpp(3);
end

mua0  = mean(mua (find( (sddist>=2.3) & (sddist<3.1) )))
musp0 = mean(musp(find( (sddist>=2.3) & (sddist<3.1) )))
ltr   = 1 / (mua0 + musp0);

fitMusp = musp0;
fitMua = mua0;

D0 = 1/(fitMua+fitMusp)/3;

%% calculate Jacobian Matrix
clear klp0 k_laplace;
for kk = 1:s_num
    k_laplace(kk,:) = exp(-s_laplace(kk)*t_insec);
    klp0(kk) = sqrt((mua0+s_laplace(kk)/c_light)/D0);
end;  % Laplace kernel

Jac2Da = [];
deltax = 0.5;
deltay = 1;
deltaz = 0.5;
dz = [0 0 nltr*D0*3];

pix1 = 0;
yi = 0;

for xi = -2.5:deltax:2.5
    for zi = 0.25:deltaz:2.5
        pix1 = pix1 + 1;
        rt = [xi, yi, zi];
        p1a = [];
        for jj = 1:ns
            rst = sqrt(sum((s_geom(jj,:)-rt).^2));
            rst1 = sqrt(sum((s_geom(jj,:)-rt-dz).^2));
            phil = (exp(-klp0*rst)-exp(-klp0*rst1))/4/pi/D0/rst;
            for kk = 1:nd
                rtd = sqrt(sum((d_geom(kk,:)-rt).^2));
                rtd1 = sqrt(sum((d_geom(kk,:)-rt-dz).^2));
                temp = -phil.*(exp(-klp0*rtd)-exp(-
klp0*rtd1))/4/pi/D0/rtd;
                rsd = sqrt(sum((s_geom(jj,:)-d_geom(kk,:)).^2));
                rsd1 = sqrt(sum((s_geom(jj,:)-d_geom(kk,:)-
dz).^2));
                phisd = (exp(-klp0*rsd)-exp(-
klp0*rsd1))/4/pi/D0/rsd;
                p1a = [p1a; (temp./phisd)'];
            end
        end
        Jac2Da = [Jac2Da p1a];
    end
end

%% reconstruction using pseudo-inverse tech.
aa = (eye(55)/(Jac2Da'*Jac2Da+0.2*eye(55)))*Jac2Da';

sigl = [];
sig1l = [];
```

```
refl = [];

for jj = 1:ns
    for kk = 1:nd
        ss = sig((jj-1)*4+kk,:);
        ss1 = sig1((jj-1)*4+kk,:);
        rr = ref((jj-1)*4+kk,:);
        rr = rr/sum(rr);
        for ll = 1:s_num
            sigl = [sigl; dt*sum(ss.*k_laplace(ll,:))];
            sig1l = [sig1l; dt*sum(ss1.*k_laplace(ll,:))];
            refl = [refl; dt*sum(rr.*k_laplace(ll,:))];
        end
    end
end

dm = (sig1l-sigl)./sigl;
dm = dm.*(sign(-dm)+1)/2;
dmua1 = aa*dm;

clear im_mua;
for kk = 1:11
    for jj = 1:5
        im_mua(jj,kk) = dmua1((kk-1)*5+jj);
    end
end

maxPt = 1.05 * max(max(im_mua));
figure(1);
imagesc(-2.5:0.5:2.5,0.25:0.5:2.5, im_mua);
hold on;  axis equal;  xlabel 'X (cm)'; ylabel 'Depth (cm)';
colorbar;
```

A.6.2 Function “S9D4_2D_new.m”

```
%% define the geometry of the hand-held probe
source = 9;
detect = 4;

% source geometry
s_geom = zeros(source,3);
s_geom = [  -1     0  0;
          -0.5     0  0;
             0     0  0;
           0.5     0  0;
             1     0  0;
            -1  -0.5  0;
             1  -0.5  0;
            -1   0.5  0;
             1   0.5  0];

%detector geometry
d_geom = zeros(detect,3);
d_geom = [ -2.5     0   0;
            2.5     0   0;
           -3.3     0   0;
            3.3     0   0];
```

```
Measmnt=[];
k1=0;
pairs = zeros(source,detect);
sddist_matrix = zeros(source,detect);

seldist = 10;
for ii=1:source;
    k=(ii-1)*detect;

    for jj=1:detect;
        k=k+1;
        k1=k1+1;
        sddist_matrix(ii,jj)=sqrt((s_geom(ii,1)-
d_geom(jj,1))^2+(s_geom(ii,2)-d_geom(jj,2))^2);

        if(sddist_matrix(ii,jj)<1 |
sddist_matrix(ii,jj)>seldist)
            k1=k1-1;
        else
            sddist(k1)=sddist_matrix(ii,jj);
            Measmnt(k1,2)=jj;
            Measmnt(k1,1)=ii;
            pairs(ii,jj)=1;
        end
    end
end
Nmeas=size(Measmnt,1);
```

A.7 Matlab code for DOS

Fig. A- 10 shows a hierarchy diagram of main functions for TD-DOS. The codes implementations are shown below.

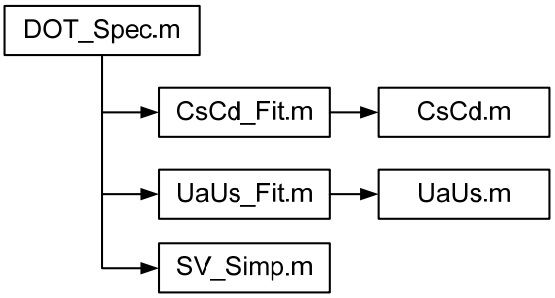

Fig. A- 10 Hierarchy diagrams of functions of TD-DOS.

A.7.1 Function "DOT_Spec.m"

```
%% in-vivo breast spectroscopy (main function)
% calc. DOT-style spectroscopy for 19 healthy subjects:
%     1. absorption coefficients Ua
%     2. reduced scattering coefficient Us'
%     3. oxygenation saturation
%     4. total hemoglobin concentration
% user need to specify data directory where breast scanning
data is
% 1st step: calibration system
% 2nd step: calculate the desired (above 4 types) data

clc;
Age = [50 48 50 23 41 45 23 49 50 47 49 26 26 48 44 43 51 50 49
23];  % ages of subjects
BMI = [27.5 21.5 20.3 21.6 25 20.1 19.1 24.9 30.6 20.6 19.9
20.3 24.1 23.5 21.2 20.4 24.7 21.4 24.9 18.8]; % BMIs of
subjects

Data = zeros(800, 11);
AvgData = zeros(160, 14);

dataS = zeros(5,1);
dataV = zeros(5,1);
dataA1 = zeros(5,1);
dataA2 = zeros(5,1);
dataS1 = zeros(5,1);
dataS2 = zeros(5,1);

% probe location on the breasts.
Loc = ['R1'; 'R2'; 'R3'; 'R4'; 'L1'; 'L2'; 'L3'; 'L4'];

% define background constituents: water and lipid in
concentration
Cpre  = 0.26;  % H2O concen. of PRE- (default: 0.26+-0.06)
Cpost = 0.11;  % H2O concen. of POST- (default: 0.11 +-0.01)
Cw = Cpre * ones(1,20);    % pre  -
Cw(1,[14,15,19]) = Cpost;  % post -
```

```
Cf = 0.57 * ones(1,20);   % lipid concentration (57%)

%% data file location
for iii = 1:20
    DataDir = [..\V' int2str(iii) '\'];

    Ref_785 = [DataDir 'r785.txt'];
    Ref_808 = [DataDir 'r808.txt'];

    Phan_785 = [DataDir 'p785.txt'];
    Phan_808 = [DataDir 'p808.txt'];
    CsCd_Fit;

    for jjj = 1:8
        for mmm = 1:5
            TPSF_785 = [DataDir '785-v' int2str(iii) '-'
Loc(jjj,:) '-' int2str(mmm) '.txt'];
            TPSF_808 = [DataDir '808-v' int2str(iii) '-'
Loc(jjj,:) '-' int2str(mmm) '.txt'];
            UaUs_Fit;
            Row =(iii-1)*40+(jjj-1)*5+mmm;
            Data(Row, 1:11) = [iii jjj mmm real(CsCd1)
real(CsCd2) real(fMua1) real(fMusp1) real(fMua2) real(fMusp2)
real(S) real(V)];
            disp(Data(Row,:));
        end;

        dataA1 = Data(Row-4:Row, 6);
        avgA1 = GetAvg(dataA1);

        dataS1 = Data(Row-4:Row, 7);
        avgS1 = GetAvg(dataS1);

        dataA2 = Data(Row-4:Row, 8);
        avgA2 = GetAvg(dataA2);

        dataS2 = Data(Row-4:Row, 9);
        avgS2 = GetAvg(dataS2);

        dataS  = Data(Row-4:Row, 10);
        avgS = GetAvg(dataS);            %% special filter

        dataV  = Data(Row-4:Row, 11);
        avgV = GetAvg(dataV);

        [avgSS avgVV ] = SV_Simp2(avgA1,avgA2, Cw(iii),
Cf(iii));

        AvgData((iii-1)*8+jjj, 1:14) = [iii jjj real(CsCd1)
real(CsCd2) avgA1 avgS1 avgA2 avgS2 avgS avgSS avgV avgVV
Age(iii) BMI(iii)];
    end;

end;
```

A.7.2 Function “CsCd_Fit.m”

```
%% fitting CsCd at 785 nm & 808 nm.
da1 = 1000; da2 = 1000; dsp1 = 1000; dsp2 = 1000; % huge values
a1 = 0.02; sp1 = 7; a2 = 0.02; sp2 = 7;

%% data for processing
Lambda = 1 ;
WindLen = 5120; SN  = 6; DN  = 3; Dstep = 40; minStep = 40; Ri
= 1.54;

%% 785 nm
a0 = 0.03; sp0 = 6;
   [CsCd1 a1 sp1]  =  CsCd(WindLen, SN, DN, Dstep, minStep,
Ref_785, Phan_785, a0, sp0, Ri); % calibrate coupling
coefficients
   da1   = abs(a1 - a0) / a0;
   dsp1  = abs(sp1 - sp0) / sp0;

   while ( (da1 >= 0.00002) || (dsp1  >=0.000005) )   % refine
       a0  = a1;
       sp0 = sp1;
       [CsCd1 a1 sp1]  =  CsCd(WindLen, SN, DN, Dstep, minStep,
Ref_785, Phan_785, a0, sp0, Ri); % fitting coupling
coefficients
       da1  = abs(a1 - a0) / a0;
       dsp1 = abs(sp1 - sp0) / sp0;
   end;

%% 808 nm
a0 = 0.03; sp0 = 6;
  [CsCd2 a2 sp2]  =  CsCd(WindLen, SN, DN, Dstep, minStep,
Ref_808, Phan_808, a0, sp0, Ri); % calibrate coupling
coefficients
  da2   = abs(a2 - a0) / a0;
  dsp2  = abs(sp2 - sp0) / sp0;

   while ( (da2 >= 0.00002) || (dsp2 >= 0.000005) )  % refine
       a0  = a2;
       sp0 = sp2;
       [CsCd2 a2 sp2]  =  CsCd(WindLen, SN, DN, Dstep, minStep,
Ref_808, Phan_808, a0, sp0, Ri); % fitting coupling
coefficients
       da2  = abs(a2 - a0) / a0;
       dsp2 = abs(sp2 - sp0) / sp0;
   end;
```

A.7.3 function “UsUa_Fit.m”

```
%% fitting Ua & Us at 785 & 808 nm
Ri =1.4;

%%%%%%%%%%%%%%%%%%%%%%%%%%%%%%%%%%%%%%%%%%%%%%%%%%%%%%%%%%%%%%%%%%%%%%%%%%%%
mua0 = 0.05; musp0 = 10;
for kk1 = 1:200
    [fMua1, fMusp1]  =  UaUs(WindLen, SN, DN, Dstep, minStep,
Ref_785, TPSF_785, mua0, musp0, Ri, CsCd1);
```

```
    Err1 = abs((fMua1 - mua0) / mua0);
    Err2 = abs((fMusp1 - musp0) / musp0);
    if ( (Err1 <= 0.0005) && (Err2 <= 0.00005) )   % close
enough,
        break;
    else
        mua0 = fMua1; musp0 = fMusp1;
    end;
end;

%%%%%%%%%%%%%%%%%%%%%%%%%%%%%%%%%%%%%%%%%%%%%%%%%%%%%%%%%%%%%%%%%%%%%%%%%%%%
mua0 = 0.05; musp0 = 10;
for kk2 = 1:200
    [fMua2, fMusp2]  =  UaUs(WindLen, SN, DN, Dstep, minStep,
Ref_808, TPSF_808, mua0, musp0, Ri, CsCd2);

    Err1 = abs((fMua2 - mua0) / mua0);
    Err2 = abs((fMusp2 - musp0) / musp0);
    if ( (Err1 <= 0.0005) && (Err2 <= 0.00005) ) % close enough
        break;
    else
        mua0 = fMua2; musp0 = fMusp2;
    end;
end;

%% calculate the SO and Vblood
c1 = fMua1;
c2 = fMua2;
[S V] = SV_Simp (c1, c2, Cw(iii), Cf(iii));
```

A.7.4 Function “CsCd.m”

```
%% Spectrometer for HbO2 and Saturation

function [cscd bgMua bgMusp] = CsCd(WindLen, SN, DN, Dstep,
minStep, RefFile, TPSF, mua0, musp0, Ri)
% input arguments:
%    WindLen  - window length for TPSF extension (5120* or
10240 ps);
%    SN, DN   - index of source fiber and detection channel
%    Dstep    - Delay step of the PDDL (40* or 80 ps)
%    minStep  - min delay step of the PDDL (40* or 80 ps)
%    Dstep    - Delay step of the PDDL
%    ref      - Reference data. 9 sources 4 detectors
%    TPSF     - acquired TPSF data. One source 4 detectors.
%    mua0     - initial guess of absorption coef.
%    musp0    - initial guess of reduced scattering coef.
%    Ri       - refractive index of medium (H2O=1.33;epoxy
resin=1.56)
%
% output arguments:
%    bgMua   - fitted mua0;
%    bgMusp  - fitted mus';

%% initialize and load data
s9d4_2D_new;  % define probe geometry
ns = size(s_geom,1);
```

```
nd = size(d_geom,1);

temp1 = fliplr(importdata(RefFile));
temp3 = fliplr(importdata(TPSF));

sd_num = (SN-1)*detect + DN;   %% index S-D pair;

% use 1st value of each TPSF for the large delay intervals;
ref(1, :) = temp1(sd_num,1:(Dstep/minStep):end);
sig(1, :) = temp3(sd_num,:);
clear temp1 temp3;

%% forward solution - based on Laplace transform
s_end = 0.62;
s_laplace = [0.42 : 0.05 : s_end] * 1e9;
s_num = length(s_laplace);

Dstep = Dstep * 1e-12;

t_insec = 0 : Dstep : ((WindLen*1e-12/Dstep -1)*Dstep);

dt = t_insec(2) - t_insec(1);

c_light = 3e10 / Ri;
c = c_light;

D0 = 1 / 3 / musp0;
r = sddist;

clear klp0 k_laplace;
for kk = 1 : s_num
    k_laplace(kk,:)  =  exp(-s_laplace(kk) * t_insec);
    klp0(kk) = sqrt( (mua0+s_laplace(kk) / c_light) / D0);
end

lpd = zeros(s_num,3);
lpd(:,1) = -1;
clear lpm;

for kk = 1 : s_num
    phi_lp(kk) = sum(sig(1,:) .* k_laplace(kk,:)) * Dstep;
    ref_lp(kk) = sum(ref(1,:) .* k_laplace(kk,:)) * Dstep;
    temp = klp0(kk) * r(sd_num);
    lpd(kk, 2) = temp * (-1+1/(1+temp)) / D0 / 2;
    lpd(kk, 3) = temp * (1-1/(1+temp)) / (mua0+s_laplace(kk) /
c_light) / 2;
    lpm(kk) = log(1+temp) - temp + log((10.2^2)*D0/8/pi) -
3*log(r(sd_num)) + log(ref_lp(kk)) - log(phi_lp(kk));
end
lpp = lpd \ lpm';

bgMusp = 1 / 3 / (D0+lpp(2));
bgMua = mua0 + lpp(3);
cscd = exp(lpp(1));
```

A.7.5 Function "UaUs.m"

```
%% Spectrometer for HbO2 and Saturation
% cal. background mua and musp ahead
% regarding inhomogeneous TPSF as evenly distributed
homogeneous TPSF
% non-zero padding

function [bgMua bgMusp] = UaUs(WindLen, SN, DN, Dstep, minStep,
RefFile, TPSF, mua0, musp0, Ri, cscd )
% input arguments:
%    WindLen  - window length for TPSF extension (5120* or
10240 ps);
%    SN, DN   - index of source fiber and detection channel
%    Dstep    - Delay step of the PDDL (40* or 80 ps)
%    minStep  - min delay step of the PDDL (40* or 80 ps)
%    ref  -  Reference data. 9 sources 4 detectors
%    TPSF     - acquired TPSF data. One source 4 detectors.
%    mua0     - initial guess of absorption coef.
%    musp0    - initial guess of reduced scattering coef.
%    Ri       - refractive index of medium (H2O=1.33;epoxy
resin=1.56)
% output arguments:
%    bgMua   - fitted mua0;
%    bgMusp  - fitted mus';

%% load and initialize data
s9d4_2D_new;  % define probe geometry
ns = size(s_geom,1);
nd = size(d_geom,1);

temp1 = fliplr(importdata(RefFile));
temp3 = fliplr(importdata(TPSF));

sd_num = (SN-1)*detect + DN;   %% index S-D pair;

ref(1, :) = temp1(sd_num,1:(Dstep/minStep):end);
sig(1, :) = temp3(sd_num,:);
clear temp1 temp3;

%% forward solution - based on Laplace
s_end = 0.62;
s_laplace = [0.42 : 0.05 : s_end] * 1e9;
s_num = length(s_laplace);

Dstep = Dstep * 1e-12;

t_insec = 0 : Dstep : ((WindLen*1e-12/Dstep -1)*Dstep);

dt = t_insec(2) - t_insec(1);

c_light = 2.997e10 / Ri;
c = c_light;

D0 = 1 / 3 / musp0;
r = sddist;

clear klp0 k_laplace;
```

```
for kk = 1 : s_num
    k_laplace(kk,:)  =  exp(-s_laplace(kk) * t_insec);
    klp0(kk) = sqrt( (mua0+s_laplace(kk) / c_light) / D0);
end

lpd = zeros(s_num,2);

clear lpm;

for kk = 1 : s_num
    phi_lp(kk) = sum(sig(1,:) .* k_laplace(kk,:)) * Dstep;
    ref_lp(kk) = sum(ref(1,:) .* k_laplace(kk,:)) * Dstep;
    temp = klp0(kk) * r(sd_num);
    lpd(kk, 1) = temp * (-1+1/(1+temp)) / D0 / 2  ;%+ 1/D0;
    lpd(kk, 2) = temp * (1-1/(1+temp)) / (mua0+s_laplace(kk) /
c_light) / 2;
    lpm(kk) = log(1+temp) - temp + log((10.2^2)*D0/8/pi) -
3*log(r(sd_num))+ log(cscd) + log(ref_lp(kk)) - log(phi_lp(kk));
end
lpp = lpd \ lpm';

bgMusp = 1 / 3 / (D0+lpp(1));
bgMua = mua0 + lpp(2);
```

A.7.6 Function “SV_Simp.m”

```
%% calc. one Saturation & blood volume
function [S V] = SV_Simp2(c1, c2, Cw, Cf);
% input:
%       c1: reconstructed coefficient of Mua of 785 nm
%       c2: reconstructed coefficient of Mua of 808 nm
%       a : absorption coefficient of deoxy-hemoglobin at 785
nm
%       b : absorption coefficient of oxy-hemoglobin at 785 nm
%       c : absorption coefficient of deoxy-hemoglobin at 808
nm
%       d : absorption coefficient of oxy-hemoglobin at 808 nm
% output:
%       S : saturation of the oxygen;
%       V : blood volume of the tissue;

% extinction coff.: unit:  /cm/uM;
% a * [Hb] + b * [HbO] = Mua_785;
% c * [Hb] + d * [HbO] = Mua_808;

% 20% water (post-menupausal: 11+-1%; pre-menupausal: 26+-6%),
% 57% lipid;
cb785 = 0.0252*Cw + 0.00357*Cf;
cb808 = 0.0218*Cw + 0.00497*Cf;

% delta Ua 785 and delta Ua808
c1 = c1 - cb785;
c2 = c2 - cb808;

% a = 2.2962e-3;  b = 1.7682e-3; c = 1.8508e-3;  d = 2.1096e-
3;  %UCL
```

```
a = 2.2048e-3;  b = 1.6812e-3; c = 1.6663e-3;  d = 1.9714e-
3;  %OMLC

Hb  = (c1*d - c2*b)/(a*d - b*c);
HbO = (a*c2 - c*c1)/(a*d - b*c);

S = HbO/(HbO+Hb);
V = Hb + HbO;
```

A.8 Publication list from this research

1) Journal publications

[1] **Weirong Mo** and Nanguang Chen, "Fast time-domain diffuse optical tomography using pseudorandom bit sequence," *Optical Express,* **16** (18), 13643-13650, (2008). – selected to publish in *Virtual Journal of Biomedical Optics*.

[2] **Weirong Mo** and Nanguang Chen, "Design of advanced time-domain diffused optical tomography," *IEEE, Journal of Selected Topics in Quantum Electronics*, **99(1)**, 1-7, (2009).

[3] **Weirong Mo,** Tryphena S. S. Chan, Ling Chen and Nanguang Chen, "Quantitative characterization of optical and physiological parameters in normal breasts using time-resolved spectroscopy: *in-vivo* results of 19 Singapore women," *Journal of Biomedical Optics,* **14(6)**, 064004, (2009). – selected to publish in *Virtual Journal of Ultrafast Science.*

2) Conference publications

[1] **Weirong Mo** and Nanguang Chen, "Source stabilization for high quality of the time-domain diffuse optical tomography". *Proc. SPIE. Design and Quality for Biomedical Technologies II.* **7170**, 71700N (2009).

[2] **Weirong Mo** and Nanguang Chen, "High performance time-resolved diffuse optical tomography system". *Proc. SPIE. Design of Biomedical Imaging Technologies*. **6849**, 684904, (2008);

[3] **Weirong Mo** and Nanguang Chen, "A novel Implementation of time-domain diffusive optical tomography". *Proc. IEEE/ICME Complex Medical Engineering*, 1101-1104, (2007).